

Universität
Rostock



Traditio et Innovatio

Influence of the pore structure on the catalytic performance of Rh-supported Zr-MOFs in the hydroformylation of olefins

Dissertation

zur

Erlangung des akademischen Grades

doctor rerum naturalium (Dr. rer. nat.)

der Mathematisch-Naturwissenschaftlichen Fakultät

der Universität Rostock

vorgelegt von Yanjun Sun, geb. am 25.09.1990 in Tonghua, China

Rostock, 13.07.2020

Die vorliegende Arbeit wurde in der Zeit von Oktober 2016 bis Oktober 2020 am Institut für Chemie der Universität Rostock am Lehrstuhl für Anorganische Chemie in der Arbeitsgruppe von Prof. Dr. Axel Schulz angefertigt.

1. Gutachter: Prof. Dr. Axel Schulz

2. Gutachter:

ERKLÄRUNG

Ich versichere hiermit an Eides statt, dass ich die vorliegende Arbeit selbstständig angefertigt und ohne fremde Hilfe verfasst habe. Dazu habe ich keine außer den von mir angegebenen Hilfsmitteln und Quellen verwendet und die den benutzten Werken inhaltlich und wörtlich entnommenen Stellen habe ich als solche kenntlich gemacht.

Rostock, 13.07.2020

.....

Yanjun Sun

Acknowledgements

This thesis provided some important results in the hydroformylation with Rh-supported zirconia based MOFs. In the four years of research work and daily life, I got encouragement support and guidance from many people. Here I would like to take the great opportunity to express my gratitude and thanks to all.

First of all, my most sincere thanks to Prof. Dr. Axel Schulz. Thank him for giving me such a great opportunity to come to study abroad and become a member of this great research group. Thank him for providing me with a great opportunity to study abroad and become a member of this great research team. I also thank him for the convenience he provided in the process of signing documents, the financial support provided in participating in international conferences, and the patient modification of the final article and thesis writing process.

I would great thank Dr. habil. Hendrik Kosslick for his kind help in my studies and life. When I first came to Germany, I was unfamiliar with everything, thank him for his great help in renting and processing documents. Under his patient guidance, I expanded a lot on the basis knowledge of porous materials related characterization. I have also a deeper understanding of active transition metals and their applications in catalysis. Thank him for his in-depth explanation of many professional knowledge in the process of writing papers and articles and the patiently verbatim modification of language.

I am great grateful to PD Dr. sc. nat. Marcus Frank and Dr. rer. nat. Armin Springer from the Elektronenmikroskopisches Zentrum (EMZ) for their kind cooperation in our project of Catalysis of Rh-supported Zr-MOFs. Thank Dr. Jörg Harloff for providing me his dedicated instructions on the organic synthesis and kind assistance with the preparation of the ligands. I sincerely thank Dr. Stephan Bartling at the Leibniz Institute for Catalysis (LIKAT) for his enthusiastic explanation and kind advices in XPS analysis. Thanks for the people mentioned above and their enormous experience in characterization and catalysis. Besides, a number of the staffs at LIKAT helped me a lot during the four years' work to improve my knowledge and skills. I am sincerely grateful to Dr. Christine Fischer, Mrs. Susanne Schareina and Mrs. Suann Buchholz at LIKAT.

Special thanks to my friends and my group members for their help over the past few years. Dr. Ronald Wustrack, Dr. Jonas Bresien, Mrs. Kerstin Bohn, Mrs. Regina Brosin, Mrs. Nadja Kohlmann, Dr. Farooq Ibad, Dr. Riaz Muhammad, Dr. Sören Arlt, Dr. Mishal Ibrahim, other group members and my Chinese friends from other group at LIKAT. Thank you all for their encouragement and supports during my work in the lab.

Sincere deep thanks to my family – my grandma, my parents, my fiancé for their love, encouragement and supports, which motived me to overcome all the difficulties and challenges during the work and life abroad. I am deeply indebted to Chinese Scholarship Council for their financial support.

In all, sincere thanks to all my friends and family who give me support, help and love throughout my life.

Abstract

Five large pore crystalline zirconium-based metal-organic frameworks (Zr-MOFs) of different pore sizes (6-30 Å) and structure were synthesized and used for the preparation of the Rh-supported catalysts Rh@UiO-66, Rh@UiO-67, Rh@MOF-808, Rh@DUT-67 and Rh@NU-1000. The materials were characterized by XRD, FTIR, SEM/TEM, XPS, TGA, and nitrogen adsorption/desorption measurements. The catalytic performance was studied in the hydroformylation of olefins to the corresponding aldehydes. A series of *n*-alk-1-enes of different chain length and bulky olefins with different size was used to study the influence of the pore size and structure. The results show that the Zr-MOF-based catalysts are very active and show high aldehyde selectivity. The superior catalytic properties are assigned to the presence of highly dispersed active Rh-single sites located at the isolated zirconia moieties and organic linker. Markedly differences in the catalytic performance of the catalysts are observed, which are assigned to the different pore size and accessibility of Rh active sites.

List of figures.....	VII
List of schemes	XI
List of tables.....	XII
List of abbreviations	XIII
1. Introduction.....	1
1.1 Research issue	1
1.2 Goals and objectives.....	3
1.3 Background	4
1.3.1 Hydroformylation	4
1.3.2 Metal-organic framework (MOF).....	9
1.3.2.1 Structure of metal-organic frameworks	10
1.3.2.3 Synthesis and design of MOFs	12
1.3.2.4 Catalytic application of metal-organic frameworks	14
1.4 State-of-the-art.....	15
1.4.1 Metal nodes as catalytic sites.....	15
1.4.2 Catalytic sites incorporated in organic ligands.....	16
1.4.3 Catalytic moieties encapsulated in the pore space.....	17
1.4.4 Hydroformylation with Rh-supported heterogeneous porous catalysts.....	17
1.5 Structure and porosity of investigated Zr-MOFs.....	19
1.5.1 Metal-organic framework UiO-66 and UiO-67	19
1.5.2 Metal-organic framework MOF-808	20
1.5.3 Metal-organic framework DUT-67	22
1.5.4 Metal-organic framework NU-1000.....	23
2. Experimental part.....	25
2.1 Reagents	25
2.2 Synthesis of MOFs	26
2.2.1 Synthesis of UiO-66 and UiO-67	26
2.2.2 Synthesis of MOF-808	26
2.2.3 Synthesis of DUT-67	26
2.2.4 Synthesis of NU-1000	27

2.2.4.1	Synthesis of organic linker	27
2.2.4.2	Synthesis of the MOF	28
2.3	Preparation of rhodium supported Zr-MOF catalysts.....	29
2.4	Characterization of materials.....	29
2.5	Catalytic testing.....	31
2.5.1	Catalytic testing with single olefins.....	31
2.5.2	Catalytic testing with mixture of olefins	32
2.5.3	Analysis of catalytic products	32
3.	Results and discussion	35
3.1	Hydroformylation of olefins over Rh-supported Zr-MOF UiO-66, UiO-67, and MOF-808.....	35
3.1.1	Characterization.....	35
3.1.2	Catalysis	45
3.1.3.1	Hydroformylation of linear <i>n</i> -alk-1-enes.....	45
3.1.3.2	Catalytic testing with bulky olefins	55
3.1.3.3	Catalytic testing with linear olefin mixtures.....	57
3.1.4	Summary	61
3.2	Hydroformylation of olefins over Rh-supported Zr-MOF DUT-67.....	63
3.2.1	Characterization.....	63
3.2.2	Catalysis	68
3.2.2.1	Hydroformylation of linear <i>n</i> -alkenes	68
3.2.2.2	Hydroformylation of bulky olefins.....	72
3.2.3	Summary	72
3.3	Hydroformylation of olefins over Rh-supported Zr-MOF NU-1000	74
3.3.1	Characterization.....	74
3.3.2	Catalysis	77
3.3.2.1	Hydroformylation of linear <i>n</i> -alk-1-enes.....	77
3.3.2.2	Hydroformylation of bulky olefins.....	80
3.3.3	Summary	81
3.4	Structure - catalytic property - relationships in the hydrofomylation over Zr-MOFs ...	83

4. Conclusion	85
Reference	88

List of figures

Figure 1. Metal nodes, organic linkers, and framework topology of UiO-66, UiO-67, MOF-808, DUT-67 and NU-1000.....	3
Figure 2. Mechanism of the rhodium catalyzed hydroformylation of olefins to aldehydes.....	8
Figure 3. Influence of temperature on the hydroformylation of <i>n</i> -hexene using Rh ₄ (CO) ₁₂ as catalysts.....	8
Figure 4. (a) A series of metal-organic framework materials with different lengths of ligands. (b) Functionalized organic MOF ligands.	12
Figure 5. Schematic diagram of representative MOFs constructed by different secondary structural units and rigid connecting rods.	13
Figure 6. One-dimensional, two-dimensional, and three-dimensional network structure formed by metal nodes and organic linkers.	13
Figure 7. Schematic representation of the structures of MOF catalysts, and the catalytic site locations on/in different essential constituent elements of MOFs – metal node, organic linker, insertion of active components into the pores.	15
Figure 8. (a) One unit cell of copper drawn to scale with: (b) Zr-MOF with 1,4-benzene -dicarboxylate (BDC) as linker, UiO-66, (c) Zr-MOF with 4,4'-biphenyl- dicarboxylate (BPDC) as linker, UiO-67. Zirconium, oxygen, carbon, and hydrogen atoms are red, blue, gray, and white, respectively.	19
Figure 9. Structures (a) and (d) show the inner core Zr ₆ -cluster drawn alone for clarity, in hydroxylated and dehydroxylated form, and the symmetry change from Td (-43 m) to D _{3d} (-3 m) when the two μ ₃ -OH groups are removed. Structures (b) and (e) show the full cluster to illustrate the change in zirconium coordination from 8 to 7 upon dehydration. Zirconium, oxygen, carbon and hydrogen atoms are red, blue, gray, and white, respectively.	20
Figure 10. Zr ₆ O ₄ (OH) ₄ (-CO ₂) ₆ (HCOO) ₆ secondary building units (SBUs) are combined with BTC linkers to form MOF-808, which has a porous, three-dimensional framework containing large adamantane shaped cages (open) and small tetrahedral cages (filled with green spheres).	21
Figure 11. (a) Packing diagram with pores location (red sphere, cuboctahedral pore; yellow spheres, octahedral pores) and (b) Zr ₆ O ₆ (OH) ₂ (CH ₃ COO) ₁₀ cluster inside the cuboctahedral pore (disorder neglected).	22
Figure 12. Synthesis of NU-1000 from TBAPy and ZrOCl ₂ with benzoic acid as modulator. NU-1000 (2.5 g) can be prepared in one reaction.....	24
Figure 13. The two-step synthesis of the tetra acid ligand for NU-1000 can be accomplished in 3d with an overall yield of 55% to produce H ₄ TBAPy (2) without the need for chromatographic purification.	27

Figure 14. High pressure PARR reactor used for hydroformylation of olefins.	33
Figure 15. Signals of main products in the hydroformylation of <i>n</i> -hexene at (a) 0h and (b) 21h.....	34
Figure 16. Simulated XRD pattern (bottom) and PXRD patterns of synthesized (top) and Rh-supported (middle) MOFs (a) UiO-66, (b) UiO-67 and (c) MOF-808.....	36
Figure 17. FTIR spectra of as-synthesized and Rh-supported (a) UiO-66, (b) UiO-67, and (c) MOF-808.	37
Figure 18. SEM images at 500, 5k and 50k magnification (top) and TEM images (bottom) of supported Zr-MOF catalysts: (a) Rh@UiO-66, (b) Rh@UiO-67 and (c) Rh@MOF-808.	39
Figure 19. XPS spectra of (a) O1s signal of as-synthesized and Rh-supported UiO-66, (b) Zr3p signal of as-synthesized and Rh-supported UiO-67 and (c) Zr3p signal of as-synthesized and Rh-supported MOF-808.	40
Figure 20. N ₂ adsorption and desorption isotherms of (a) synthesized and Rh-supported (a) UiO-66, (b) UiO-67, and (c) MOF-808.....	42
Figure 21. Thermogravimetric weight loss curves (TGA) of (a) UiO-66, (b) UiO-67 and (c) MOF-808 in the argon atmosphere.....	44
Figure 22. Conversion of the <i>n</i> -hexene, <i>n</i> -octene, <i>n</i> -decene, <i>n</i> -dodecene, and <i>n</i> -hexadecene in the hydroformylation over: (a) Rh@UiO-66, (b) Rh@UiO-67, and (c) Rh@MOF-808 in dependence on the reaction time.	47
Figure 23. Schematic drawing of the pore windows of (a) Rh@UiO-66, (b) Rh@UiO-67 and (c) Rh@MOF-808.....	48
Figure 24. Selectivity to aldehydes in the hydroformylation of <i>n</i> -hexene, <i>n</i> -octene, <i>n</i> -decene, <i>n</i> -dodecene, and <i>n</i> -hexadecene over (a) Rh@UiO-66, (b) Rh@UiO-67, and (c) Rh@MOF-808 in dependence on the reaction time.	50
Figure 25. Yield of aldehydes in the hydroformylation of <i>n</i> -hexene, <i>n</i> -octene, <i>n</i> -decene, <i>n</i> -dodecene, and <i>n</i> -hexadecene in dependence on the reaction time over (a) Rh@UiO-66, (b) Rh@UiO-67, and (c) Rh@MOF-808.....	51
Figure 26. Composition of the reaction mixtures obtained with different Rh-supported Zr-MOF catalysts (a) 50% and (b) 100% conversion in the hydroformylation of <i>n</i> -hexene.	53
Figure 27. <i>n/i</i> -aldehyde ratio in the hydroformylation of <i>n</i> -alkenes of different chain lengths over (a) Rh@UiO-66, (b) Rh@UiO-67 and (c) Rh@MOF-808.....	54
Figure 28. Pores and super tetrahedral cages of (a) UiO-66, (b) UiO-67, and (c) MOF-808. Proposed location of Rh active sites (yellow points) in the MOF pores.	55

Figure 29. Yield of aldehyde in the hydroformylation of 3,3-dimethyl-1-butene, 4-methylstyrene, cyclooctene, cyclohexene, and 2,4,4-trimethylpentene over (a) Rh@UiO-66, (b) Rh@UiO-67 and (c) Rh@MOF-808 in dependence on the reaction time.	56
Figure 30. Hydroformylation with (a) single olefin and (b) mixture olefins of <i>n</i> -hexene, <i>n</i> -decene and <i>n</i> -hexadecene catalyzed by Rh@UiO-66. Hydroformylation with (c) single olefin and (d) mixture olefins of <i>n</i> -hexene, <i>n</i> -decene and <i>n</i> -hexadecene catalyzed by Rh@UiO-67.	58
Figure 31. Simplified channel and linker orientation of (a) UiO-66 and (b) UiO-67.	59
Figure 32. Comparison of the catalytic performance (conversion, aldehyde yield and <i>n/i</i> -aldehyde ratio) of <i>n</i> -hexene in the hydroformylation with (a) Rh(acac)(cod), (b) Rh@UiO-66 and (c) leached solution.	60
Figure 33. Simulated XRD pattern (bottom) and PXRD patterns of synthesized (top) and Rh-supported (middle) DUT-67.	64
Figure 34. FTIR spectra of as-synthesized and Rh-supported Zr-MOF DUT-67.	64
Figure 35. SEM images of Rh-supported DUT-67 at (a) 5k and (b) 50k magnification, and (c) TEM images of Rh-supported DUT-67 with marked pore sizes.	65
Figure 36. N ₂ adsorption and desorption isotherms of as-synthesized and Rh-supported DUT-67.	66
Figure 37. XP spectra of (a) S _{2s} signal of as-synthesized and Rh-supported DUT-67, and (b) Rh _{3d} signal of Rh-supported Zr-MOF DUT-67.	67
Figure 38. Thermogravimetric weight loss curves (TGA) of DUT-67 in the argon atmosphere.	67
Figure 39. Conversion of the <i>n</i> -hexene, <i>n</i> -octene, <i>n</i> -decene, <i>n</i> -dodecene, and <i>n</i> -hexadecene in the hydroformylation over Rh@DUT-67 in dependence on the reaction time.	69
Figure 40. (a) Selectivity to aldehydes in the hydroformylation of <i>n</i> -hexene, <i>n</i> -octene, <i>n</i> -decene, <i>n</i> -dodecene, and <i>n</i> -hexadecene over Rh@DUT-67 in dependence on the reaction time. (b) Composition of the reaction mixtures obtained in the hydroformylation of <i>n</i> -hexene (left) and <i>n</i> -decene (right) over Rh@DUT-67 catalyst.	69
Figure 41. Yield of aldehydes in the hydroformylation of <i>n</i> -hexene, <i>n</i> -octene, <i>n</i> -decene, <i>n</i> -dodecene, and <i>n</i> -hexadecene over Rh@DUT-67 in dependence on the reaction time.	70
Figure 42. <i>n/i</i> -aldehydes ratio of <i>n</i> -hexene, <i>n</i> -octene, <i>n</i> -decene, <i>n</i> -dodecene and <i>n</i> -hexadecene in the hydroformylation over Rh@DUT-67 in dependence on the reaction time.	71
Figure 43. Re-usability of Rh@DUT-67 catalyst in the hydroformylation of <i>n</i> -hexene.	71

Figure 44. Yield of aldehyde in the hydroformylation of 3,3-dimethyl-1-butene, 4-methylstyrene, cyclooctene, cyclohexene, and 2,4,4-trimethylpentene over Rh@DUT-67 in dependence on the reaction time.....	72
Figure 45. Simulated XRD pattern (bottom) and PXRD patterns of synthesized (top) and Rh-supported (middle) NU-1000.	74
Figure 46. FTIR spectra of as-synthesized and Rh-supported NU-1000.	75
Figure 47. N ₂ adsorption and desorption isotherms of starting (black) and Rh-supported NU-1000 (red).	76
Figure 48. Thermogravimetric weight loss curves (TGA) of NU-1000 in the argon atmosphere.	76
Figure 49. XPS spectra of Zr _{3p} signal of as-synthesized and Rh-supported NU-1000.	77
Figure 50. Conversion of <i>n</i> -hexene, <i>n</i> -octene, <i>n</i> -decene, <i>n</i> -dodecenenem, and <i>n</i> -hexadecene in the hydroformylation over Rh@NU-1000 in dependence on the reaction time.	78
Figure 51. Selectivity to aldehydes in the hydroformylation of <i>n</i> -hexene, <i>n</i> -octene, <i>n</i> -decene, <i>n</i> -dodecene, and <i>n</i> -hexadecene over Rh@NU-1000 in dependence on the reaction time.....	79
Figure 52. (a) Yield of aldehydes with <i>n</i> -hexene, <i>n</i> -octene, <i>n</i> -decene, <i>n</i> -dodecene and <i>n</i> -hexadecene in dependence on the reaction time over Rh@NU-1000. (b) Composition of the reaction mixtures obtained in the hydrofromylation with <i>n</i> -hexene (left) and <i>n</i> -decene (right) over Rh@NU-1000 catalyst.....	80
Figure 53. <i>n/i</i> -aldehydes ratio of <i>n</i> -hexene, <i>n</i> -octene, <i>n</i> -decene, <i>n</i> -dodecene and <i>n</i> -hexadecene in the hydroformylation over Rh@NU-1000 in dependence on the reaction time.	80
Figure 54. Yield of aldehyde in the hydroformylation of 3,3-dimethyl-1-butene, 4-methylstyrene, cyclooctene, cyclohexene, and 2,4,4-trimethylpentene over Rh@NU-1000 in dependence on the reaction time.....	81
Figure 55. The composition in the reaction mixture over <i>n</i> -hexene and <i>n</i> -decene after 21h.	84

List of schemes

Scheme 1. Reaction scheme of the hydroformylation of olefins over Rh-catalysts.	5
Scheme 2. Process of i) isomerization and ii) hydrogenation.	5
Scheme 3. The reactivity of different olefins in the hydroformylation.	6
Scheme 4. Products derived from aldehydes.....	6

List of tables

Table 1. The specifications of the main reagents	25
Table 2. Binding energies of carbon, oxygen and zirconium in the XP spectra of the as-synthesized and Rh-supported UiO-66, UiO-67 and MOF-808.	41
Table 3. BET surface area and pore volumes (PV) of as-synthesized and Rh-supported Zr-MOFs UiO-66, UiO-67, and MOF-808.	43
Table 4. Binding energies of carbon, oxygen, sulfur, zirconium and rhodium in the XP spectra of the as-synthesized and Rh-supported DUT-67.....	67
Table 5. Binding energies of carbon, oxygen, zirconium and rhodium in the XP spectra of the as-synthesized and Rh-supported NU-1000.	77
Table 6. The amount of <i>i</i> -alkenes in in the reaction mixture over <i>n</i> -hexene and <i>n</i> -decene after 21h.....	84

List of abbreviations

Abbreviation	Full name
MOF	Metal-organic framework
Rh(acac)(cod)	(Acetylacetonato)(cycloocta-1,5-diene) rhodium (I)
DMF	Dimethylformamide
NMP	Methylpyrrolidone
H₂BDC	1,4-Benzenedicarboxylic acid
H₃BTC	Benzene-1,3,5-tricarboxylic acid
H₂BPDC	Biphenyl-4,4' -dicarboxylic acid
H₂TDC	2,5-Thiophenedicarboxylic acid
H₄TBAPy	4,4',4'',4'''-(pyrene-1,3,6,8-tetrayl) tetrabenzoic acid
DMB	3,3-dimethyl-1-butene
TMP	2,4,4-trimethyl-1-pentene
PXRD	Powder X-ray diffraction
FTIR	Fourier transform infrared spectroscopy
BET	Brunauer-Emmett-Teller
TGA	Thermogravimetric analysis
SEM	Scanning electron microscopy
TEM	Transmission electron microscopy
XPS	X-ray photoelectron spectroscopy
SBU	Secondary building unit
DFT	Density functional theory

1. Introduction

1.1 Research issue

The hydroformylation (or oxo reaction) of olefins with synthesis gas to aldehydes was discovered by Otto Roelen in 1938. It is one of the most important fine chemical reactions¹⁻⁵. After decades of research, rhodium complexes were proved to be the most active catalysts. Currently, homogeneous catalysts are used in the commercial hydroformylation because of their high activity and selectivity. However, this process suffers from separating of the expensive catalyst from the reaction mixture. Therefore, the development of heterogeneous catalysts is of interest. Many reports on the immobilization of Rh-complexes on porous supports like silica, zeolites, polymers, and activated carbon are available. Besides the obtained progress, the achieved catalytic performance of these catalytic materials is still not sufficient.

Metal-organic frameworks are a new class of open porous materials composed of strictly alternating metal units connected by organic linkers. The variety of chemical compositions and possible 3-dimensional connections between inorganic units and organic linkers lead to diverse structures with large and accessible pores. Different metal nodes and organic linker offer multiple possibilities for functionalization. They show superior high porosity – large specific surface areas and specific pore volumes, and a large range of controlled defined pore sizes facilitating mass transfer. Due to their hybrid nature, MOFs combine both hydrophobic and hydrophilic properties. The strictly alternative arrangement of the hydrophilic inorganic metal nodes and hydrophobic organic linker allow catalytic site separation, i.e. site isolation useful for the preparation of so-called single site catalysts. They show superior catalytic activity. These unique features make MOFs ideal host matrices for the immobilization of catalytic active complexes and the preparation of heterogeneous supported catalysts. Therefore, the incorporation of transition metal complexes into MOFs was considered in recent efforts. Currently, a couple of metal nanoparticles such as Cu, Ru, Pd, and Pt were used to prepare different MOF-supported catalysts. These materials were catalytic active e.g. in oxidation, reduction, hydrogenation, and photo catalysis⁶⁻¹².

Rh-loaded MOFs were tested mostly in the hydrogenation. Only very few reports deal with the hydroformylation of olefins with Rh-loaded metal-organic frameworks such as ZIF-8, MIL-101, and IRMOF-3¹³⁻¹⁵. Zirconium-based MOFs are of interest

for the preparation and testing of supported catalysts due to its outstanding stability, the quite large surface area and the extended pore size ranging from micro- to mesopores. To the best of our knowledge, the catalytic performance of Rh-loaded large pore Zr-MOFs in the hydroformylation of olefins was not investigated so far. There are some reports dealing with Cu-, Rh-, and Nb-supported Zr-MOF-catalysts used in CO oxidation, hydrogenation, and cyclohexene epoxidation^{7,16,17}.

In order to study the catalytic performance of Zr-MOFs with different pore sizes, five different zirconia based MOFs: UiO-66, UiO-67, MOF-808, DUT-67, and NU-1000 were chosen as representative materials (Figure 1). The metal-organic framework UiO-66 has the same topology as UiO-67, which framework is formed by tetrahedral and octahedral cages. However, UiO-67 contains the longer biphenyl linker (H₂BPDC) whereas UiO-66 contains the shorter benzene dicarboxylate linker (H₂BDC). Therefore, UiO-67 has a larger pore size. The framework of MOF-808 contains large pores formed by 6 surrounding tetrahedral cages. The tripod benzene tricarboxylate linker (H₃BTC) is located on the face of the cage. Compared to UiO-66, the connectivity of the inorganic nodes of DUT-67 decreases from 12 to 8 and contains a bent 2,5-thiophenedicarboxylate (H₂TDC) linker. The framework contains larger cubooctahedral units providing larger pores. The inorganic nodes of NU-1000 are the same as with DUT-67 and are also 8 connected. But the pore size increases largely and the topology changes due the utilization of the extra-large pyrene tetra benzene carboxylate linker (H₄TBAPy).

Here in, the catalytic performance of Rh-supported large pore Zr-MOF catalysts of different porosity in the hydroformylation of olefins will be investigated. For this purpose, rhodium supported zirconium-based MOFs UiO-66, UiO-67, MOF-808, DUT-67, and NU-1000 were prepared and characterized by PXRD, FTIR, SEM/TEM, XPS, and nitrogen adsorption. The catalytic performance was studied using linear olefins with different chain lengths (*n*-hexene, *n*-octene, *n*-decene, *n*-dodecene and *n*-hexadecene) and bulky olefins with different molecular size (2,4,4-trimethylpentene, 3,3-dimethyl-1-butene, 4-methylstyrene, cyclohexene and cyclooctene) as model substances.

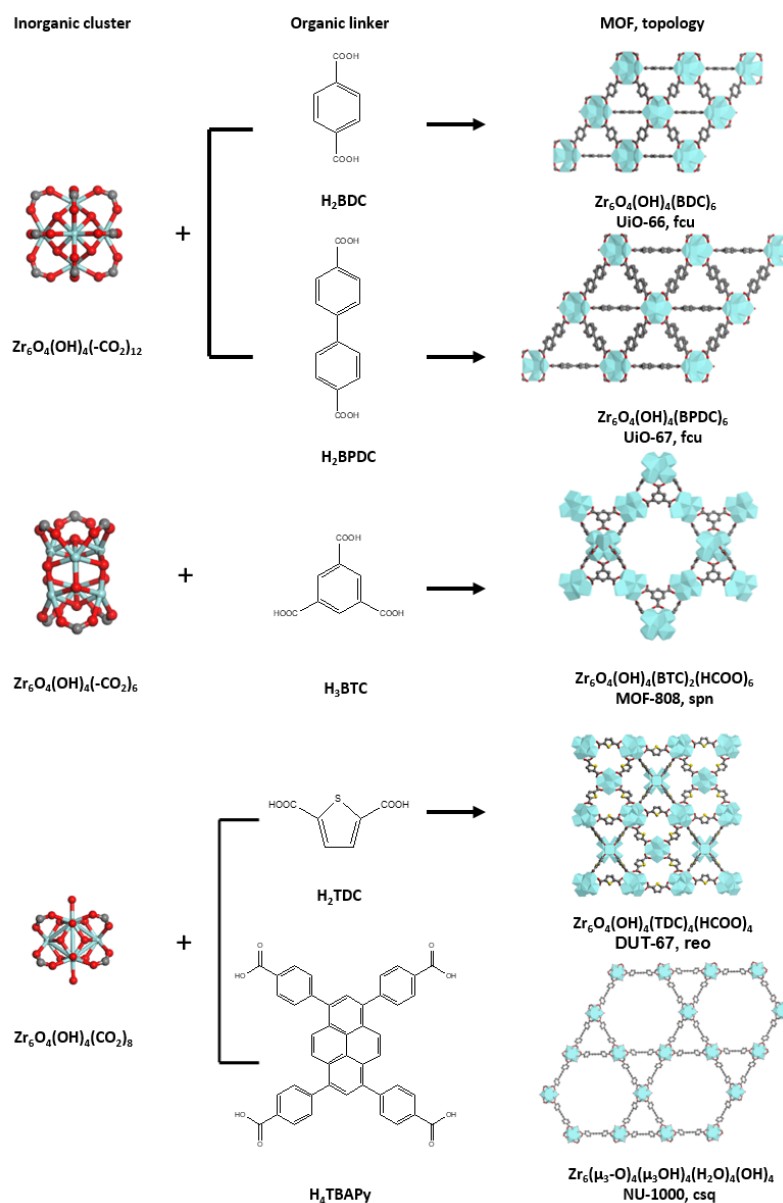


Figure 1. Metal nodes, organic linkers, and framework topology of UiO-66, UiO-67, MOF-808, DUT-67 and NU-1000.

1.2 Goals and objectives

The work aims to

- Prepare advanced large pore Rh-supported Zr-MOFs catalysts and its characterization regarding catalytic relevant properties as crystallinity, particle morphology, specific surface area, pore size and pore volume, loading and the location and stability of catalytic active rhodium component,

- Study of the catalytic performance, i.e. activity selectivity, and its potential for the application in the hydroformylation of different olefins including large molecules like hexadecene,
- Investigate Structure-Property- Relationships, i.e. the influence the of pore structure, pore size and pore volume on the catalytic performance in the hydroformylation of olefins.

The objectives of the work are:

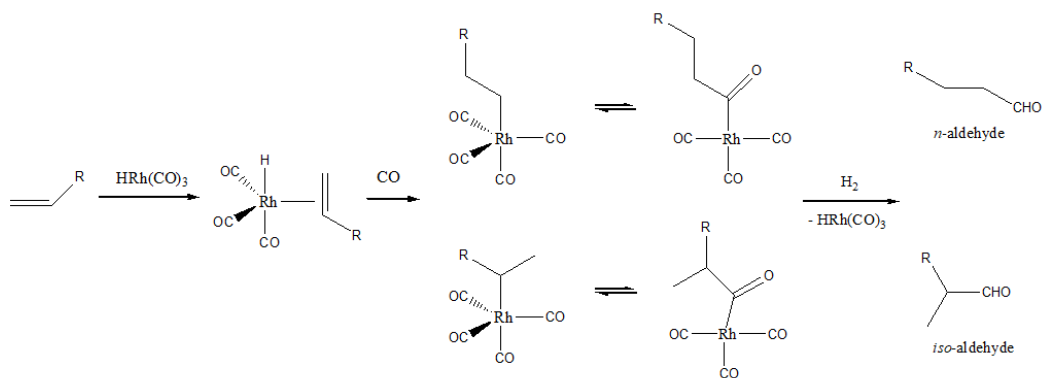
- Preparation of five Zr-MOFs UiO-66, UiO-67, MOF-808, DUT-67 and NU-1000 as small, medium, large and extra-large pore-sized MOFs covering pore size range of 6 Å to 30Å. Specially, DUT-67 contains a heteroatom substituted organic linker providing a high accessible active site,
- Characterization of structural and textural properties of Zr-MOFs and corresponding Rh-supported Zr-MOF catalysts PXRD, SEM/TEM, FTIR, N₂-adsorption/desorption, TGA, and XPS,
- Investigation of the catalytic performance in the hydroformylation with different different *n*-alkenes including *n*-hexene, *n*-octene, *n*-decene, *n*-dodecene and *n*-hexadecene as model substances,.
- Investigation of the catalytic performance in the hydroformylation with bulky olefins including 2,4,4-trimethylpentene, 3,3-dimethyl-1-butene, 4-methylstyrene, cyclohexene, and cyclooctene as model substances,
- Testing of the catalyst stability, e.g. leaching test and re-usability using Rh@UiO-66 and Rh@DUT-67 as model catalysts and *n*-hexene as test molecule.

1.3 Background

1.3.1 Hydroformylation

In 1930, D.F. Smith and others discovered that the reaction of ethylene and water gas could result in the formation of aldehydes and alcohols under the action of cobalt catalysts. This discovery spurred the development and research on the synthesis of high-carbon alcohols (chain lengths C12 to C14)¹⁸. Until 1938, the hydroformylation was discovered by chance by Otto Roelen^{19,20}. After 20 years

break, the research on hydroformylation restarted at the end of 1950's¹. The Hydroformylation was also called aldolization of oxo synthesis. It refers to the reaction of carbon monoxide, hydrogen and olefins in the presence of a catalyst under pressure to aldehydes with one carbon atom more than the original olefin. It is the reaction of olefinic double bonds with CO and H₂, yielding a mixture of linear and branched aldehydes, Scheme 1)^{2,3,20,21}.



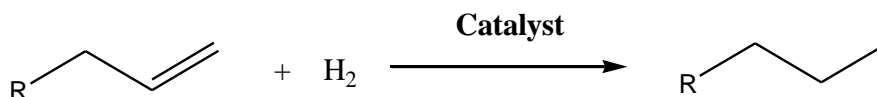
Scheme 1. Reaction scheme of the hydroformylation of olefins over Rh-catalysts.

Double-bond isomerization (shift) is always observed as a fast side reaction in the hydroformylation. It leads to the formation *i*-aldehydes. This side reaction is difficult to avoid even though only terminal *n*-alk-1-enes as starting materials. Besides, hydrogenation may also happen (Scheme 2).

(i) Isomerization of *n*-alkene to *i*-alkene (double bond shift):



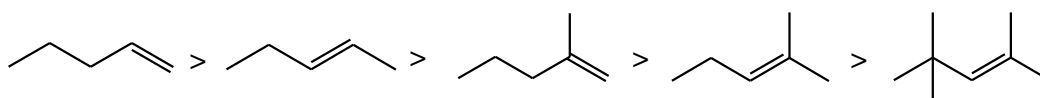
(ii) Hydrogenation:



Scheme 2. (i) isomerization and ii) hydrogenation of terminal *n*-alkenes.

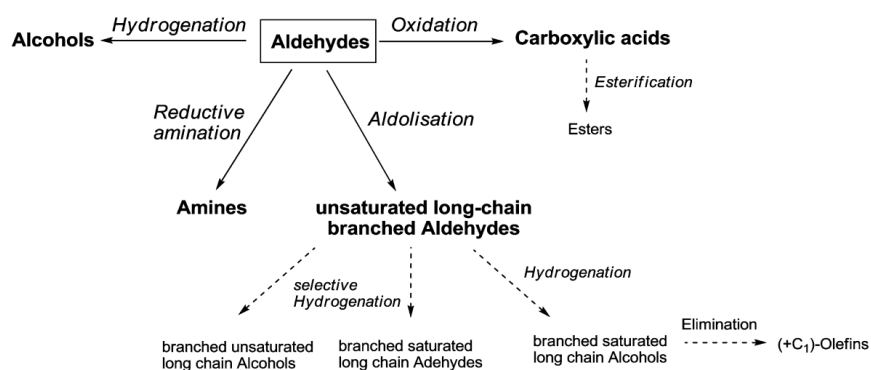
Due to the occurrence of the competing double bond shift side reaction and following formation of *i*-aldehydes beside of wished terminal *n*-aldehydes, the regioselectivity is an important parameter of the catalytic performance of catalysts in hydroformylation reaction. Usually it is expressed as *n*/*i*-aldehyde ratio. It depends on the catalyst,

ligands and reaction conditions. The selectivity varies with different catalysts. The yield of *n*-aldehydes, i.e. the efficiency of the hydroformylation depends on the selectivity and activity (conversion) of the catalyst. In addition, also the reactivity of the starting olefins is of importance. In general, the terminal linear olefins such as *n*-butene, *n*-hexene are more active than branched olefins. The order of reactivity of unsaturated substrates is shown in Scheme 3²².



Scheme 3. The reactivity of different olefins in the hydroformylation.

The obtained aldehydes are viewed as valuable final products. These products are more preferred to be used for the production of alcohols via hydrogenation, amines via reductive amination and carboxylic acid via oxidation. Besides, further aldolisation of the primary generated aldehydes can be also used in the synthesis of branched saturated/unsaturated long chain alcohols. Nearly 9 million metric tons of aldehydes and alcohols are produced per year by hydroformylation. The products are highly valuable for the synthesis of solvents, detergents, adhesives, plasticizers, agrochemicals and pharmaceuticals. Main products derived from aldehydes are shown in Scheme 4².



Scheme 4. Products derived from aldehydes.

The hydroformylation proceeds only in the presence of a catalyst. Typical catalysts used in the hydroformylation of olefins are mostly homogeneous transition and

noble metal M complexes with active species of the type $[HM(CO)_xL_y]$, where the ligand L can be substituted by further CO groups or other organic ligands. Moreover, the activity of the catalyst differs when the metal atoms is changed. A generally accepted order of the activities for unmodified monometallic catalysts is:



Currently, all the works proved that only rhodium and cobalt are valuable in industrial practice. Before 1970's, catalysts with cobalt as metal site dominated industrial hydroformylation completely²⁴. After that rhodium catalysts were partly commercialized and its unparalleled activity has received widespread attention. In 1995, almost 80% of all homogeneous hydroformylation processes are carried out in the system with the rhodium catalysts³.

A general mechanism for the hydroformylation of a vinyl substrate is shown in Figure 2²⁵. In the first stage, rhodium precursor reacts with synthesis gas to form a highly active rhodium hydride tricarbonyl species. Then these species coordinate the substrate and generate the π -complex. After that the π -complex tends to rearrange through insertion of the alkene into the Rh-H bond generating a more stable alkyl-rhodium intermediate. The second stage is a two-step addition reaction with synthesis gas. Migratory insertion of the alkyl moiety on to a CO molecule coordinated to rhodium and provides the acyl-rhodium species, which interact with H_2 through oxidative addition at the end of the reaction. Thus aldehydes and regenerated rhodium hydride species are formed. Thereby a complete catalytic cycle is achieved.

Systematic investigation on the effect of reaction conditions on the regioselectivity in the hydroformylation of olefins was carried out in the presence of unmodified rhodium-based complexes. It is worth noting that both hydroformylation and double bond isomerization were enhanced as the temperature of the reaction increased. In the case of *n*-octene in the presence of (acetylacetonato) dicarbonyl rhodium (I), the *n*/*i* aldehyde ratio increased slightly from 1.5 to 2.1 when the temperature increased from 50 to 90 °C²⁶. However, due to the isomerization the amount of internal octenes increased from 3% to 24% at the same time. Other investigations considered the hydroformylation of styrene, ethyl- and allyl ethers and 1-hexene with $Rh_4(CO)_{12}$ at temperatures between 20 and 100 °C. As shown in Figure 3, the yields

of linear aldehyde increased in all the cases. The reaction temperature has obvious a promoting effect on the hydroformylation of olefins.

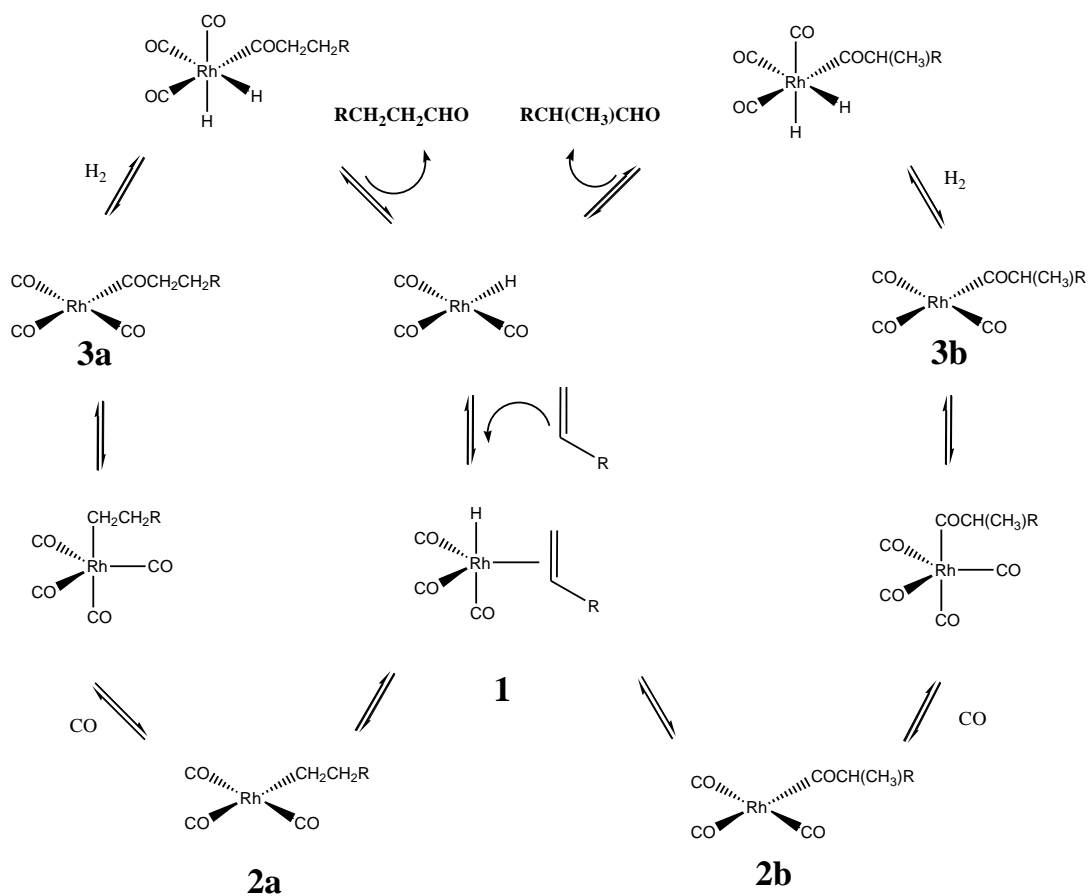


Figure 2. Mechanism of the rhodium catalyzed hydroformylation of olefins to aldehydes.

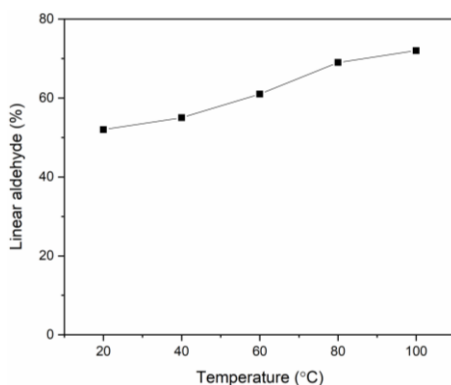


Figure 3. Influence of temperature on the hydroformylation of *n*-hexene using Rh₄(CO)₁₂ as catalysts.

Also the CO and H₂ partial pressure affect the regioselectivity of the hydroformylation. In the case of styrene, an increase of the yield of linear aldehydes was observed when CO or H₂ partial pressure decreased and the reaction was carried out at high temperature. This effect was more evident at higher temperature of 100 °C. Specifically, in the hydroformylation of styrene, when the partial pressure ranges from 170 bar of CO/H₂ (1:1) to $P_{CO}=85$ bar and $P_{H_2}=6$ bar or $P_{CO}=6$ bar and $P_{H_2}=85$ bar, the *n/i*-aldehyde ratio increases from 20/80 to 56/44 or 60/40, respectively. However, this effect could not be observed in the reaction with *n*-hexene. In contrast, the aldehyde selectivity increased with increasing temperature. At the same time, the aldehyde/*i*-olefins ratio increased from 44/56 at 40 bar to 77/23 at 140 bar.

Apart from temperature and CO/H₂ partial pressure, proper solvent can also improve the reaction efficiency. In the hydroformylation of olefins, solvents are always used to solubilize the reactants. In addition, solvents enable the reaction to proceed in the liquid phase, which is beneficial for gas-liquid mass transfer into the reaction mixture (synthesis gas input). At the same time, solvents act as diluents, facilitate the heat transfer, and improve the control of the reaction temperature. Toluene is a preferred solvent. The solubility of H₂ and CO in common solvents is in the range of 2-10 mol m⁻³ bar⁻¹.

1.3.2 Metal-organic framework (MOF)

Porous materials are of high interest for the development new improved catalytic systems. They provide internal high specific surface area and pore volumes in interconnected intra-material pore systems. Specifically the understanding and tailor-made preparation of crystalline porous materials is of importance, because they provide pores of defined size and shape pore of molecular size. The research has experienced from zeolites, molecular sieves, mesoporous materials, macroporous materials and other inorganic to organic porous materials and inorganic-organic hybrid materials²⁷⁻⁴². They are of high potential in terms of catalysis, adsorption, separation, or ion exchange.

Metal-organic frameworks (MOFs) are a new type of porous materials that combine the functions and characteristics of both inorganic and organic polymers. It has not only a rich and diverse framework structure, high specific surface area and good

stability, but also the structure and properties of metal-organic framework materials are designable and controllable^{43,44}.

1.3.2.1 Structure of metal-organic frameworks

The structure of metal-organic framework (MOFs) is formed by a strict ordered, 3-dimensional, and alternating arrangement of metal moieties and organic linker into a crystalline framework. In case porous MOFs metal nodes form secondary building units which are connected by organic linker in an open way leaving an ordered intra-particle pore system of molecular size. Because the pores are a part of the crystal structure the size of pores, windows, channels and cages. Is well-defined and of molecular size. Also the structure of the secondary building unit (metal moiety formed from metal nodes, is well defined. Due to different interconnection of SBUs and linker structures of different topology are formed providing one-, two- and three-dimensional intra-crystalline pore systems. The size and shape of pores can be tailor-made modified by using different metals, metal moieties and linker molecules. Well selected modification of metal moieties and linker provide multiple functionalities^{45,46}.

The porous MOFs have emerged as an huge class of crystalline frameworks with ultrahigh porosity (up to 90% free volume) and quite large surface areas, which extending to maximum 6000 m²/g. Besides, the extraordinary degree of variability for both the organic and inorganic components of their structures provide MOFs tunable hybrid character, with combined hydrophilic and hydrophobic properties^{42,47-52}.

Research on metal-organic framework materials evolved from coordination chemistry. Back in 1706, the first three-dimensional network Prussian blue has discovered and widely used in the dye industry, but its structure was resolved only in 1977 by Ludi et al⁵³. In 1897, Hoffman et al. obtained a MOF-like coordination polymer by adding benzene to the ammonia solution of nickel cyanide⁵⁴. The structure of this coordination polymer was solved in 1952 analyzed by Powell et al by X-ray technology⁵⁵. Inspired by these classic coordination polymers, other building blocks, bridging ligands, stencil agents and guest molecules were explored to build new coordination polymer. After 1960s, with the improvements in characterization technology and the knowledge of recognition of coordination

polymers together with the introduction of the "crystal engineering" strategy have laid a foundation for the design and construction of coordination polymers. In 1989, Robson's group used 4,4',4'', 4'''-tetracyanobenzene methane (TCPM) ligands and cuprous ions to prepare cuprous cyano coordination polymers with diamond topology⁵⁶. This research not only extends Wells' work in inorganic network structures to the field of metal-organic coordination polymers for the first time, but also predicts that metal-organic coordination polymers may produce other molecular sieve topologies. In the mid-1990s, Yaghi's group deeply investigated coordination polymers based on carboxylic acid ligands⁵⁷⁻⁶². This series of work are of great significance for the development and construction of metal-organic frameworks with stable pore systems (Figure 4). After removing the guest molecules, these materials still maintain the stability of the framework and can also adsorb other guest molecules.

A huge amount of MOFs with different porosity and composition is now available and requires studies on possible application of MOFs e.g. in catalysis, adsorption, separation and purification processes, energy storage and others.

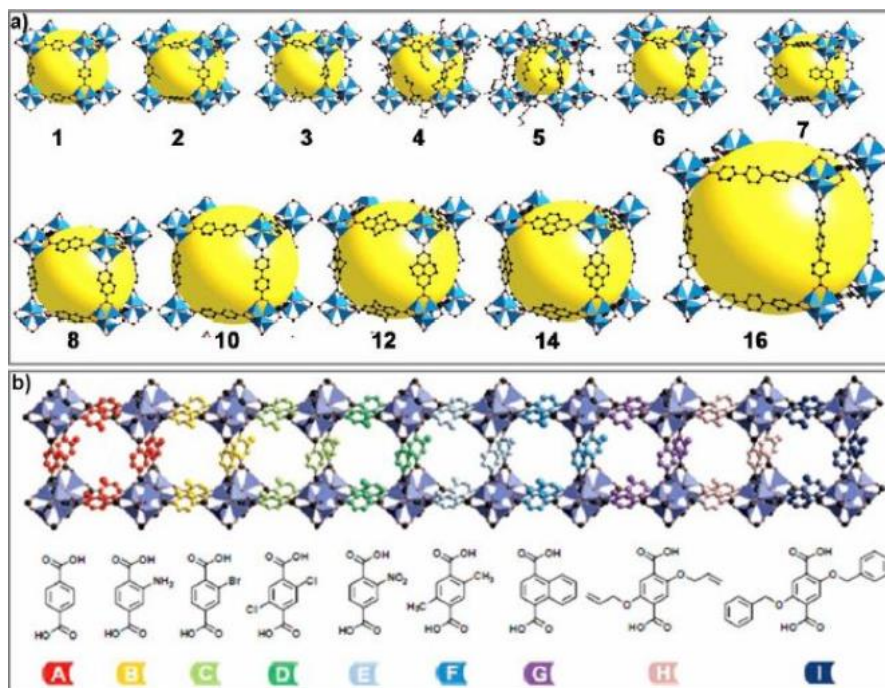


Figure 4. (a) A series of metal-organic framework materials with different lengths of ligands. (b) Functionalized organic MOF ligands.

1.3.2.3 Synthesis and design of MOFs

The synthesis of metal-organic frameworks include hydrothermal / solvothermal synthesis, solvent evaporation, vapor diffusion, or mechano-chemical preparation by milling of starting materials. Among these methods, MOFs synthesis under solvothermal conditions at low temperature (less than 250 °C) is mostly used. In general, metal source and organic ligands are added in the solution, mixed and heated in autoclaves or glass vessel for crystallization. The synthesis conditions such as pH, temperature, type solvent and template may affect the crystallization. By desired choice of metal ions and linker of different size and shape various MOF structures can be obtained. The inorganic part includes transition metal ions, high-valent transition metal ions, rare earth metal ions, alkali metal ions and alkaline earth metal ions⁶³⁻⁶⁵. The organic ligand part includes carboxylic acid ligands, heterocyclic ligands, phosphate ligands, mixed ligands of carboxylic acid ligands with nitrogen-containing ligands, and mixed ligands of dicarboxylic acids⁶⁶⁻⁶⁹.

The porosity can be additional modified by addition of non-bridging linker, i.e. monocarboxylic acids or blocking of coordination sites by mineral acids. The common polar organic solvents such as dimethyl/ethyl formamide (DMF), dimethyl sulfoxide (DMSO) and acetonitrile are always used in MOF thesis^{45,70-78}.

The concept of *iso*-reticular synthesis of MOFs was developed by Yaghi and co-workers the design of new structure types. It includes a systematic variation of linker size, shape and number of coordinating groups. In addition, a concept of variation of secondary building units (SBUs) was developed^{79,80} was developed and lead to this synthesis of Zn-based IRMOFs and new zirconia based MOFs. Thus a large series of MOF with same topology but different properties can be realized⁶¹ (Figure 1, 4, 5, and 6).

Theoretical models based on topology concepts were developed to predict new MOF structures in order to guide the MOF synthesis (Figure 5)⁷⁹⁻⁸³. Classification from the structure of metal-organic framework, MOFs consist of zero-dimensional cluster structure, one-dimensional chain structure, two-dimensional network structure, and three-dimensional framework structure (Figure 6).

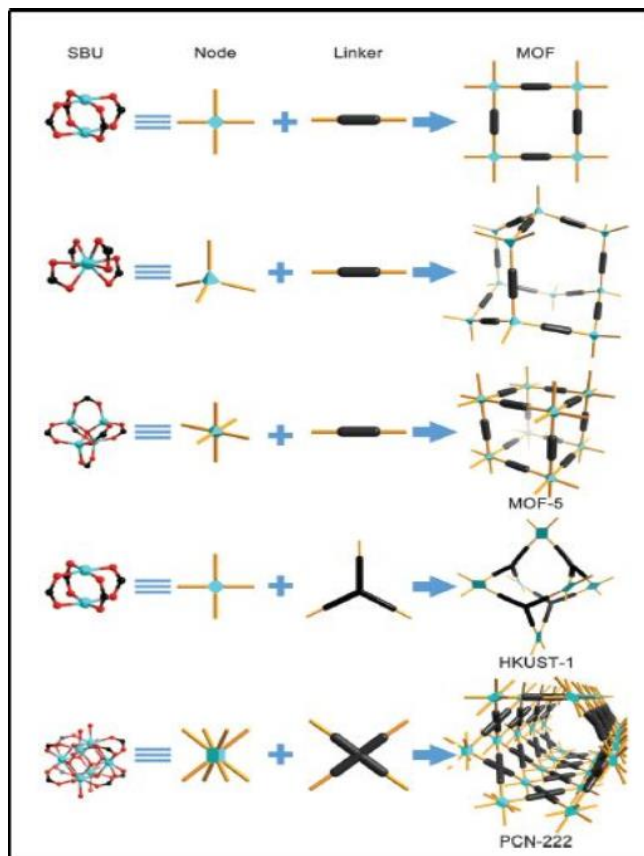


Figure 5. Schematic diagram of representative MOFs constructed by different secondary structural units and rigid connecting rods.

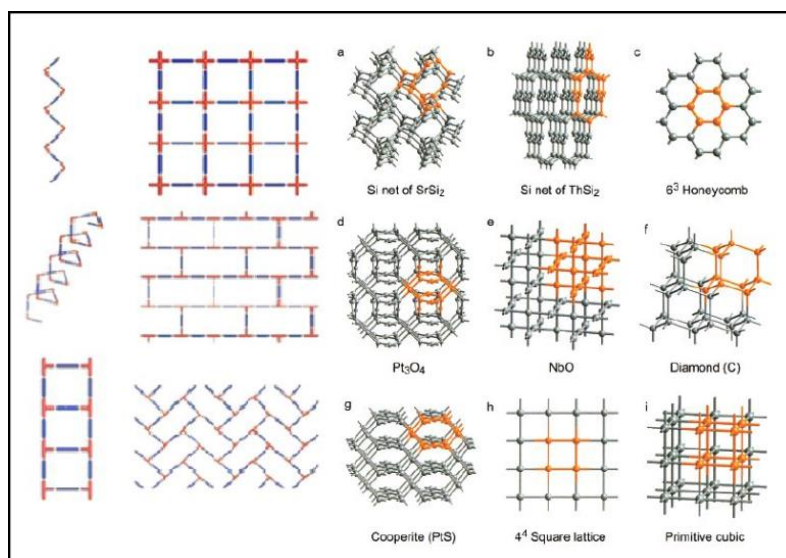


Figure 6. One-dimensional, two-dimensional, and three-dimensional network structure formed by metal nodes and organic linkers.

1.3.2.4 Catalytic application of metal-organic frameworks

Due to their unique superior properties as structural diversity, large controllable pore size and shape, hydrophobic –hydrophilic hybrid nature, site separation by strictly alternating arrangement of inorganic units and organic linkers, sufficient stability and possibly multiple functionality porous metal-organic frameworks have great perspectives for the application as heterogeneous catalysts, metal supported catalysts as well the immobilization catalytic components as homogeneous catalysts or biocatalysts and other applications^{9,43,84-100}.

Based on the special properties MOF catalysts may offer several superior characteristics:

- i) High density of separated sites due to the large surface area (up to 3000 m²g⁻¹) and corresponding high catalytic activity,
- ii) The large pore size MOFs facilitates the mass transfer and conversion of large molecules,
- iii) High accessibility of the active sites in the pore space due to open pore structure,
- iv) Site separation by alternating inorganic and organic parts enables the preparation of advanced isolated, highly active “single site” catalysts,
- v) The large pore size and pore volumes improve the heterogenization of homogeneous complex and immobilization of bio-catalysts.,
- vi) The high stability of Zr-MOFs enhances catalyst stability decreases leaching and improves recovery and re-usability ,and
- vii) Improved selectivity by “confinement effects” by limited space, shape and size of pores and windows.

These properties make Zr-MOFs superior candidates for the preparation of metal supported catalysts.

1.4 State-of-the-art

In terms of the catalytic properties of MOFs, three essential factors are of high value, i.e. inorganic nodes, organic ligands and pore space inside the framework. This allows the preparation of three basic types of catalysts:

- i) metal nodes are used as catalytic sites,
- ii) incorporation the catalytic sites on the organic ligands,
- iii) supporting active metal components or immobilization of catalytic moieties into the pore space of the framework, e.g. metal complexes or biocatalysts, by situ synthesis in one system or treated by post modification^{88,101}.

Hence, a high diversity of catalytic materials is available based on porous metal-organic frameworks (Figure 7).

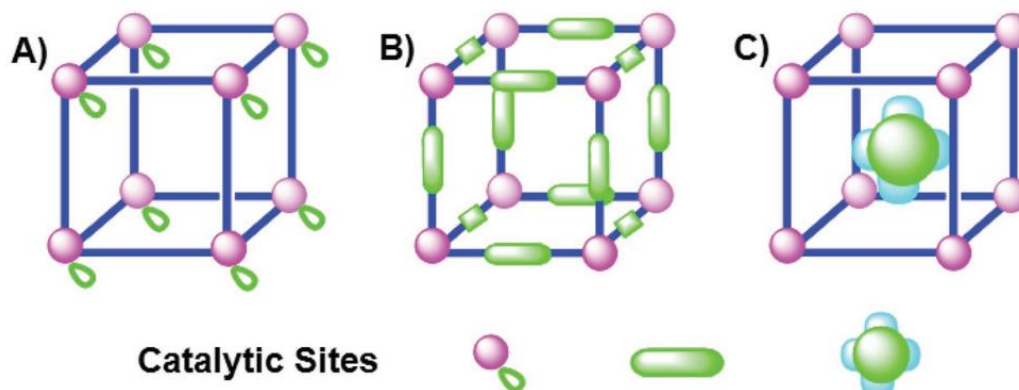


Figure 7. Schematic representation of the structures of MOF catalysts, and the catalytic site locations on/in different essential constituent elements of MOFs – metal node, organic linker, insertion of active components into the pores.

1.4.1 Metal nodes as catalytic sites

A large amount of MOFs have a certain degree of catalytic activity which depends on the catalytic properties of the metal nodes. In terms of catalytic performance, metal sites in MOF have the following features: i) The metal nodes can directly react with substrate molecules. ii) Uncoordinated metal atoms of the metal nodes can act as active sites. iii) Attachment of active components on uncoordinated metal sites by

replacement of loosely coordinated solvent molecules. iv) In the nodes of MOF frameworks, the metal ions can be isomorph substituted by a variety of catalytic active transition metals.

First metal sites of MOFs were used for catalytic reactions. Fujita et al. proved that the coordinative unsaturated Cd sites in the MOF $[\text{Cd}(4,4'\text{-bpy})_2](\text{NO}_3)_2$ at quite active in the catalytic reaction of cyanosilylation of aldehydes¹⁰². Similarly, the Lewis-acid sites of Cu^{2+} in the MOF-199 ($[\text{Cu}_3(\text{BTC})_2]$) were investigated and showed high catalytic efficiency in the cyanosilylation of benzaldehyde and cyanotrimethylsilane¹⁰³. This reaction was also catalyzed by the MOF MIL-101 ($[(\text{Cr}_3\text{F}(\text{H}_2\text{O})_2\text{O}(\text{BDC}))_3 \cdot 25\text{H}_2\text{O}]^{104}$, which was first discovered by Férey's group¹⁰⁵. Horcajada et al. showed that both Cr-MIL-100 and Fe-MIL-100 are possible to catalyze the Friedel-Crafts benzylation of benzene with benzyl chloride¹⁰⁶.

1.4.2 Catalytic sites incorporated in organic ligands

The organic linker can be used to introduce catalytic function. Direct modification of the linker by acid, sulfonic groups or amino groups can be used to prepare brønsted acid or base catalysts. Otherwise heteroatom substituted linker (e.g. sulfur, nitrogen) can be used as anchor for the attachment of catalytic species. This way the active species can be directly located in the void space of the pore. Hence high accessibility of active sites by reactant molecules is achieved. These catalysts should be highly active.

Hupp and co-workers prepared Zr-MOF containing porphyrine linker, which were modified by different metal ions (Al, Zn, Pd, Fe). These catalysts were active in the styrene epoxidation and were highly efficient in the oxidation of cyclohexane to cyclohexanol¹⁰⁷. Genna et al. used two ways to immobilize Rh cations on anionic metal nodes in ZJU-28 and anionic organic linker of MIL-101-SO₃. The performance of these two catalysts was tested in the hydrogenation *n*-octene. The catalyst showed high activity in the hydrogenation 2,3-dimethylbutene when the active rhodium was supported on the organic linker due to the better accessibility¹⁰⁸. The Zhou group reported a series of highly stable and highly porous porphyrinic MOFs, PCN-224(M) (M = 2H, Ni, Co, Fe), build from six-connected Zr₆ clusters linked by metal porphyrin linker M-TCPP (H₆TCPP = 5, 10, 15, 20-tetra (carboxyphenyl)) with large channels of 1.9 nm in dimension. These catalysts were

active in the cycloaddition reaction of carbon dioxide and propylene oxide¹⁰⁹. Su and co-workers have utilized Ir-H₄TCPP together with HfCl₄ to synthesis a stable Ir(III) porphyrin MOF Ir-PMOF-1(Hf), which is *iso*-structural to PCN-224(M).

1.4.3 Catalytic moieties encapsulated in the pore space

The inherent nature of MOF materials such as metal centers, ordered porous structure, uniform pore sizes, high surface areas, and functional organic linkers provide a promising strategy, with enables us to encapsulate immobilize various catalytic moieties in the pore space.

E.g. metal nanoparticles were encapsulated inside the pore space of MOFs by solid grinding, chemical vapor deposition and solution infiltration.

Fischer's group has successfully supported Ru complex into the pore space of MOF through chemical vapor deposition. The catalyst [Ru(cod)(cot)]_{3.5}@MOF-5 exhibited a high efficiency in the hydrogenation from benzene to cyclohexane¹¹⁰. Xu's group immobilized Au particles in the cages of ZIF-8 by solid grinding organic gold complex Me₂Au (1,5-cyclooctadiene) with as-synthesized ZIF-8. This Au supported ZIF-8 has shown a great performance in the CO oxidation reaction¹¹¹. Through impregnation method, Li et al. immobilized prepared Pd nanoparticles into the pore space of MIL-101(Cr), the obtained Pd@MIL-101(Cr) was proved as an efficient catalyst in the synthesis of methyl isobutyl, Suzuki-Miyaura and Ullmann coupling of aryl chlorides¹¹². By liquid impregnation-reduction method, Cheng et al. loaded silver nanoparticles in the pore space of MIL-101(Cr) yielding Ag@MIL-101(Cr). Under mild condition, Ag@MIL-101 demonstrates quite high catalytic efficiency in fixation of carbon dioxide with alkynes to propionic acids. The excellent performance attributed to the bifunctional properties of simultaneous capture and low-energy conversion of carbon dioxide. In addition, Ag@MIL-101 can realize at least 5 cycles reaction without significant loss of activity and selectivity¹¹³

1.4.4 Hydroformylation with Rh-supported heterogeneous porous catalysts

Today homogeneous catalysts are mostly used hydroformylation of olefins due to high activity¹¹⁴⁻¹²⁴. However, homogeneous catalysts are expensive and difficult to

recover and to reuse. Therefore the development of heterogeneous catalysts is of interest because they are better separable and recyclable¹²⁵⁻¹³¹.

In the recent reports, Shi et al. supported rhodium nanoparticles in the pore space of a series of boron doped g-C₃N₄. These catalysts demonstrated high catalytic efficiency in the hydroformylation of alkenes¹³². In the hydroformylation of long-chain alkenes (*n*-dodecene), Tao et al. immobilized Rh-sulfoxantphos in the mesoporous silica nanospheres in an ionic liquid IL-in-oil pickering emulsion system. The catalysts exhibit high chemoselectivity of 94% due to the increased interface and properties of ILs¹³³. In addition, a rhodium supported reduced graphene oxide was synthesized via liquid-phase reduction by Tan and co-workers. This catalyst was firstly used in hydroformylation of *n*-hexene. The results showed that the Rh/RGO catalyst with high rhodium loading exhibited high 1-hexene conversion and *n*/*i* ratio of 4.0 among the tested catalysts¹³⁴.

Only a few studies investigated the hydroformylation of rhodium-supported MOFs. Hou et al. successfully synthesized a highly porous and crystalline MOF ZIF-8 and supported Rh cation in the pore space via vigorous agitation. Rh@ZIF-8 exhibited high catalytic activity for the hydroformylation of *n*-alkenes¹⁵. Our group has previously immobilized Rh complex in the pores of MIL-101(Cr), the Rh@MIL101(Cr) was proved to have high conversion and *n*-aldehydes selectivity in the hydroformylation of *n*-alkenes¹³ (Figure 8). Simultaneously, Rh-supported IRMOF-3 were prepared and tested. Compared to other Rh-supported MOFs Rh@MOF-5 and Rh@MIL-77, a significant influence of the MOF framework on the catalytic properties was observed¹⁴. Previous work proves that rhodium loaded Zn-MOFs are potential catalysts for the hydroformylation of olefins.

In general previous work with single MOFs shows the potential of the application of Rh-supported MOFs for the replacement of homogeneous catalysts in the hydroformylation of olefins. However, mostly smaller pore size ZIF and IRMOF, were used. The influence of the pore size and porosity on the catalytic performance was not investigated. Specially, the new stable Zr-MOFs were not considered so far. Also information about leaching and catalyst re-use is missed. Therefore, in this thesis, several Rh-supported zirconia based MOFs with different structure and pore sizes ranging from 6 to 30 Å are prepared and tested in the hydroformylation of different sized small and bulky olefins including their mixtures.

1.5 Structure and porosity of investigated Zr-MOFs

1.5.1 Metal-organic framework UiO-66 and UiO-67

In 2008, Cavka et al. synthesized new Zr-MOFs with same metal nodes but different length of organic linkers, namely UiO-66 and UiO-67¹³⁵. In this work, a new inorganic metal node, 12-coordinated, $Zr_6O_4(OH)_4(CO_2)_{12}$ was used and further connected via the linear organic linkers forming a cubic close packed 3-dimensional framework (Figure 8).

In the case of UiO-66, the primary building units are connected via the ligands 1,4-benzenedicarboxylic acid (H_2BDC) to form a tetrahedral secondary building unit (SBU). The pore openings are formed by a triangle ring of the secondary building units. The octahedral cage was surrounded by tetrahedral cages. The framework is formed by porous tetrahedral and octahedral cages with internal pore diameters of 6 Å. Compared to UiO-66, the MOF UiO-67 has the same topology (fcu-MOFs). With the exchange of the terephthalic acid linker by the longer 4,4'-biphenyl dicarboxylic acid (H_2BPDC), the pore size of UiO-67 increased to 8 Å. Both show high chemical and thermal stability although the pore opening are rather large.

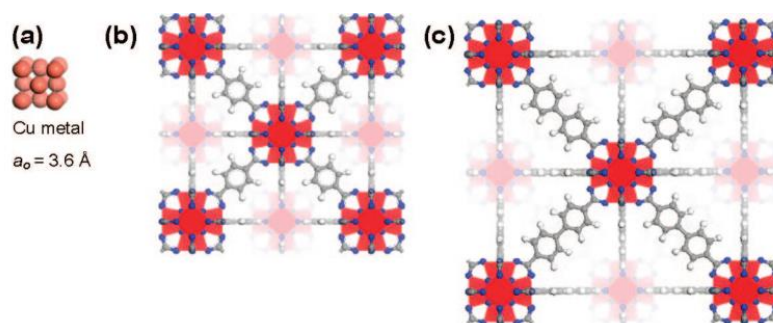


Figure 8. (a) One unit cell of copper drawn to scale with: (b) Zr-MOF with 1,4-benzene -dicarboxylate (BDC) as linker, UiO-66, (c) Zr-MOF with 4,4'-biphenyl-dicarboxylate (BPDC) as linker, UiO-67. Zirconium, oxygen, carbon, and hydrogen atoms are red, blue, gray, and white, respectively.

The inorganic metal node is the key factor to stabilize the framework. It consists of an inner $Zr_6O_4(OH)_4$ core which the triangular faces of the Zr_6 -octahedron are alternatively capped by μ_3 -O and μ_3 -OH groups. The edge of polyhedron is linked by carboxylate ($-CO_2$) group with originating from the dicarboxylic acids. Thus a $Zr_6O_4(OH)_4(CO_2)_{12}$ cluster was formed (Figure 9). Each zirconium atom is eight-coordinated forming a square-anti prismatic coordination consisting of eight oxygen atoms. One square face is formed by oxygen atoms originating from carboxylates while the second square face is formed by oxygen atoms coming from the μ_3 -O and μ_3 -OH groups. This results in a cluster shaped like a Maltese star.

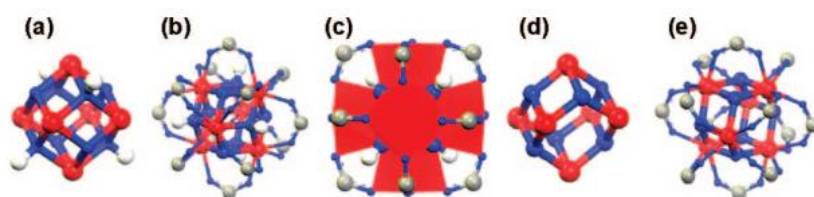


Figure 9. Structures (a) and (d) show the inner core Zr_6 -cluster drawn alone for clarity, in hydroxylated and dehydroxylated form, and the symmetry change from T_d (-43 m) to D_{3d} (-3 m) when the two μ_3 -OH groups are removed. Structures (b) and (e) show the full cluster to illustrate the change in zirconium coordination from 8 to 7 upon dehydration. Zirconium, oxygen, carbon and hydrogen atoms are red, blue, gray, and white, respectively.

The specific surface area of UiO-66 was $1187 \text{ m}^2/\text{g}$ which agrees with the predicted value. Higher surface area materials were obtained by increasing the length of the linkers. In case of UiO-67 was used the longer biphenyl dicarboxylic linker which led to an increase of the specific surface area to *ca.* $3000 \text{ m}^2/\text{g}$, respectively. Increasing the length of the linker does not reduce the stability of these structures; very stable materials with surface areas in the range of the highest reported can therefore be reached. Accessibility to the internal surface of the framework is confined by triangular pore windows.

1.5.2 Metal-organic framework MOF-808

The MOF-808, formula $Zr_6O_4(OH)_4(BTC)_2(HCOO)_6$, was synthesized by Yaghi et al.¹³⁶ using a tripodal benzene-1,3,5-tricarboxylic acid (H_3BTC) as the organic ligand. The crystal structure analysis showed that the inorganic bricks are connected

to six BTC ligands and each ligand coordinated to three inorganic bricks. In addition, another six formate ligands, which account for the charge balance, coordinated also with the inorganic bricks. These formate anions are found coordinated to the Zr atoms and disordered as both mono- and bidentate ligands. Via 6,3-connected MOF-808 has a three-dimensional framework with an overall spn topology (Figure 10). Tetrahedral were formed through the connection between inorganic bricks and BTC linkers and internal pore diameters of 4.8 Å were obtained, with the inorganic bricks at the vertices and the BTC linkers at the faces of the tetrahedron. The tetrahedral cages are sharing vertices in such a way that the overall connectivity of MOF-808 can be simplified to an augmented diamond net. The large adamantane units contains extra-large pores of 18.4Å diameter is formed by the surrounding tetrahedral cages.

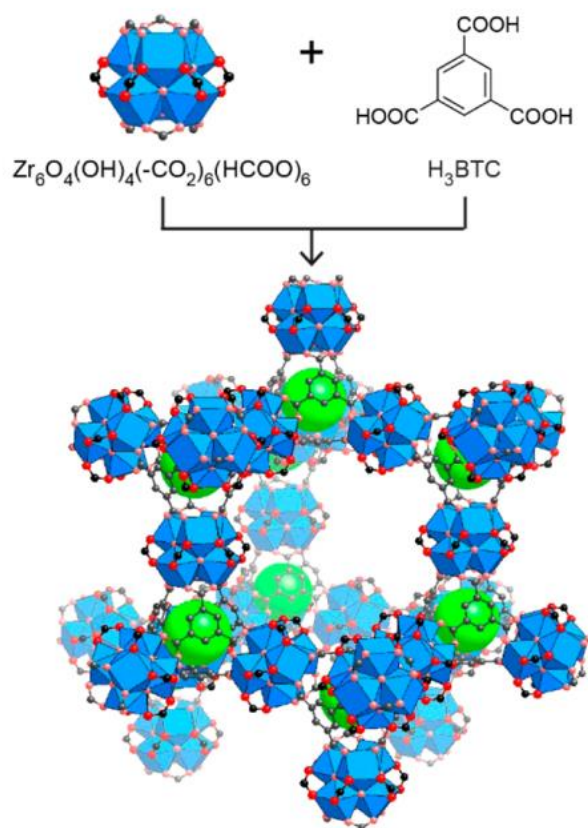


Figure 10. $\text{Zr}_6\text{O}_4(\text{OH})_4(-\text{CO}_2)_6(\text{HCOO})_6$ secondary building units (SBUs) are combined with BTC linkers to form MOF-808, which has a porous, three-dimensional framework containing large adamantane shaped cages (open) and small tetrahedral cages (filled with green spheres).

MOF-808 has high BET surface area of *ca.* 2060 m²/g. The structure was stable up to *ca.* 350 °C. In addition, the pore distribution was calculated by density functional theory (DFT), which showed that two types of micropores with diameters of *ca.* 10 and 18 Å. The result was almost identical with that obtained from crystallographic data, where a diameter of approximately 9.7 Å was found for the large hexagonal windows and 18.4 Å for the adamantane-shaped cages, respectively.

1.5.3 Metal-organic framework DUT-67

A new zirconia based secondary building unit (SBU) was discovered, which can be derived from $Zr_6O_4(OH)_4^{12+}$ by decreasing the connectivity from 12 to 8. It was used by Kaskel¹³⁷ to prepare MOF DUT-67 using a bent dithienothiophene based ligand. DUT-67 consists of a uninodal 8-connected framework with the *reo* topology. Through further extension of the modulator, MOF polymorphs with different pore systems were obtained. Thus a series of novel Zirconia based topologically different materials including DUT-67 was synthesized via bent 2,5-thiophenedicarboxylate (tdc^{2-}) ligand, which were obtained by applying a modulated synthesis approach (Figure 11).

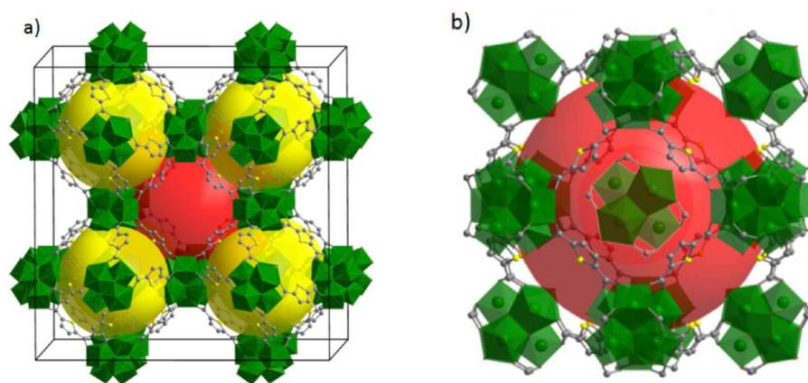


Figure 11. (a) Packing diagram with pores location (red sphere, cuboctahedral pore; yellow spheres, octahedral pores) and (b) $Zr_6O_6(OH)_2(CH_3COO)_{10}$ cluster inside the cuboctahedral pore (disorder neglected).

The synthesis of DUT-67 ($[Zr_6O_6(OH)_2(tdc)_4]$) was realized with zirconium chloride in the mixture of N,N-dimethylformamide (DMF) and N-methyl-2-pyrrolidone (NMP) choosing acetic acid as modulator. Single crystal X-ray diffraction confirmed that DUT-67 crystallized in $Fm\bar{3}m$ space group with $a = 39.120(5)$ Å. The

inner pores diameters were 14.2 Å for cuboctahedral and 11.7 Å for octahedral cage in the case of DUT-67, respectively. The thermal stability of DUT-67 was tested to be 300 °C. The specific surface area, calculated to be *ca.* 1767 m² g⁻¹ for DUT-67. Nitrogen adsorption-desorption experiments were carried out at 77 K. The isotherm was of type I. The maximum nitrogen uptake was *ca.* 287 cm³ g⁻¹. The BET specific surface area was *ca.* 1064 m² g⁻¹, respectively. The specific pore volume was 0.44 cm³ g⁻¹. In addition, the chemical and thermal stability was tested. Hydrolytic stability of DUT-67 was evaluated by soaking the dry MOF powders in water. The powder diffraction pattern did not change pointing to the intact structure. The chemical stability of DUT-67 was evaluated by immersing dried powders in concentrated HCl and NaOH with the concentration 1 mol/L for 3 days. As a result, DUT-67 structure remained unchanged in the strong acidic medium.

1.5.4 Metal-organic framework NU-1000

With the continuous progress of MOF synthesis technology, in addition to the field of micropores, in recent years, many mesoporous MOFs have also been synthesized by Peoplevia improving the utilization of metals and ligands. Among the various metal-based nodes from previous reports, MOFs constructed from the strong bonding between the oxophilic Zr^{IV}₆ nodes and the carboxylates of the linkers ensures the high thermal (up to 500°C), chemical (pH 1–10), and mechanical stability of NU-1000, and the Lewis acidity of the zirconia nodes provided isolated active sites for chemical transformations. In addition, solvent-assisted ligand incorporation was realized as a new functionalization technique to incorporate carboxylate-based functionalities in the Zr-based metal-organic framework efficiently. Thus a highly robust mesoporous (containing pores >2 nm) metal-organic framework, NU-1000, was successfully synthesized on a gram scale from inexpensive starting materials¹³⁸.

The structural projection of NU-1000 can be visualized as a 2D extended Kagome network, built via eight connected Zr₆(μ₃-O)₄(μ₃OH)₄(H₂O)₄(OH)₄ nodes at each corner and tetrapodal 1,3,6,8-(p-benzoate)pyrene (H₄TBAPy) ligands located at each edge. A part of the octahedral Zr₆ cluster is capped by eight μ₃-OH ligands. Eight of the twelve octahedral edges are connected to TBAPy linkers, while the remaining Zr coordination sites are occupied by eight terminal -OH ligands. The obtained MOF had the molecular formula Zr₆(μ₃OH)₈(OH)₈(TBAPy)₂ and contained mesoporous channels formed through terminal -OH ligands. The extra-large (31 Å) mesoporous

channels extend throughout the structure. Besides, the large channels allowed also for the rapid flow of reactants throughout the entire heterogeneous framework (Figure 12).

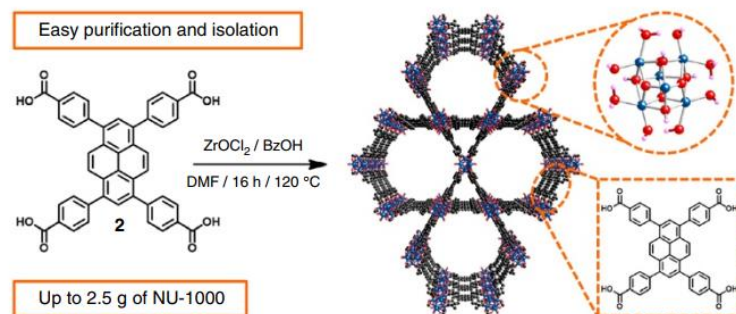


Figure 12. Synthesis of NU-1000 from TBAPy and ZrOCl_2 with benzoic acid as modulator. NU-1000 (2.5 g) can be prepared in one reaction.

Infrared spectra show a vibration band at *ca.* 3674 cm^{-1} which is assigned to terminal $-\text{OH}$ groups. The observed shoulder at *ca.* 3671 cm^{-1} was consistent with the bridging $\mu_3\text{-OH}$ groups. The latter are also observed with UiO-66. The N_2 adsorption and desorption isotherms of the parent NU-1000 were of type IV. Hence, the material contains mesopores. The BET surface area was *ca.* $2320 \text{ m}^2 \text{ g}^{-1}$.

2. Experimental part

2.1 Reagents

Table 1. The specifications of the main reagents

Reagents	Purity	Company
ZrCl ₄	98%	Acros
ZrOCl ₂	99.5%	Acros
dimethylformamide(DMF)	99.5%	Acros
1-Methyl-2-pyrrolidone (NMP)	99%	Aldrich
dioxane	99.5%	ROTH
benzene-1,4-dicarboxylic acid (BDC)	98%	MERCK
biphenyl-4,4' -dicarboxylicacid (BPDC)	98%	ABCR
benzene-1,3,5-tricarboxylic acid (BTC)	97%	Fluka
2.5-Thiophenedicarboxylic acid	99%	Aldrich
tetrakis (triphenylphosphine) palladium	99.8%	MSDS
1,3,6,8-tetrabromopyrene	97%	Aldrich
4-ethoxycarbonylphenylboronic acid	98%	Aldrich
<i>n</i> -hexene	97%	Aldrich
<i>n</i> -octene	98%	Aldrich
<i>n</i> -decene	95%	Acros
<i>n</i> -dodecene	95%	Acros
<i>n</i> -hexadecene	99%	Aldrich
3,3-dimethyl-1-butene	97%	Aldrich
2,4,4-trimethyl-1-pentene	96%	Aldrich
4-methylstyrene	96%	Aldrich
Cyclohexene	99%	Acros
Cyclooctene	99%	Acros

2.2 Synthesis of MOFs

2.2.1 Synthesis of UiO-66 and UiO-67

UiO-66, and UiO-67 were synthesized solvothermally via slightly modified from literature procedures¹³⁵. In details, the synthesis of UiO-66 was performed by dissolving ZrCl_4 (0.159g, 0.681mmol) and H_2BDC (0.102g, 0.681mmol) in DMF (25mL, 0.34mol) at room temperature. Then the mixture was sealed in an 100mL autoclave and placed in a preheated oven at 120°C for 24 hours. UiO-67 was synthesized by replacing H_2BDC with equivalent molar amounts of H_2BPDC . The crystallized MOF UiO-66 was filtered off and washed three times with 5mL of DMF and 10mL of CH_2Cl_2 . Then the resulting solid was suspended in 50ml CH_2Cl_2 for 12 hours at room temperature. The obtained solid was then filtered and washed with 3×10mL of CH_2Cl_2 . Finally, the product was dried at 70°C under vacuum yielding the as-synthesized material. UiO-67 was treated in the same way to remove the DMF from the pore system.

2.2.2 Synthesis of MOF-808

Microcrystalline MOF-808 was prepared using slightly modified published procedure^{136,139}. MOF-808 was prepared by dissolving $\text{ZrOCl}_2 \cdot 8\text{H}_2\text{O}$ (0.97g, 3mmol) and H_3BTC (1,3,5-benzenetricarboxylic acid, 0.21g, 1mmol) in the mixture of 45mL DMF (dimethyl formamide) and 45mL formic acid. The mixture was placed in an 100mL autoclave and heated to 130°C for 48 hours. The obtained white powder was collected by filtration and washed 3 times with 20mL DMF. Then as-synthesized MOF-808 was immersed in 150 mL CH_2Cl_2 for 12h. The CH_2Cl_2 -exchanged sample was finally evacuated at 70 °C for 24 h to yield activated sample.

2.2.3 Synthesis of DUT-67

DUT-67 were solvothermally synthesized using slightly modified procedure based on literature¹³⁷. In detail, synthesis of DUT-67 was performed by dissolving ZrCl_4 (230mg, 1mmol) in the mixture of 12.5mL DMF and 12.5mL Methylpyrrolidone

(NMP). Then 2,5-Thiophenedicarboxylic acid (110mg, 0.67mmol) was added in the obtained solution by sonication at room temperature. After that acetic acid (7mL, 117mmol) was added to resulting solution and sonicated for 10min. Then the mixture was sealed in autoclave and placed in a preheated oven at 120°C for 48 hours. The crystallized product of DUT-67 was separated by centrifugation and washed several times with DMF until supernatant solution became colorless. Then the resulting solid was suspended in 100ml CH₂Cl₂ for 12 hours at room temperature. The obtained solid was then filtered and washed with 3×10ml of CH₂Cl₂. Finally, the product was dried at 70°C under argon atmosphere for 2h and as-synthesized powder was obtained.

2.2.4 Synthesis of NU-1000

Mesoporous MOF NU-1000 were synthesized solvothermally via slightly modified from literature procedures^{138,140}. The synthesis procedure was performed in two steps. The first step is the synthesis of the large organic linker. The second step is the preparation of MOF framework. The preparation of the 4,4',4'',4'''-(pyrene-1,3,6,8-tetrayl) tetrabenzoic acid (H₄TBAPy) was prepared in 5g scale via a standard Suzuki-Miyaura reaction between 1,3,6,8-tetrabromopyrene and (4-(ethoxycarbonyl)phenyl) boronic acid (Figure 13). During the reaction, ethyl ester was used to slow down the hydrolysis of the benzoic ester. Tetra ester was obtained through simple filtration, which is hydrolyzed cleanly to the tetra-acid under basic conditions in dioxane.

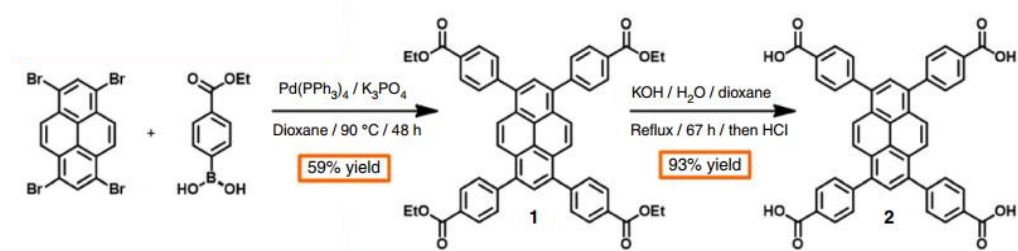


Figure 13. The two-step synthesis of the tetra acid ligand for NU-1000 can be accomplished in 3d with an overall yield of 55% to produce H₄TBAPy (2) without the need for chromatographic purification.

2.2.4.1 Synthesis of organic linker

- i) 270mL of degassed dioxane was added into a 500ml three-necked round bottom flask.
- ii) 5g of tetrabromopyrene and 8.25g of 4-ethoxycarbonylphenylboronic acid, 16.5 of potassium phosphate tribasic and 0.75g of tetrakis (triphenylphosphine) -palladium were then added into the flask through stirring in the argon atmosphere. Thus brown solution was obtained.
- iii) The solution was heated at 90°C for 72h. After heating the solution turned to black.
- iv) 200mL of water was then added to cool down the solution. The reaction product was filtered off with a Büchner funnel with a medium filter. After filtration the yellow solid was washed with 300mL water and 300mL acetone.
- v) 100mL boiling chloroform was added 5 times to dissolve the desired product in the funnel. Then 300mL of methanol were added and a light-yellow solid material was formed. After filtration the ideal product was obtained.
- vi) 4g of the obtained intermediate in the last procedure was added in 500mL degassed dioxane by stirring in a 1L three-necked round bottom flask.
- vii) 400mL 0.33mol/L KOH were added in the flask and stirred for 18h. A clear solution was observed after the reaction.
- viii) HCl was added in the solution slowly and PH was kept at 1. When a yellow solid was seen in the solution, stir the mixture for an additional 1h.
- ix) The solid was filtrated and dissolved in 150mL boiling DMF and then added 400mL CH₂Cl₂.
- x) The obtained yellow desired product was finally filtrated and washed with CH₂Cl₂, water and then dried in the vacuum condition at 120°C for 24h.

2.2.4.2 Synthesis of the MOF

Synthesis of mesoporous NU-1000 was realized by dissolving 1.94g of $ZrOCl_2$ and 54g benzoic acid in 120mL of DMF. Simultaneously, 800mg H_4TBAPy was dissolved in 40mL of DMF. The two solutions were placed in a 100°C oven for 1h and then mixed. Finally the mixture was placed in a 120°C oven for 16h. The obtained yellow powder was immersed in 260mL fresh DMF for 2h and then 200mL acetone for 12h. The desired product was washed 3 times with 20mL acetone and dried in vacuum condition at 70°C for one night.

2.3 Preparation of rhodium supported Zr-MOF catalysts

Rhodium supported MOF catalysts were prepared in the same way and low concentration. Typically, the rhodium loading procedure of UiO-66 sample was carried out in argon atmosphere. 10mg of (acetylacetonato)(1,5-cyclooctadiene)rhodium(I)containing *ca.* 33wt% of rhodium were dissolved in mixture solvent of 30mL of acetonitrile and 20 mL toluene under stirring. After the pale yellow solution was obtained, 2g as-synthesized UiO-66 was added under stirring. The suspension was then heated to 80°C slowly to evaporate the solvents gradually and to adsorb rhodium complex on the UiO-66 support. The obtained material was dry for the whole night and then washed 3 times with 5 ml toluene and finally dried at 70°C under vacuum. The resulting Rh@UiO-66 catalyst was stored and used for catalytic testing.

All the other catalysts namely Rh@UiO-67, Rh@MOF-808, Rh@DUT-67 and Rh@NU-1000 were prepared in the same way.

2.4 Characterization of materials

The as-synthesized and corresponding rhodium supported MOF catalysts were characterized by XRD, FTIR for investigation of structure, SEM, TEM and nitrogen sorption measurements for textural studies. Besides, XPS was utilized to study the electronic state of rhodium in Rh@MOFs.

Specifically, the parameters of all the characterization of MOFs and corresponding Rh-supported MOFs are as follows:

X-ray Diffraction (XRD) measurements were carried out on a STADI-P (STOE) X-ray diffractometer with monochromatic $CuK\alpha$ radiation($k = 1.5418 \text{ \AA}$). The sample

was prepared onto a silicon wafer and the measurement was carried out from 2 to 40 degree. Simulated patterns were calculated by Material Studio 7.0 basic on the CIF files from the Internet database.

SEM images were obtained on the DSM 960A electron microscope operating at 10.0 kV (Carl Zeiss, Oberkochen) using a resolution of 4 nm. The samples were immersed in the mixture of ethanol and water and then placed in ultrasonic bath to disperse the solid materials. After sonication one drop of the suspension was deposited on the sample plate. The suspension was dried and coated with a very thin layer of gold by using a plasma distribution method. In the next step, the plate which hold the sample was placed into the sample box. Before testing, the box was evacuated and the base vacuum of the chamber was *ca.* 2×10^{-5} kPa. The scanning images of high magnification (30000 times) were recorded with a speed of 200 $\mu\text{m}/\text{pixel}$ in accordance with the scanning time of *ca.* 3 min.

TEM measurements were carried out with a LIBRA 120 electron microscope (Carl Zeiss, Oberkochen) at 120 kV using a resolution of 0.35 nm. Images were recorded with a digital camera with 2000×2000 pixels. Before testing, the samples were also treated and well dispersed in the ethanol/water and then deposited on the copper grids. Infrared spectroscopic (IR) measurements were performed on a Nicolet 380 FTIR spectrometer coupled with smart orbit ATR (Attenuated Total Reflection) device with a resolution of 4 cm^{-1} . The IR spectra was given in the mid infra-red range from $400\text{-}4000 \text{ cm}^{-1}$.

XPS measurements were done at an ESCALAB220iXL spectrometer (Thermo Fisher) with monochromatic $\text{Al}_{K\alpha}$ radiation ($E=1486.6 \text{ eV}$). The samples were fixed on a stainless-steel sample holder with double-sided adhesive carbon tape. The electron binding energies were obtained with charge compensation using a flood electron source and referenced to the C1s core level of adventitious carbon at 284.8 eV (C-C and C-H bonds). For determination of the binding energy and peak area the peak were fitted with Gaussian–Lorentzian curves. The base pressure of the UHV chamber was below 1×10^{-7} Pa.

Nitrogen adsorption measurements were performed on an ASAP 2010 sorption system. Before measurements, the samples were dried by heating and pumping at 150°C under reduced pressure. Nitrogen adsorption measurements were carried out at the temperature of liquid nitrogen (-196°C).

Thermogravimetric analysis (TGA) was carried out in flowing argon atmosphere (15mL/min) using a Rheometric Scientific STA 1500 instrument. The approximate sample weight was 10-20 mg in all experiments and the heating rate in TG experiment was 10 °C/min.

2.5 Catalytic testing

The rhodium supported MOFs mentioned above were investigated under similar condition in the hydroformylation of linear and bulky olefins with different structure. In order to study the influence of the structure on the catalytic performance, details of reaction with a couple of olefins with gradually varied chain length were utilized. Thus linear *n*-alkenes from 6 to 16 carbon atoms such as *n*-hexene, *n*-octene, *n*-decene, *n*-dodecene and even the very long chain alkene *n*-hexadecene, the branched olefins and the bulky or less reactive olefins including 2,4,4-trimethylpentene, 3,3-dimethyl-1-butene, 4-methylstyrene, cyclohexene and cyclooctene were investigated in hydroformylation. Besides, part of the rhodium supported catalysts including Rh@UiO-66 and UiO-67 were used in the hydroformylation with mixture of linear olefins to study the possibility of single file diffusion.

2.5.1 Catalytic testing with single olefins

All the hydroformylation experiments were carried out in a 100 mL PARR reactor (Figure 14) at T=100°C, p=50 bar (CO/H₂=1), and the substrate to catalyst molar ratio based on rhodium was calculated to be *ca.*65000 under stirring at 1000rpm. Toluene was used as proper solvent.

Typically, for the reaction of *n*-hexene 95 mg of Rh@UiO-66 were added in the mixture of *n*-hexene (12.5ml) and toluene (30ml). The molar ratio of olefin based on rhodium was 65,000/1. After that the reactor was evacuated and purged with argon in order to remove air and residual moisture and then loaded with synthesis gas (CO/H₂=1) immediately up to a pressure of 50 bar at room temperature. Finally, the reaction mixture was heated under stirring at *ca.* 1000 rpm with a connection of mechanic stirrer and maintained at a temperature of 100°C. The reactions of the other olefins were carried out in the similar way using same ratio of olefin based on rhodium.

2.5.2 Catalytic testing with mixture of olefins

The hydroformylation with a mixture of olefins were carried out in a 100 mL PARR reactor at $T=100^{\circ}\text{C}$, $p=50$ bar ($\text{CO}/\text{H}_2=1$), and the substrate to catalyst molar ratio based on rhodium was kept constant compared to the condition of the reaction with mixed olefins. Toluene was used as proper solvent. Typically, 95 mg of Rh@UiO-66 were added in the mixture of *n*-hexene (4.2mL), *n*-decene (6.3mL), *n*-hexadecene (9.5mL) and toluene (30ml). The molar ratio of olefins based on rhodium was kept at 65,000/1 in the reaction with Rh@UiO-67, Rh@MOF-808, Rh@NU-1000 and 27000/1 with Rh@DUT-67. The reactor was then evacuated and purged with argon to remove air and residual moisture and then loaded with synthesis gas ($\text{CO}/\text{H}_2=1$) up to a pressure of 50 bar. Finally, the reaction mixture was heated under stirring at *ca.* 1000 rpm with a connection of mechanic stirrer and maintained at a temperature of 100°C .

2.5.3 Analysis of catalytic products

Quantitative analysis of reaction products were carried out via gas chromatography (GC), the instrument was equipped with Agilent HP-6890 equipped with a HP-5 column, $30\text{ m} \times 0.25\text{ mm} \times 0.25\text{ }\mu\text{m}$, and a flame ionization detector (FID). Specifically, in the hydroformylation of *n*-hexene, the signal position of the main products at the beginning and the end of the catalytic reaction were shown in Figure 15. The content of the product is calculated by comparing its peak area.

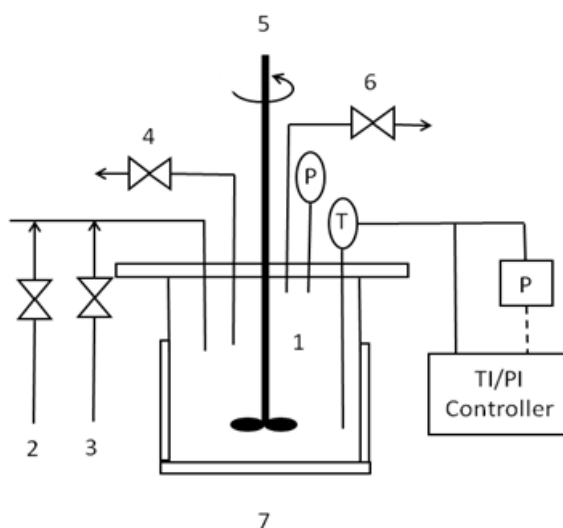
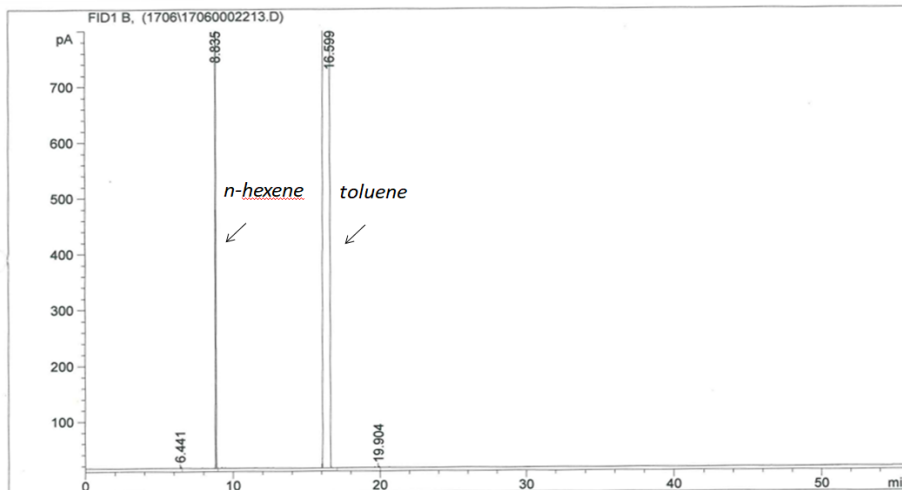
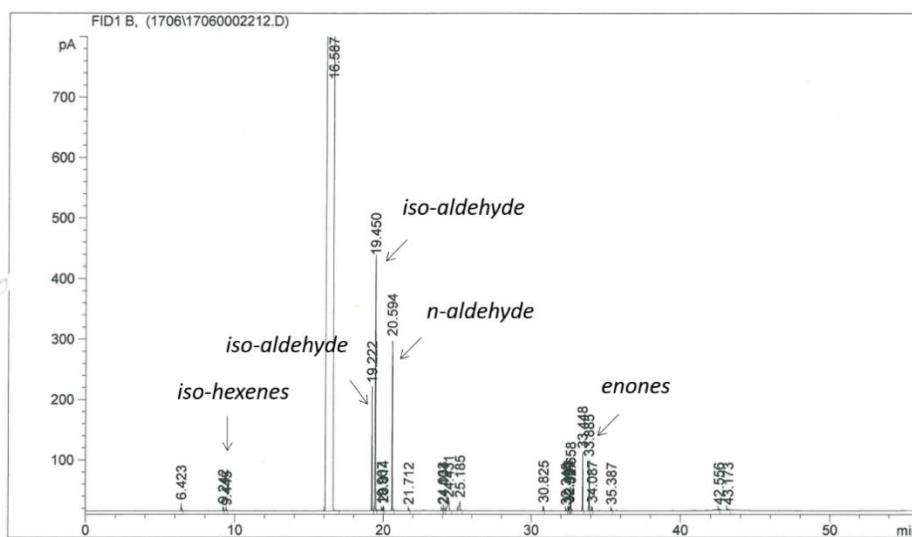


Figure 14. High pressure PARR reactor used for hydroformylation of olefins.

(1) high pressure PARR reactor; (2) Argon/Nitrogen tube; (3) Synthesis gas tube (CO/H₂=1); (4) Sampling system; (5) Gas introduction stirrer; (6) Venting; (7) Plate for heater; (P) Pressure gauge; (TI/PI Controller) Temperature & Pressure indicators in control panel.



(a)



(b)

Figure 15. Signals of main products in the hydroformylation of *n*-hexene at (a) 0h and (b) 21h.

3. Results and discussion

3.1 Hydroformylation of olefins over Rh-supported Zr-MOF UiO-66, UiO-67, and MOF-808

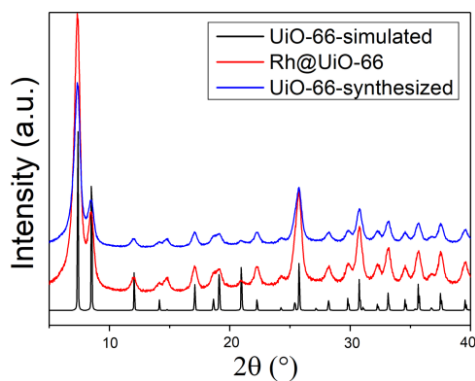
In this work we intend to investigate the relation between the pore and cage sizes as well as between the pore structure and the catalytic activity and selectivity of Rh-supported large pore Zr-MOF catalysts. For this purpose, rhodium-supported zirconium-based MOFs UiO-66, UiO-67, and MOF-808 were prepared and characterized by PXRD, FTIR, SEM/TEM, XPS, and nitrogen adsorption. The catalytic performance was studied in the hydroformylation of olefins to the corresponding aldehydes using linear olefins with different chain lengths (C6, C8, C10, C12, and C16) as model substances.

3.1.1 Characterization

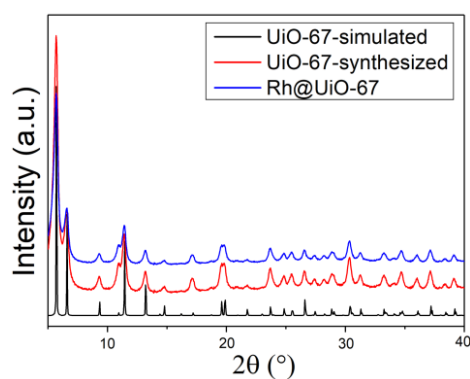
Powder X-ray diffraction patterns of synthesized MOFs after work up by washing and solvent removal are shown in Figure 16. The PXRD patterns of the synthesized UiO-66, UiO-67 and MOF-808 correspond to the expected structure type^{139,141}. The positions of observed XRD reflections are similar to the simulated patterns. The materials are crystalline and show narrow reflections especially for reflections located at $2\theta = 5-10^\circ$. The crystallite sizes obtained by the Scherrer formula are 32, 27, and 30nm, respectively¹⁴². Only MOF-808 shows a higher background. The structure of the MOFs is maintained after Rh loading. However, the intensity of the reflections is decreased due to the stress caused by the additional mechanical and thermal treatment during the Rh loading procedure. Rhodium metal reflections are not observed for Rh@UiO-66, Rh@UiO-67, and Rh@MOF-808. The very low concentrated (<0.05 ma.-%) supported rhodium is highly dispersed in the pores in a single site manner.

The FTIR spectra of the synthesized MOFs and rhodium supported MOFs are shown in Figure 17. All the prepared materials show the typical vibrational spectra of the linker molecules, 1,4-benzenedicarboxylic acid, biphenyl 1-4,4'-dicarboxylic acid, and benzene-1,3,5-tricarboxylic acid. The vibrational bands are narrow and well-resolved. The absorption bands appearing between 1300-1700 cm^{-1} are assigned to the vibrations of the carboxyl groups. The CO–O and C–O stretching vibrations appear between *ca.* 1250 cm^{-1} and 1040 cm^{-1} . The vibrational bands

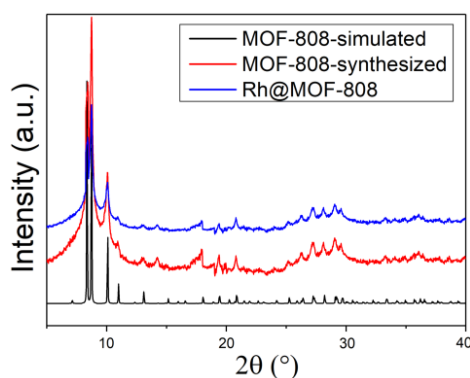
below 1000 cm^{-1} belong to $=\text{C}-\text{H}$ deformation bands of the aromatic benzene ring. The rhodium loading causes an increase in the intensities of the vibrational bands and small shifts (within 10 cm^{-1}) of the absorption maxima to higher wavenumbers, indirectly confirming the Rh loading¹⁴.



(a)

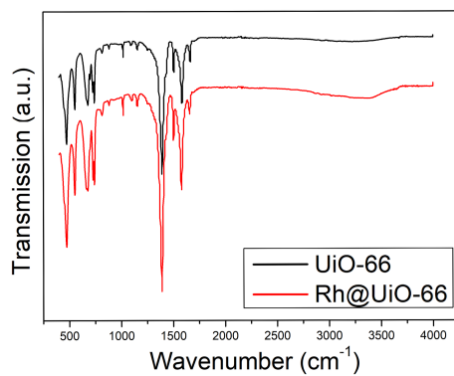


(b)

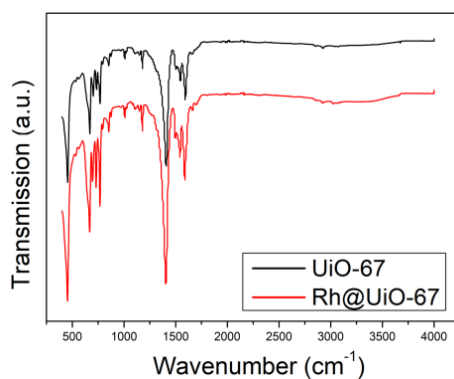


(c)

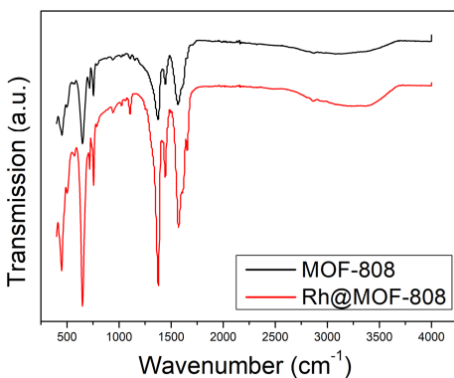
Figure 16. Simulated XRD pattern (bottom) and PXRD patterns of synthesized (top) and Rh-supported (middle) MOFs (a) UiO-66, (b) UiO-67 and (c) MOF-808.



(a)



(b)



(c)

Figure 17. FTIR spectra of as-synthesized and Rh-supported (a) UiO-66, (b) UiO-67, and (c) MOF-808.

The high resolution scanning and transmission electron microscopic (SEM and TEM) images of the three rhodium-supported MOF catalysts are shown in Figure 18. The SEM images show that the three MOFs UiO-66, UiO-67, and MOF-808 are crystallized as micrometer sized particles (in 500 times magnification, top). As

seen at higher magnification these large particles, which are regular cube-like shaped with MOF-808, are composed of sub-micrometer sized intergrown secondary particles. Large textural nanopores (Figure 18, mid, 50k magnification) exist between these secondary particles. The secondary particles are not bulky but consist of loosely agglomerated round shaped primary nanoparticles as shown by TEM (Figure 18, bottom). The agglomerated nanoparticles form an interstitial mesopore system, whereas the nanoparticles contain the micropores. The nanoparticles are of 20-30 nm with UiO-66 and UiO-67, and of 10-20 nm size with MOF-808. The peak widths of XRD reflections match the nanoparticle sizes observed in TEM images very well. Obviously, the micropores are in the nanoparticle. Even with detailed inspection by high-resolution TEM it was impossible to detect any Rh particles. Obviously the rhodium is highly dispersed and form single-site like active sites. Hence, these materials can be referred to as hierarchically composed primary nanoparticles containing secondary sub-micrometer sized particles. With respect to the pore system, these materials contain a hierarchical micro-meso-macro pore system, which is highly accessible and facilitates the mass transfer.

The X-ray photoelectron spectroscopy was used to characterize the electronic state of the elements C, O, Zr and Rh in the MOF structure. The results are shown in Figure. 19. Attempts to identify the Rh signal in the XP spectra of Rh@UiO-66, Rh@UiO-67 and Rh@MOF-808 failed due to the low concentration. However, significant changes of peak positions could be observed in the XP spectra comparing the as-synthesized UiO-66, UiO-67 and MOF-808 and the Rh-supported catalysts (Table 2). The most intense changes after Rh loading are observed in the O1s signal of UiO-66 which shifted from 530.4 to 528.4 and the Zr3p signal of UiO-67 from 332.2/346.1 to 333.5/346.8eV. Although MOF-808 cannot stay in the X-ray beam for too long time due to its weak stability, a rather short measurement showed a small shift of the Zr3p signals: 333.1/346.7 to 333.4/347.0eV. Since all other regions (Zr3d and Zr3p in the case of UiO-66, O1s in the case of UiO-67) only show minor changes in their binding energies the observed changes indicate a transfer of electron density from Rh to O (Rh@UiO-66) or from Zr to Rh (Rh@UiO-67). This indirectly suggests that the Rh species are located nearby the zirconium and/or oxygen atoms in the MOF framework. In the case of Rh@MOF-808 the binding energy of Zr is rather unaffected by the Rh doping, thus probably indicating that the Rh atoms are not so

close to the Zr. Following this interpretation, the triangle linker partially might block the access of the molecules to the side pockets.

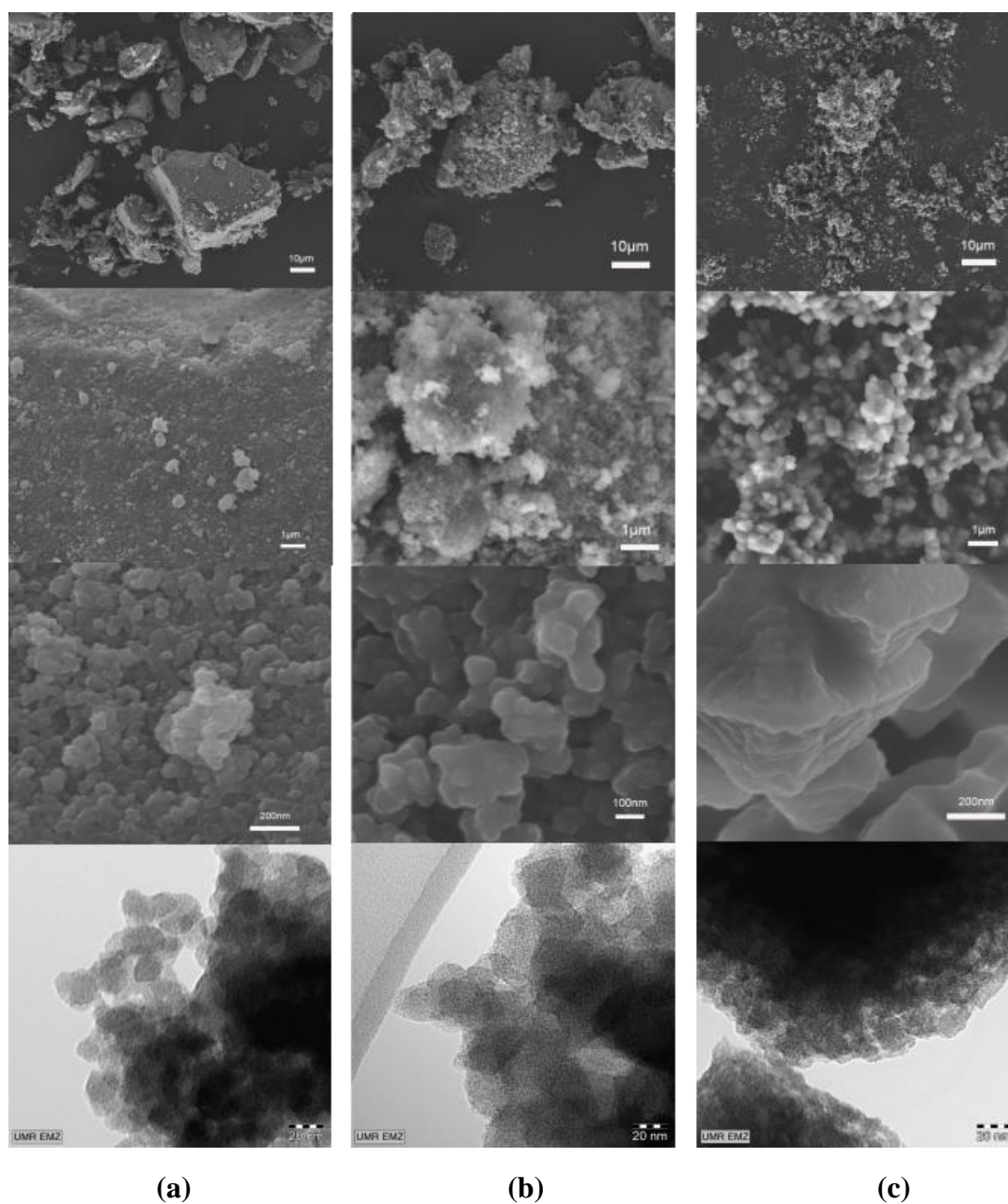
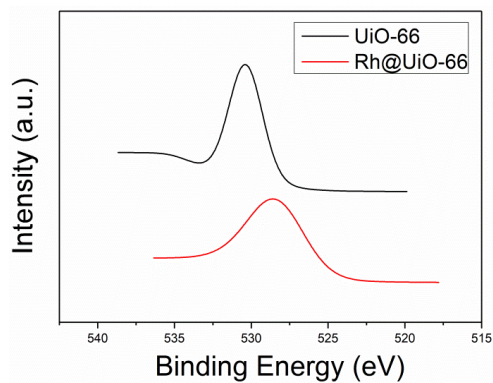
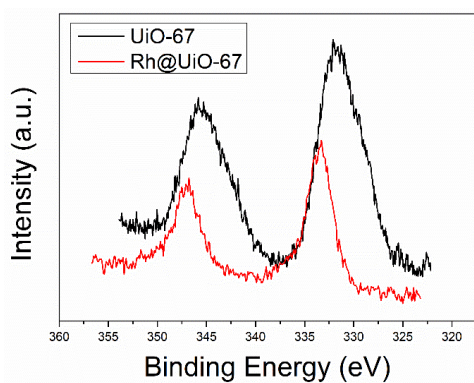


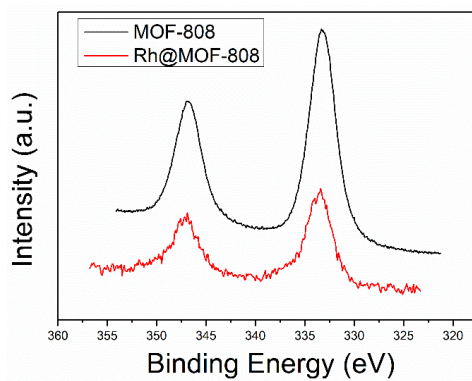
Figure 18. SEM images at 500, 5k and 50k magnification (top) and TEM images (bottom) of Rh-supported Zr-MOF (a) Rh@UiO-66, (b) Rh@UiO-67 and (c) Rh@MOF-808.



(a)



(b)



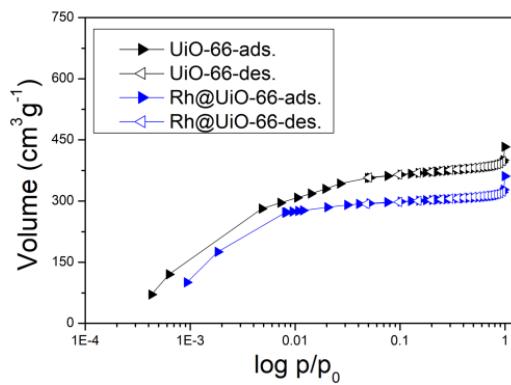
(c)

Figure 19. XPS spectra of (a) O1s signal of as-synthesized and Rh-supported UiO-66, (b) Zr3p signal of as-synthesized and Rh-supported UiO-67 and (c) Zr3p signal of as-synthesized and Rh-supported MOF-808.

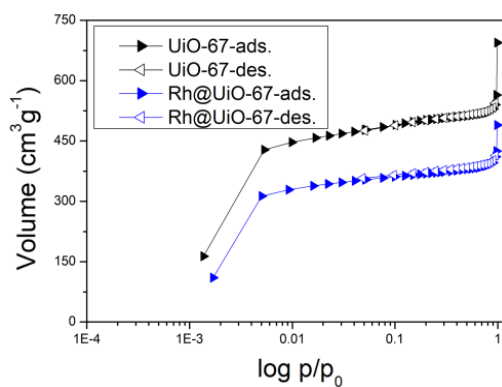
Table 2. Binding energies of carbon, oxygen and zirconium in the XP spectra of the as-synthesized and Rh-supported UiO-66, UiO-67 and MOF-808.

Element	Binding energy (eV)					
	UiO-66	Rh@UiO-66	UiO-67	Rh@UiO-67	MOF-808	Rh@MOF-808
C1s	284.8	284.8	284.8	284.8	284.8	284.8
	288.6	288.8	288.8	288.8	288.8	288.7
O1s	530.4	528.4	528.5	530.0	530.1	530.0
	532.7	529.6	531.0	532.1	531.9	531.8
Zr3d _{5/2}	182.2	182.4	181.2	183.1	182.4	182.3
Zr3d _{3/2}	184.5	184.7	183.5	185.4	184.8	184.7
Zr3p _{3/2}	332.5	333.1	332.2	333.5	333.1	333.4
Zr3p _{1/2}	346.4	347.0	346.1	346.8	346.7	347.0

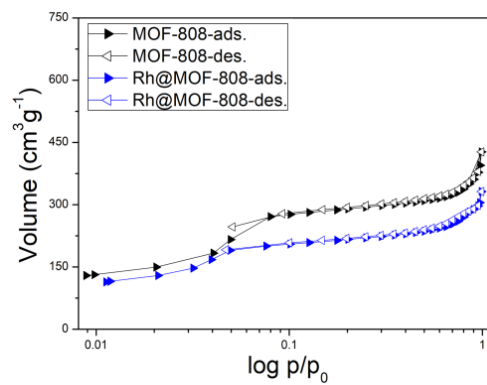
Nitrogen ad-and desorption isotherms of as-synthesized and Rh-supported Zr-MOFs are of type I (Figure 20)¹⁴³. The steep increase of the isotherms at low relative pressure (of up to $p/p_0 = 0.01$) indicates the existence of micropores. The further uptake up to a relative pressure of $p/p_0=0.8$ is due to multilayer adsorption and the filling of the mesopores. The nitrogen uptake at high relative pressure beyond $p/p_0=0.8$ is assigned to nitrogen adsorption in textural macropores. The calculated Brunauer–Emmett–Teller (BET)¹⁴⁴ theory surface areas of the porous Zr-MOFs and the corresponding Rh-supported catalysts UiO-66/Rh@UiO-66, UiO-67/ Rh@UiO-67 and MOF-808/Rh@MOF-808 are $1520.6 \text{ m}^2\text{g}^{-1}/ 1240.5 \text{ m}^2\text{g}^{-1}$, $1993.6 \text{ m}^2\text{g}^{-1}/1479.1 \text{ m}^2\text{g}^{-1}$ and $1455.1 \text{ m}^2\text{g}^{-1}/987.1 \text{ m}^2\text{g}^{-1}$, respectively. All the samples show a high specific surface area and specific micropore volume, which is in line with literature data. Both are highest with the porous MOF UiO-67 and the corresponding supported catalyst Rh@UiO-67. Besides some mesoporosity, also macroporosity is observed (Table. 3). They belong to inter-particle pores located in between the aggregated Zr-MOF nanoparticles. The observed decrease in the specific surface area and pore volume detected after Rh loading is caused by the additional mechanical stress and shrinkage due to the stirring followed by the additional heating of the samples to remove the adsorbed solvent. It cannot be excluded that some pores are blocked by the rhodium but the loading is too low to cause a significant effect.



(a)



(b)



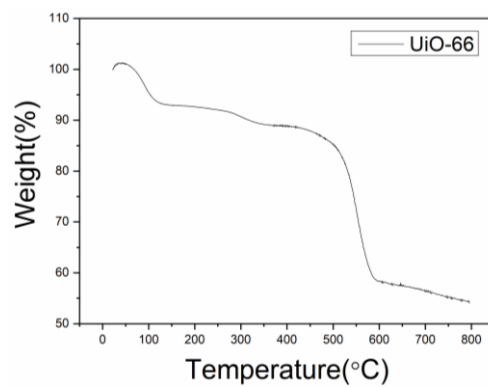
(c)

Figure 20. N₂ adsorption and desorption isotherms of (a) synthesized and Rh-supported (a) UiO-66, (b) UiO-67, and (c) MOF-808.

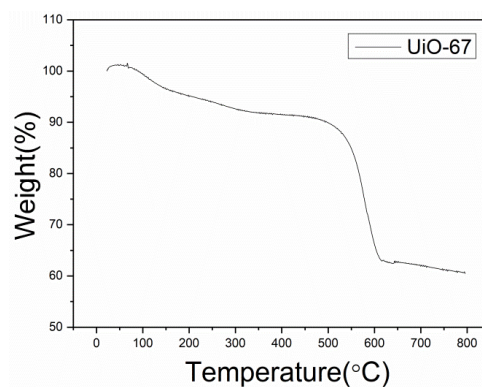
Table 3. BET surface area and pore volumes (PV) of as-synthesized and Rh-supported Zr-MOFs UiO-66, UiO-67, and MOF-808.

MOFs/	BET	Micro-PV	Meso-PV	Macro-PV
Rh@MOFs	(m ² g ⁻¹)	(cm ³ g ⁻¹)	(cm ³ g ⁻¹)	(cm ³ g ⁻¹)
UiO-66	1520.6	0.564	0.034	0.072
Rh@UiO-66	1240.5	0.462	0.024	0.072
UiO-67	1993.6	0.755	0.047	0.269
Rh@UiO-67	1479.1	0.557	0.045	0.154
MOF-808	1455.1	0.381	0.103	0.122
Rh@MOF-808	987.1	0.322	0.091	0.080

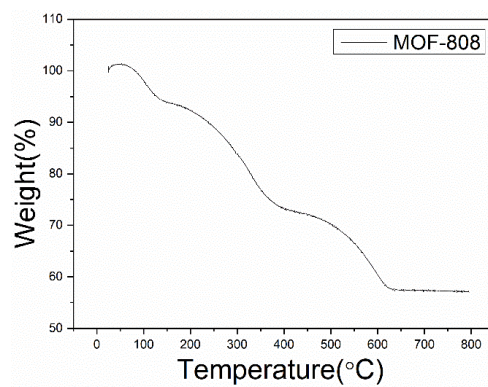
Thermal stability was tested by TGA (Thermogravimetric Analysis) and shown in Figure 21. At the beginning of the test, the slight increase in weight was due to the decrease in the density of argon at higher temperature. The curves of all the three MOFs show three steps of weight loss prior to the formation of final ZrO₂ product. In the first step in less than 100 ° C, the weight loss is assigned to the volatilization of adsorbed water. In this region, the weight loss of the materials followed the trend: UiO-67 (4.8%) < UiO-66 (6.9%) < MOF-808 (7.4%). These differences suggest that an decrease in the surface area enhances the capacity for retaining adsorbed water. The weight loss in the second step, from 100 to 400 °C, was attributed to the removal of monocarboxylate linkers, the solvent (DMF) and dehydroxylation of the zirconium cluster. Finally, in the step three, defined between 400 and 800 °C, was considered to correspond to be the thermal decomposition of the MOFs. Hence, this region was assumed to involve the complete degradation of the organic constituents of the materials resulting in the formation of zirconium oxides. Thermal stability was observed to be similar in the case of UiO-66 and UiO-67. Because the weakest point in the structure is the bond between the benzene rings and the terminal carboxyl group and not the connection between the organic linker and the inorganic brick or the metal node itself. Therefore the stability of UiO-66 and UiO-67 didn't change by shifting the organic linkers.



(a)



(b)



(c)

Figure 21. Thermogravimetric weight loss curves (TGA) of (a) UiO-66, (b) UiO-67 and (c) MOF-808 in the argon atmosphere.

3.1.2 Catalysis

3.1.3.1 Hydroformylation of linear *n*-alk-1-enes

The catalytic performance of Rh@UiO-66, Rh@UiO-67 and Rh@MOF-808 in the hydroformylation of olefins was tested with *n*-alk-1-ene molecules with different chain lengths. As expected both *n*- and *iso*-aldehydes are the desired reaction products. Beside, double bond shifted internal alkenes are formed as side-products. No notable hydrogenation of alkenes to saturated alkanes was observed during the reaction. The blank experiments with *n*-hexene and *n*-octene show that the desolvated Zr-MOFs alone do not catalyze the double bond shift of *n*-alk-1-enes to internal positions, or the hydroformylation of alkenes to aldehydes after 21h treatment. The course of conversion with the reaction time of different *n*-alkenes such as *n*-hexene, *n*-octene, *n*-decene, *n*-dodecene and *n*-hexadecene over Rh@UiO-66, Rh@UiO-67 and Rh@MOF-808 are shown in Figure 22. Typically, the conversion curves show an induction period of up to 4 h before the reaction starts markedly. The appearance of long induction periods confirm that the catalytic reaction takes place in the pores. Otherwise the reaction would start immediately. The conversions reach 80% to nearly 100% after 6 h of reaction. Even large molecules like the *n*-hexadecene are fastly converted indicating the importance of the large pores for the mass transfer.

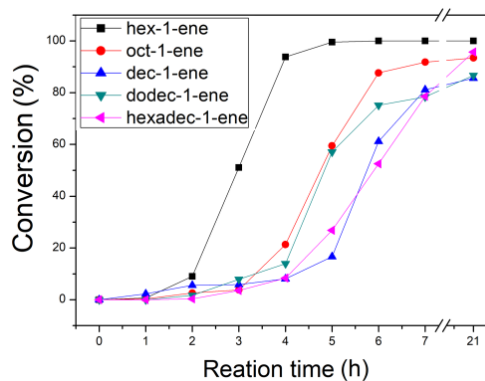
With the catalyst Rh@UiO-67, faster conversions are observed compared to Rh@UiO-66, which is in line with the larger pore size facilitating the mass transfer to and from the catalytically active sites. The conversion of all the linear olefins achieved more than 90% after 5h of reaction time. Interestingly, the conversion is highest with *n*-octene and decreases in the order *n*-octene > *n*-hexadecene \approx *n*-dodecene > *n*-decene > *n*-hexene. Surprisingly, the conversion of the short *n*-hexene proceeds slower compared to the longer *n*-alkenes. Obviously, the size of the *n*-hexene fits the pore size so that it is partially captured. Generally, the conversion becomes slower with increasing chain lengths of the *n*-alkenes because the slope of the conversion curves decreases slightly in the same order. The short induction periods and fast conversions found with catalyst Rh@UiO-67 are attributed to the larger pore size and pore opening (8–11Å) of secondary tetrahedral building units. The biphenyl ligands connecting the zirconia units of UiO-67 are markedly larger than that of terephthalic acid linker of UiO-66.

With Rh@UiO-66 the induction periods are considerably longer and the conversions proceed somewhat slower compared to Rh@UiO-67. The conversion of *n*-hexene starts after of 2 h of reaction time. Once started, the conversion of *n*-hexene increases very fast and achieves almost 100% after 5h. Compared to *n*-hexene, the conversions of other alkenes proceeds slower, decreasing with growing chain lengths of the *n*-alkene in the order: *n*-hexene >> *n*-octene > *n*-dodecene > *n*-hexadecene > *n*-decene. The induction periods are longer. The fast conversion of hexane is due to its small size which allows better passage of the small *ca.* 6 Å sized pore windows.

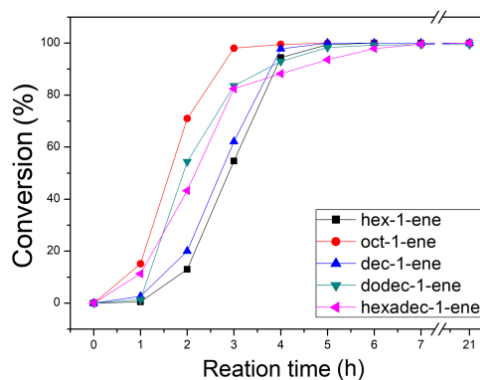
With Rh@MOF-808 the conversion of olefins reach to *ca.* 90% after 6 h. Interestingly, the large *n*-hexadecene shows high conversion compared to the shorter olefins. The conversion decreases in the order *n*-hexadecene > *n*-decene \approx *n*-dodecene > *n*-hexene > *n*-octene. Interestingly, conversion is markedly decreased compared to Rh@UiO-67 although the olefins should have easy access to the catalyst. It is concluded that the active Rh species are located in the small pore cages, not allowing access of the olefins. Additionally, the access of molecules is hindered by the linker. It is located at the faces of the tetrahedron thereby blocking the entrance. As a result, the catalytic activity is decreased. Interestingly, the conversion of *n*-hexadecene is high with all the large porous Rh@Zr-MOFs and similar to that of *n*-decene or *n*-dodecene which shows the importance of the large pores for the mass transfer of long-chain molecules.

These results show a remarkable influence of the pore size and structure on the catalytic activity. However, the impact is more complex. The conversion is increased with increasing pore size from Rh@UiO-66 to Rh@UiO-67. But surprisingly, it is decreased again with the extra-large pore (18 Å) MOF-808. This is due to the impact of the secondary building unit, where the active sites are obviously located (Figure 23). The access to active sites is hindered with Rh@MOF-808 due to the small pore size. Also the conversions of differently sized *n*-alkenes show some deviation from the expected molecule size dependency. With exception of Rh@UiO-66 catalyst, fast conversion is observed for long-chain alkenes, the conversion of hexadecane is faster than that of the small hexane. It is concluded that these findings reflect the mobility and arrangement possibilities of the different sized molecules to the catalytic Rh sites in the different structures. They influence the activity directly. So three important factors could be identified:

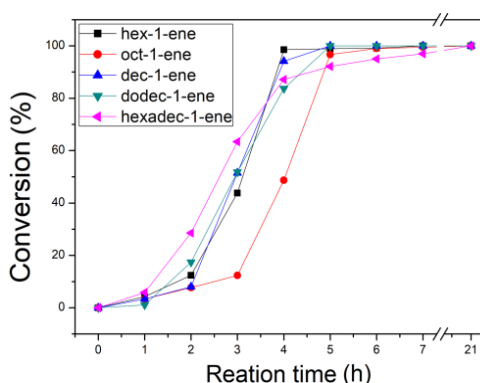
(i) the pore size for access of the catalyst, (ii) the location and accessibility of the Rh sites in the secondary building units (smaller cages or pores), and (iii) the arrangement possibilities of *n*-alkenes in the confined space of the pores (confinement effects) with respect to the active sites.



(a)



(b)



(c)

Figure 22. Conversion of the *n*-hexene, *n*-octene, *n*-decene, *n*-dodecene, and *n*-hexadecene in the hydroformylation over: (a) Rh@UiO-66, (b) Rh@UiO-67, and (c) Rh@MOF-808 in dependence on the reaction time.

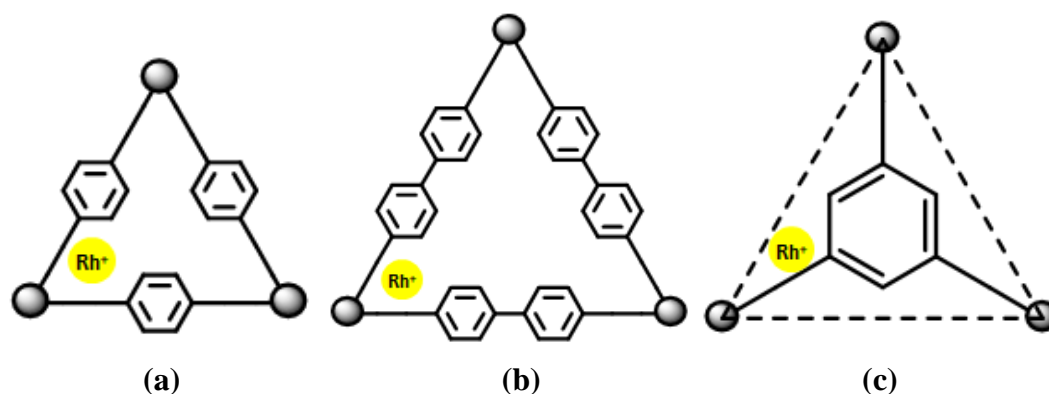


Figure 23. Schematic drawing of the pore windows of (a) Rh@UiO-66, (b) Rh@UiO-67 and (c) Rh@MOF-808.

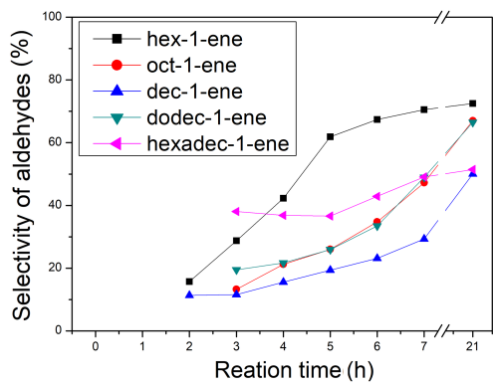
Figure 24 shows the selectivity to aldehydes observed for the hydroformylation of *n*-alk-1-enes over Rh@Zr-MOFs in dependence of the reaction time. The selectivity to aldehydes increases during the course of reaction as can be seen from the graph. First, the *n*-aldehyde is formed. With increasing formation of *i*-alkenes by the double bond shift, also formation of *i*-aldehydes starts. This is also well reflected in the decrease of the *n*/*i*-ratio during the course of reaction as discussed below. Interestingly, comparative aldehyde selectivity are observed for the very long-chain *n*-hexadecene which is obviously due to the improved access by the large pores of these MOFs. This facilitates also the formation of the transition state in hydroformylation reaction.

With Rh@UiO-66, the short chain *n*-hexene shows significantly higher selectivity to aldehydes than the longer chain alkenes. Obviously, the short *n*-hexene can easier pass the comparatively small windows of UiO-66, which are only of 6–8 Å size. In the reaction with Rh@UiO-67, highest selectivity to aldehydes is observed. The selectivity to aldehydes increases much faster than with Rh@UiO-66 and is already high at short reaction time of 1 to 4 h, which reaches *ca.* 60 to 70% after 7 h. The highest selectivity to aldehyde is observed with Rh@UiO-67 due to its larger pore window size of 8-11 Å, which provides higher accessibility of active sites.

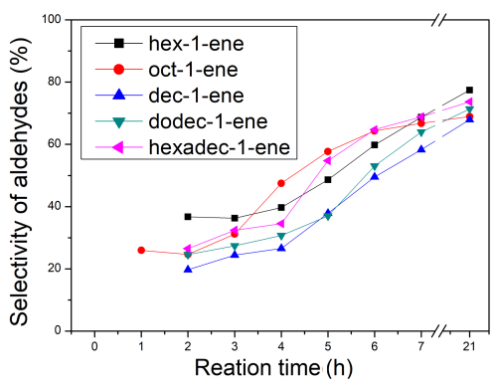
From the considered Zr-MOFs, the Rh@MOF-808 provides the largest pore size. It shows the lowest aldehyde selectivity of *ca.* 18 to 30%. The aldehyde selectivity increases slightly with prolonged reaction time. This behaviour is obviously due to lower accessibility of active sites at the secondary building units (SBU). The fixed

tripodal linker (benzene tricarboxylate) is located at the triangular faces in the windows of the secondary building units (SBU) and hinders access to Rh active sites. As a result, the formation aldehyde is diminished in Rh@MOF-808. The initial decrease of the selectivity to heptadecanal is caused by consumption of the aldehyde by aldol condensation which occurs as side reaction. In Figure 24, the yields of aldehydes for different *n*-alkenes in dependence of the reaction time obtained over the Rh-supported Zr-MOFs Rh@UiO-66, Rh@UiO-67, and Rh@MOF-808 are depicted. Highest aldehyde yields (68%-79%) are observed with catalyst Rh@UiO-67. This catalyst possesses the largest windows and cage sizes allowing easy access and mobility of the *n*-alkenes within the pore system. After starting of the reaction, aldehydes are formed continuously. Also large *n*-alkenes like *n*-hexadecene show high conversion to aldehydes compared to short chain *n*-hexene or *n*-octene.

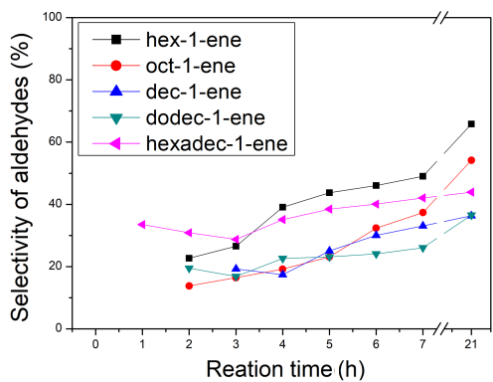
From the considered Zr-MOFs, the Rh@MOF-808 provides the largest pore size. It shows the lowest aldehyde selectivity of *ca.* 18 to 30%. The aldehyde selectivity increases slightly with prolonged reaction time. This behaviour is obviously due to lower accessibility of active sites at the secondary building units (SBU). The fixed tripodal linker (benzene tricarboxylate) is located at the triangular faces in the windows of the secondary building units (SBU) and hinders access to Rh active sites. As a result, the formation aldehyde is diminished in Rh@MOF-808. The initial decrease of the selectivity to heptadecanal is caused by consumption of the aldehyde by aldol condensation which occurs as side reaction. In Figure 25, the yields of aldehydes for different *n*-alkenes in dependence of the reaction time obtained over the Rh-supported Zr-MOFs Rh@UiO-66, Rh@UiO-67, and Rh@MOF-808 are depicted. Highest aldehyde yields (68%-79%) are observed with catalyst Rh@UiO-67. This catalyst possesses the largest windows and cage sizes allowing easy access and mobility of the *n*-alkenes within the pore system. After starting of the reaction, aldehydes are formed continuously. Also large *n*-alkenes like *n*-hexadecene show high conversion to aldehydes compared to short chain *n*-hexene or *n*-octene.



(a)

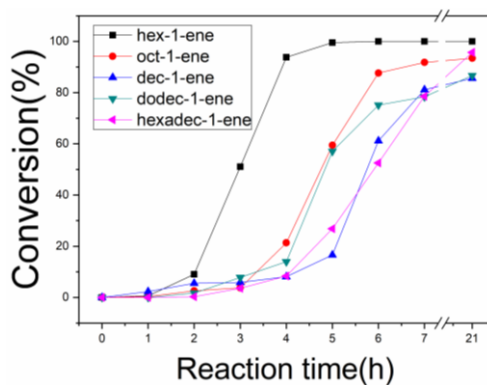


(b)

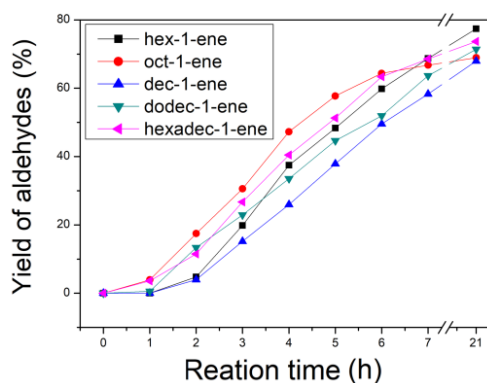


(c)

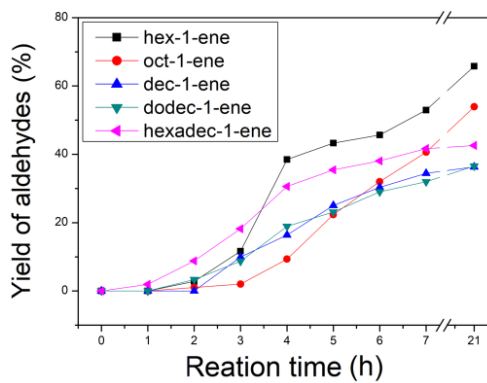
Figure 24. Selectivity to aldehydes in the hydroformylation of *n*-hexene, *n*-octene, *n*-decene, *n*-dodecene, and *n*-hexadecene over (a) Rh@UiO-66, (b) Rh@UiO-67, and (c) Rh@MOF-808 in dependence on the reaction time.



(a)



(b)



(c)

Figure 25. Yield of aldehydes in the hydroformylation of *n*-hexene, *n*-octene, *n*-decene, *n*-dodecene, and *n*-hexadecene in dependence on the reaction time over (a) Rh@UiO-66, (b) Rh@UiO-67, and (c) Rh@MOF-808.

The window and cage sizes of Rh@UiO-66 are smaller than those of UiO-67. Correspondingly, the formation of aldehydes proceeds slower and the induction

periods are longer (*ca.* 4 h) with the exception of *n*-hexene, for which similar parameters were found compared to UiO-67.

Obviously, the size of the short chain *n*-hexene fits the smaller pores of UiO-66 best and allows fast conversion. With exception of *n*-hexene, the final aldehyde yields are lower. The differences between the *n*-alkenes are larger and range from *ca.* 48 to 77 %, i.e. the influence of the chain lengths is higher with the confined pores of UiO-66. The approach of the double bond to the active sites renders more difficulties for longer chain *n*-alk-1-enes like *n*-decene and *n*-dodecene. With Rh@MOF-808, the total yields of aldehydes are the lowest (32-67%) although the structure of this MOF contains the largest pores size of *ca.* 18 Å. Different from Rh@UiO-66 or Rh@UiO-67, the course of the formation of aldehydes shows an inflection point, after that aldehyde formation proceeds markedly slower.

The analysis of the composition of the reaction mixtures after different stages of conversion shows that mixtures obtained with Rh@MOF-808 show a markedly enhanced amount of non-converted *i*-alkenes and low amounts of *i*-aldehydes compared to the reaction mixtures obtained with Rh@UiO-66 and Rh@UiO-67. This is exemplified for the case of *n*-hexene hydroformylation as shown in Figure 26. The compositions of mixtures are similar as long as the *i*-alkene content is low (*ca.* 50 % of conversion). The formation of *i*-aldehydes is diminished, finally leading to a lower total aldehyde yield. The approach of the alkenes for the formation of the transition state (insertion of *i*-alkene into the Rh complex) is most difficult with Rh@MOF-808. Obviously, active sites are located in the walls or side pockets of the large pores. At 50% of conversion the *n/i*-aldehyde ratio is *ca.* 3 for all Zr-MOFs. In the initial stage of reaction, mostly *n*-aldehydes are formed because the starting reaction mixture contains only the linear *n*-alk-1-enes. Therefore, the initial *n/i*-ratio is high at the beginning of the reaction.

The *n/i*-aldehyde ratio generally decrease during the course of reaction from *ca.* 2.5-3 to <1 after 7h. The decrease is due to the change of the composition of the reaction mixture, i.e. the formation of *i*-alkenes on the expense of the *n*-alkene. The internal olefins, formed in the double-bond-shift side-reaction remain in the reaction solution and their hydroformylation leads to the formation of *i*-aldehydes, and correspondingly, to a decrease of the *n/i*-ratio during prolonged reaction time. The *n*-olefin content decreases markedly due to the formation of *n*-aldehyde and of

i-olefins which then react to *i*-aldehydes. For example, with Rh@UiO-67 *ca.* 15% of *n*-hexene is converted to aldehydes after 3h of reaction time, whereas the *n*-hexene conversion reaches 50% already. This means *ca.* 35% of *n*-hexene is converted to *i*-hexenes. As a result, the *n/i*-aldehyde ratio decreases from *ca.* 3 to 1.6 after 4h of reaction time (Figure 27). The internal linear alkenes show a lower reactivity and the formation of the space demanding transition state during the hydroformylation reaction renders more difficulties. Therefore, the formation of aldehydes is markedly decreased with MOF-808. The access to the active Rh sites is hindered by blocking of the pore entrance of the secondary building units by the tripodal linker located in the face of the triangle window (Figure 28). Besides, the aldol condensation, as side reaction, consumes also some *n*-aldehyde after long reaction times. The amount is small in the reaction with Rh@UiO-66 and 67. It reaches *ca.* 10-12% after 21 h. However, the amount is higher with Rh@MOF-808. The large pores facilitate the formation of enones *ca.* 21% by aldol condensation of the formed aldehydes. Although the formation of *i*-aldehydes is diminished, the loss of *n*-aldehyde due to aldol condensation leads to a decrease of the *n/i*-ratio at longer reaction time. This phenomenon was in agreement with the results reported by Vu, Hou and co-workers¹³⁻¹⁵.

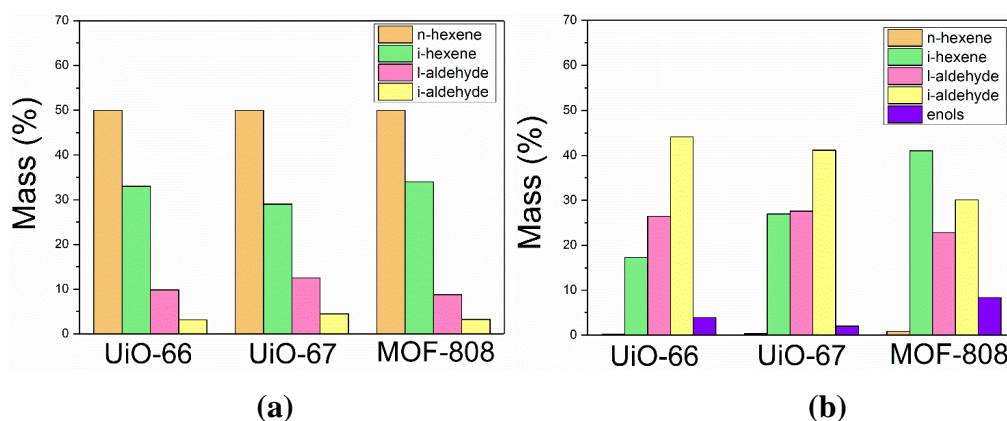
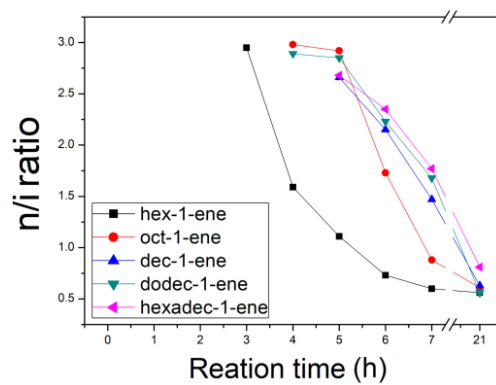
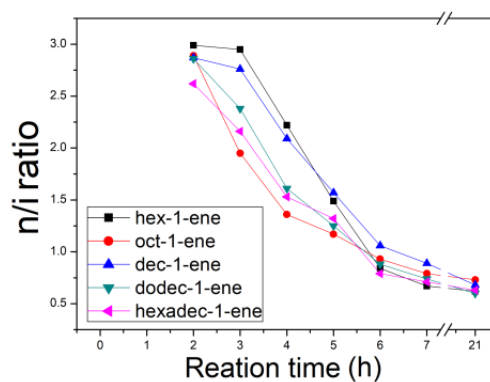


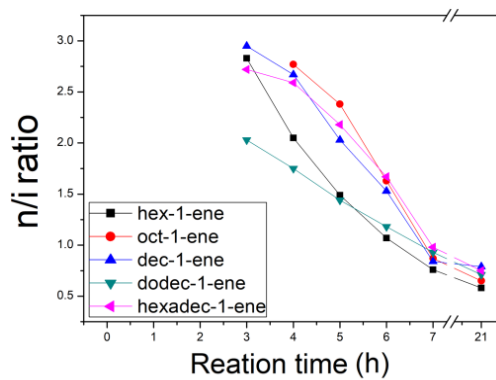
Figure 26. Composition of the reaction mixtures obtained with different Rh-supported Zr-MOF catalysts (a) 50% and (b) 100% conversion in the hydroformylation of *n*-hexene.



(a)



(b)



(c)

Figure 27. *n/i*-aldehyde ratio in the hydroformylation of *n*-alkenes of different chain lengths over (a) Rh@UiO-66, (b) Rh@UiO-67 and (c) Rh@MOF-808.

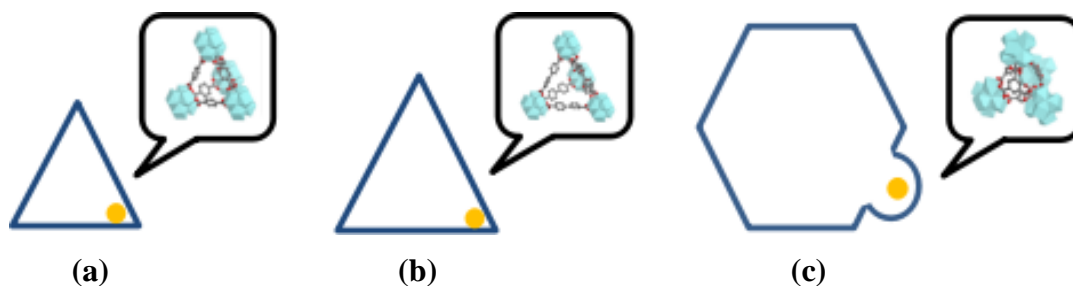


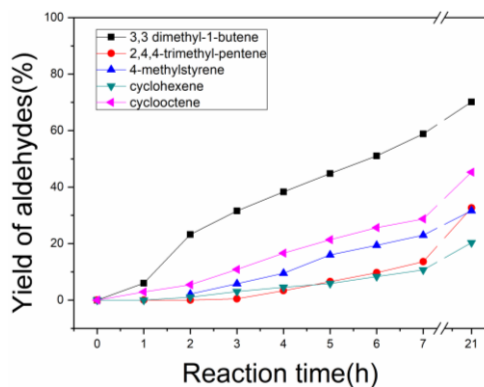
Figure 28. Pores and super tetrahedral cages of (a) UiO-66, (b) UiO-67, and (c) MOF-808. Proposed location of Rh active sites (yellow points) in the MOF pores.

3.1.3.2 Catalytic testing with bulky olefins

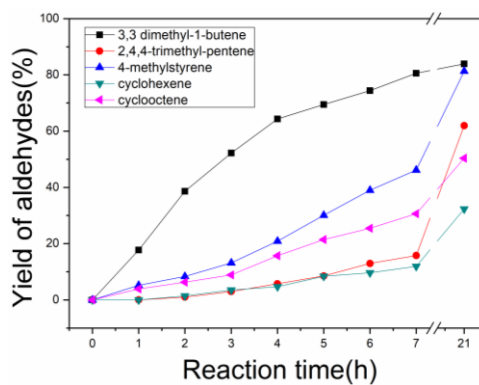
In order to compare the catalytic reaction with linear olefins, and further explore the relationship between the catalytic reaction substrate and the pore structure of the catalyst. The catalytic reaction with bulky olefins and less reactive cyclic olefins has also been studied. Compared to linear olefins, no double bond rearrangement was observed in the reaction because of the branched group. Thus hydroformylation with bulky olefins has quite high selectivity.

Figure 29 shows the yield of aldehydes in dependence of the reaction time observed with different sizes of bulky olefins. In the reaction with Rh@UiO-66, the yield of the product reacted with 3,3-dimethyl-1-butene is significantly higher than that of other olefins. After 21 hours, the yield reached to 70% while the others were arranged from 18% to 42%. As we expected, with the same reaction substrate, when the catalyst was changed to Rh@UiO-67, the yield of all reactions was improved. Although in the first 7 hours, only the yield of product from 3,3-dimethyl-1-butene has a significant increase. However, after 21h, the reaction yields were greatly improved. In the reaction with Rh@MOF-808, the yield varies significantly with time. It can be found that in the reaction with 4-methylstyrene, the reaction yield is greatly improved in the first 7 hours compared to the other two catalysts. In the reaction with the three catalysts, the yields of the reaction with cyclohexene and cyclooctene are very low, and the reaction yield with cyclohexene is always lower than that of cyclooctene, which can be explained by the two rings. The activity of the substrate is very low, and it is not easy to react, and the double bond of cyclohexene and the bond angle of the single bond make it more difficult to access the Rh active site of the catalyst. Therefore, after 21h, the conversion of cyclohexene

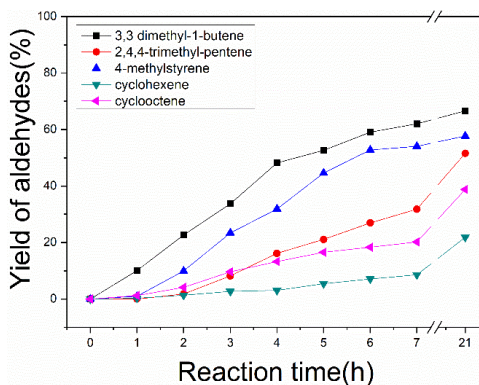
was lower than that with cyclooctene even though the molecular size of cyclohexene is smaller.



(a)



(b)



(c)

Figure 29. Yield of aldehyde in the hydroformylation of 3,3-dimethyl-1-butene, 4-methylstyrene, cyclooctene, cyclohexene, and 2,4,4-trimethylpentene over (a) Rh@UiO-66, (b) Rh@UiO-67 and (c) Rh@MOF-808 in dependence on the reaction time.

3.1.3.3 Catalytic testing with linear olefin mixtures

In order to test the possibility of single file diffusion hydroformylation of olefin mixture with Rh-supported MOFs were also investigated. In this case UiO-66 and UiO-67 were chosen as model because their structures have the same topology but different pore size. In Figure 30 is shown the different catalytic performance between single olefin and mixture olefins. Interestingly, in the hydroformylation with Rh@UiO-66, the conversion has shown a clear difference in the hydroformylation with single olefin. The reaction starts in a shorter time with *n*-hexene than that with *n*-decene and *n*-dodecene. However, when three olefins were mixed, the conversion of the reaction changed very closely with time. This phenomenon was also observed in the hydroformylation with Rh@UiO-67. Conversion with Rh@UiO-67 was observed to be highest with *n*-hexadecene at 3h and lowest with *n*-hexene. However, the figures were obviously different in the mixed olefin reaction. The conversion of mixtures containing three different olefins was almost the same for each component during the whole process of the reaction.

This phenomenon could be explained from the structure that the 180° bonding angle of the linker in the framework of UiO-66 and UiO-67 allowed rotation of the benzene ring. Thus a linker-orientation effect can be observed. As shown in Figure 31. The preferred linker orientation markedly modulated the window size of the framework and thus structure isomers by distortion of the crystal lattice could be obtained. The rotation of benzene group was dependent and isolated from each other. Therefore, under normal conditions, the benzene rings of the ligands are arranged in the lowest energy manner and lattice distortions cannot happen automatically. However, when guest molecules passed through the channel, a domino-like effect could happen. The orientation of benzene ring was modified and changed in the direction of the molecule pathway can be induced. The following changes of the lattice lead to collective changes in the lattice of the framework creating quasi one-dimensional channels of enhance directed molecule motion compared to the original two-dimensional pore system in the framework of UiO-66 and UiO-67. Effective window size shift between fully open and partly closed window derive from the orientation of the linker by rotation in the framework (Figure 31). Thus, a single-file diffusion was observed in the conversion behavior of the mixture olefins over Rh@UiO-66 and Rh@UiO-67, which shown that the conversion tend to be the

same with different size of linear olefins because the molecules cannot pass each other.

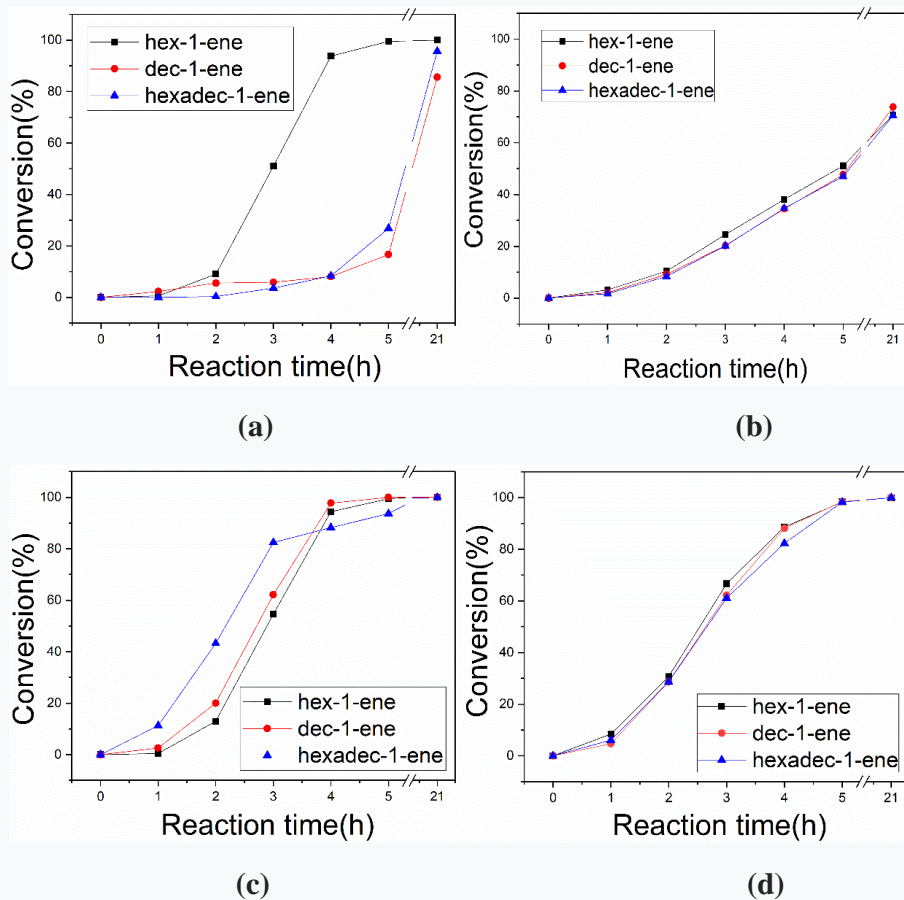


Figure 30. Hydroformylation with (a) single olefin and (b) mixture olefins of *n*-hexene, *n*-decene and *n*-hexadecene catalyzed by Rh@UiO-66. Hydroformylation with (c) single olefin and (d) mixture olefins of *n*-hexene, *n*-decene and *n*-hexadecene catalyzed by Rh@UiO-67.

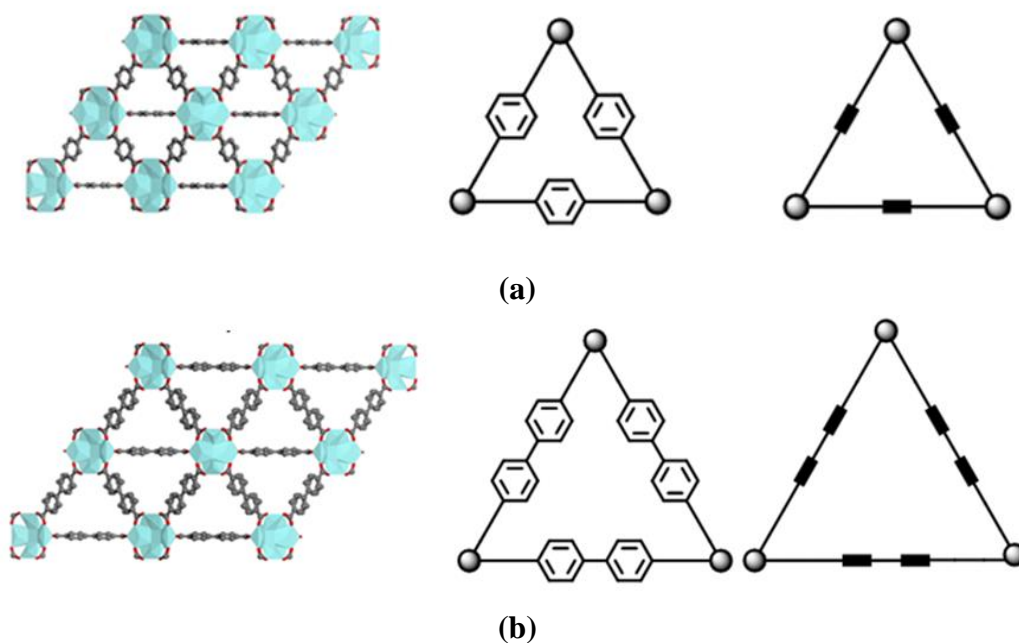
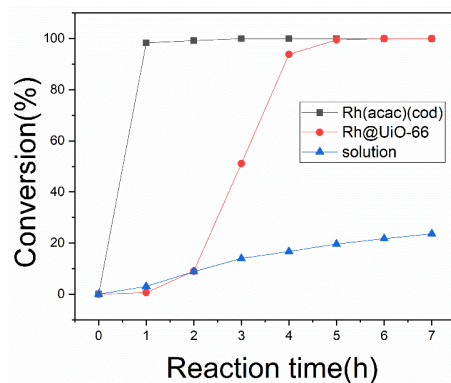
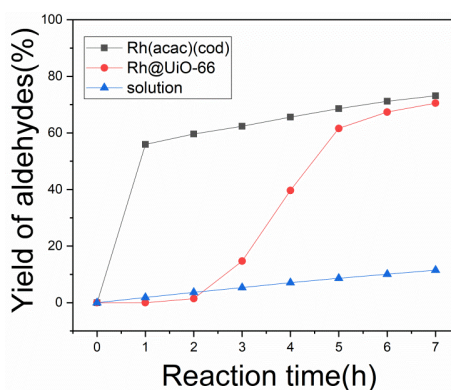


Figure 31. Simplified channel and linker orientation of (a) UiO-66 and (b) UiO-67.

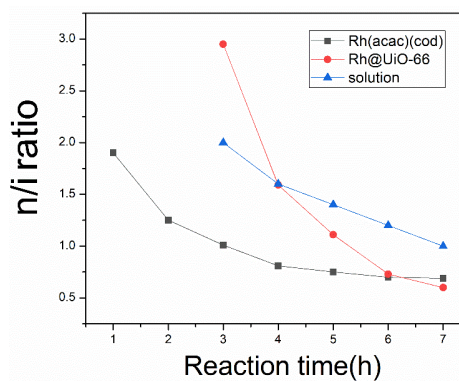
The leaching test was done to detect the Rh active species released into the solution during the reaction. Figure 32 show the results of hydroformylation of *n*-hexene catalyzed with the leached solution Rh(acac)(cod) and Rh@UiO-66, respectively. The conversion of *n*-hexene with leached solution is very low and increases continuously and slowly with reaction time. The low activity of the leached solution indicates that the Rh-supported catalyst is very stable against leaching. Only a little amount Rh was leached into the solution. In contrast, the Rh(acac)(cod) is highly active and the reaction shows a rapid increase to nearly 100% after 1h. The catalytic behaviour of the leached solution is significantly different from the hydroformylation with the MOF catalyst. Hence, the observed induction time and sudden increase in conversion is typical for the MOF catalyst and not caused by leaching. The yield of aldehyde goes nearly in parallel with the conversion. The *n/i* ratio observed with the leached solution and Rh(acac)(cod) at the beginning of the reaction is *ca.* 2. Whereas the *n/i* selectivity of the Rh@UiO-66 is significantly higher (*n/i*=3), which is due to the confinement in the MOF framework.



(a)



(b)



(c)

Figure 32. Comparison of the catalytic performance (conversion, aldehyde yield and *n/i*-aldehyde ratio) of *n*-hexene in the hydroformylation with (a) Rh(acac)(cod), (b) Rh@UiO-66 and (c) leached solution.

3.1.4 Summary

Synthesis of MOFs and Rh-supported catalysts are of high crystallinity with defined pore size: MOF-808 > UiO-67 > UiO-66. The obtained of μm -sized particles and represent meso-crystals composed of aggregated small sized nanoparticle (10-30nm).

The catalysts contain a hierarchical pore system of interconnected inter-particles featuring macro and mesopores as well as intra (nano) particle medium and large sized micropores. The structure facilitates the mass transfer to and from the catalyst. High porosity and surface area are proved during N_2 adsorption /desorption measurement. Specifically, the tested BET surface area follow the following order: UiO-67/Rh@UiO-67 ($1993.6 \text{ m}^2\text{g}^{-1}/1479.1 \text{ m}^2\text{g}^{-1}$) > UiO-66/Rh@UiO-66 ($1520.6 \text{ m}^2\text{g}^{-1}/ 1240.5 \text{ m}^2\text{g}^{-1}$) > MOF-808/Rh@MOF-808 ($1455.1 \text{ m}^2\text{g}^{-1}/987.1 \text{ m}^2\text{g}^{-1}$).

The Rh species are highly dispersed in an atomic scale and the test indirectly suggests that the Rh species are located nearby the zirconium and/or oxygen atoms in the MOF framework in the secondary building units. TG measurement confirmed all the catalysts are of high thermal stability, which proved that the catalyst remains stable during the catalytic reaction.

The pore size and structure have a markedly influence on catalytic properties of the Rh@Zr-MOF catalysts in the hydroformylation of *n*-alk-1-enes of different chain lengths.

All three Rh-supported catalysts Rh@UiO-66, Rh@UiO-67, and Rh@MOF-808 show a very high catalytic activity pointing to high dispersion of the rhodium i.e. the presence of catalytic “single site”. Indeed, the Rh loading is very low. The catalysts contain less than 1 Rh atom per 100 unit cells (Zr metal nodes). The apparent turn over numbers amount to 50.000-60.000 (based on total conversion).

The large pores facilitate the conversion of even very long chain molecules like the *n*-hexadecene and the formation of *i*-aldehydes from formed *i*-alkenes. Thereby the aldehyde selectivity and yield is increased. Nevertheless, the catalytic behaviour of the large pore Rh-supported Zr-MOF catalysts differ markedly due to the different

access to Rh sites in the secondary building units. The latter differ in pore size and type and in the arrangement of the linker.

The catalytic activity and the selectivity to aldehydes is highest with the Rh@UiO-67 and lowest with Rh@MOF-808. Although Rh@MOF-808 possesses the largest pores of *ca.* 18 Å, the access to the Rh in the side pockets of the pore is limited. However, the large pores facilitate the aldol condensation of formed aldehydes.

The pore structure of large pore containing Zr-based MOFs have an important impact on the catalytic performance due to the different confinement (formation of space demanding transition state) and access to active Rh sites located at the secondary building units. The influence is more complex due to the interplay of the large pores and the different accessibility of active Rh sites. In addition, reactions with inactive bulky olefins and mixtures of chain olefins have also been tried.

Compared with the reaction of linear olefins, although the yield of aldehydes and chain olefins have decreased significantly in the reaction with bulky olefins. However, the reaction has a selectivity close to 100%, due to the difficulty of rearrangement of double bonds in bulky olefins.

3.2 Hydroformylation of olefins over Rh-supported Zr-MOF DUT-67

The large pore Zr-MOF DUT-67 contains 2,5-thiophene dicarboxylic acid as a linker. Therefore, it is used as a model system for the study of the influence of heteroatom-substituted linker on the catalytic properties of Rh-supported MOFs. A highly porous and crystalline Zr-MOF DUT-67 was synthesized and used for the preparation of a supported rhodium catalyst. The material was characterized by XRD, SEM/TEM, FTIR, XPS, TGA, and nitrogen adsorption and desorption. The catalytic properties of Rh@DUT-67 have been investigated in the hydroformylation of n-alkenes with different chain length (C6, C8, C10, C12, C16) as well as of bulky olefins as 2,4,4-trimethylpentene, 3,3-dimethyl-1-butene, 4-methylstyrene, cyclohexene and cyclooctene. The stability and reusability of the catalyst was tested by cycling experiments using n-hex-1-ene as model substance.

3.2.1 Characterization

Figure 33 shows the powder X-ray diffraction patterns of as-synthesized Zr-MOF DUT-67, obtained after washing and extraction of the DMF solvent, and of the corresponding Rh-supported catalyst. The materials are highly crystalline and show a low background and narrow reflections especially in the diffraction angle range of $2\theta = 5-20^\circ$. The PXRD patterns correspond to the expected structure type and the positions of XRD reflections are similar to the simulated pattern¹³⁷. The crystallite sizes, determined from the reflection widths by the Scherrer formula¹⁴⁵, are *ca.* 30 nm. The structure of DUT-67 is maintained after Rh loading. However, the intensities of the reflections are decreased indicating some structural loss caused by the thermal and mechanical treatment during the Rh loading procedure. Reflections of metallic Rh species are not observed with Rh@DUT-67. Obviously, the very low loading (<0.05 wt%) facilitates a high dispersion of the supported rhodium likely in a single site manner.

The FTIR vibration spectra of the as-synthesized and rhodium supported DUT-67 are shown in Figure 34. The prepared materials show the typical vibration spectra of the linker molecule 2,5-thiophenedicarboxylic acid. The vibration bands are narrow and well resolved. The absorbances observed at *ca.* 1300-1700 cm^{-1} are assigned to the vibrations of the carboxylic groups. The vibration bands below 1000 cm^{-1} belong to =C-H deformation and C-S stretching vibrations of the thiophene ring. The rhodium

loading causes an increase of the intensities of the vibration bands. Additionally, the vibration band maxima shift (within 10 cm^{-1}) to higher wavenumber, indirectly confirming the Rh loading.

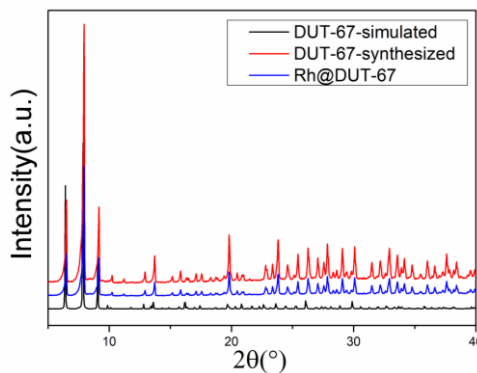


Figure 33. Simulated XRD pattern (bottom) and PXRD patterns of synthesized (top) and Rh-supported (middle) DUT-67.

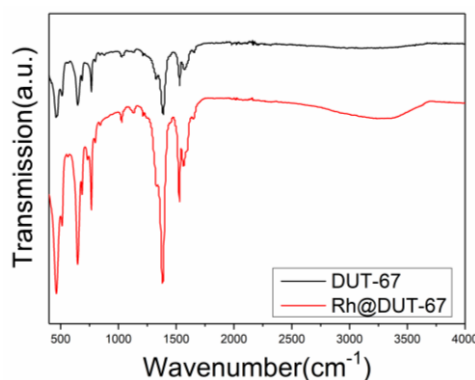


Figure 34. FTIR spectra of as-synthesized and Rh-supported Zr-MOF DUT-67.

The high resolution scanning electron microscopic (SEM) images of the rhodium-supported DUT-67 catalysts are shown in Figure 35. The SEM images show that DUT-67 is crystallized as micrometer sized particles (in 5000 times magnification). The higher magnification (50000 times) shows that the material consists of bulky well-shaped cubooctahedra of *ca.* 1.3 μm size. The TEM (Figure 35c) shows that the material contains an ordered large-size pore system. The pore sizes range from 0.73 to 1.78 nm, which is in line with the crystal structure data. The crystallite size is *ca.* 30nm, which agrees with the XRD data. Even with detailed inspection by high-resolution TEM, it was not possible to detect any Rh particles. Obviously the rhodium is highly dispersed and forms single-site like active sites.

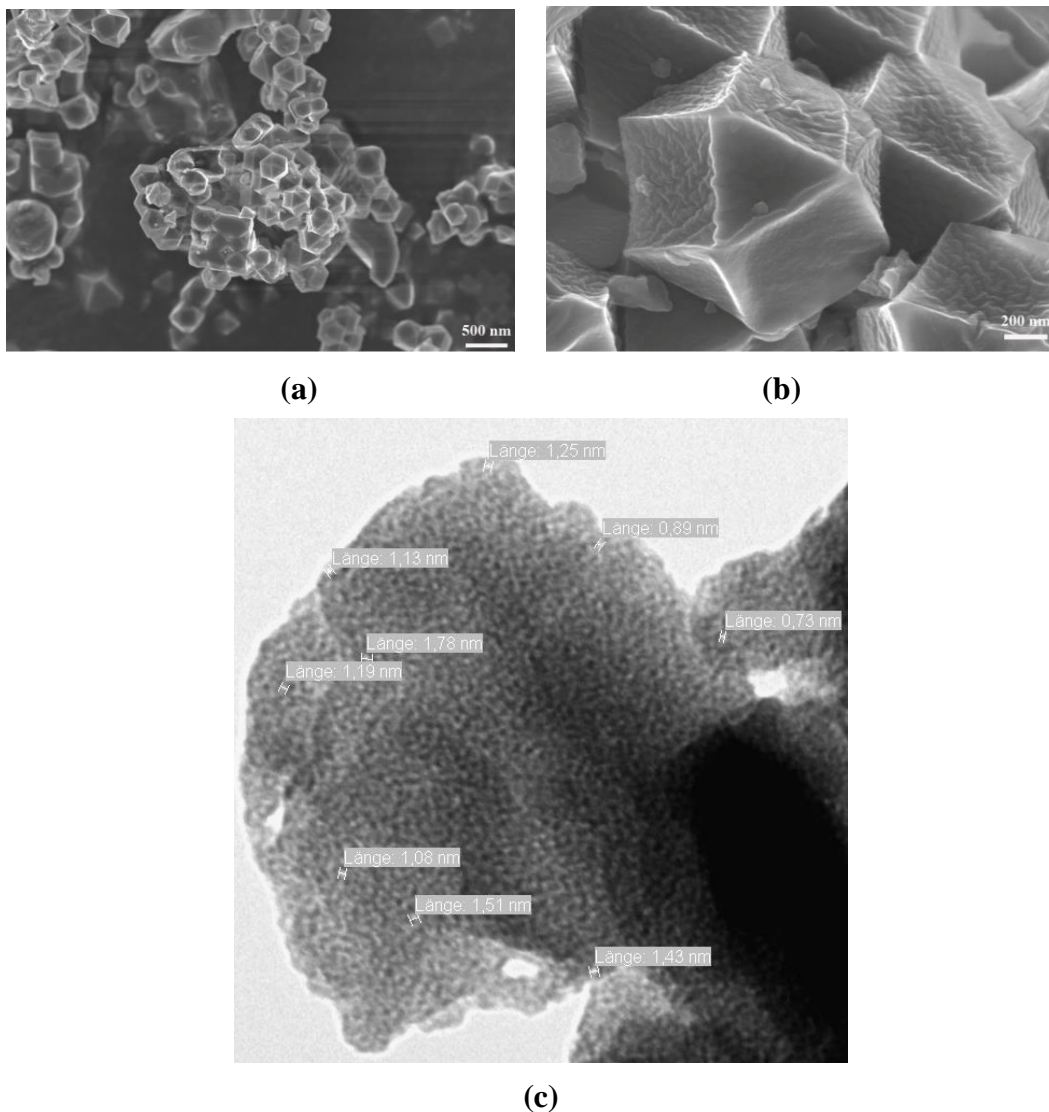


Figure 35. SEM images of Rh-supported DUT-67 at (a) 5k and (b) 50k magnification, and (c) TEM images of Rh-supported DUT-67 with marked pore sizes.

N_2 adsorption and desorption isotherms of the materials are of type I (Figure 36). A markedly increase of nitrogen up take at low relative pressure below $p/p_0 < 0.03$ indicates the presence of micropores. The shape of the isotherm at low pressure is not rectangular. The curved shape between p/p_0 0.01 to 0.03 is due to the large open extended pores in the system. This finding is confirmed by the TEM shown above. The further continuous nitrogen up take with increasing relative pressure is due to the presence of mesopores. The formation of additional mesopores (*ca.* 4% by total volume) in this DUT-67 is caused by the addition of acetic acid as misleading linker to the synthesis mixture. The acetic acid prevents formation of linker bridges by blocking Zr-node coordination sites and competes with the

2,5-thiophenedicarboxylic acid linker which can act as bridge between the Zr nodes. The material is highly porous. The calculated BET surface areas of DUT-67 and Rh@DUT-67 are 1013.7 and 972.2 m² g⁻¹, respectively. The pore volumes of DUT-67 and Rh@DUT-67 calculated basic on DFT mode from their adsorption isotherms are 0.379 and 0.369 cm³ g⁻¹, respectively. The Zr-MOF DUT-67 shows a high stability. Even after Rh loading the specific surface area and the pore volume are nearly maintained.

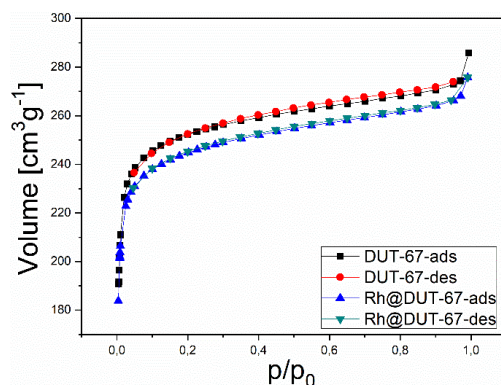


Figure 36. N₂ adsorption and desorption isotherms of as-synthesized and Rh-supported DUT-67.

X-ray photoelectron spectroscopy was used to characterize the valence state of C, O, S, Zr and Rh in the Zr-MOF (Figure 37). With Rh@DUT-67, a Rh signal was observed in the XPS spectrum. The amount of Rh was calculated to be <0.04wt%. Although it is very low, the Rh loading causes significant shifts of the O_{1s} and S_{2s}XPS signal maxima to higher energy. The oxygen signal is shifted by *ca.* 0.9eV and the sulfur signal by up to 1.3eV (Table. 4). These shifts show a strong interaction of the rhodium with the oxygen and sulfur indicating that the rhodium is likely located at the linker in the large windows of the pore system. Whereas, only minor shifts of 0.2 to 0.3 eV to higher energy are found with the Zr_{3d} and Zr_{3p} signals.

The thermogravimetric weight loss curve of DUT-67 is shown in Figure 38. The slight increase in weight at the beginning of the run is an artefact. It is due to the decrease in the density of argon at higher temperature. The first weight loss at 34°C to 150 °C of *ca.* 14wt% is mainly due to the removal of loosely and internal surface bound water located in the pores of the Zr-MOF. The second weight loss of *ca.* 8wt% between *ca.* 180 to 350 °C, is assigned to the removal the residual solvent (DMF), strongly bound water or possibly dehydroxylation of the zirconium node. The

framework is stable up to 350 °C. Beyond 350 °C the structure starts to decompose to zirconium oxide.

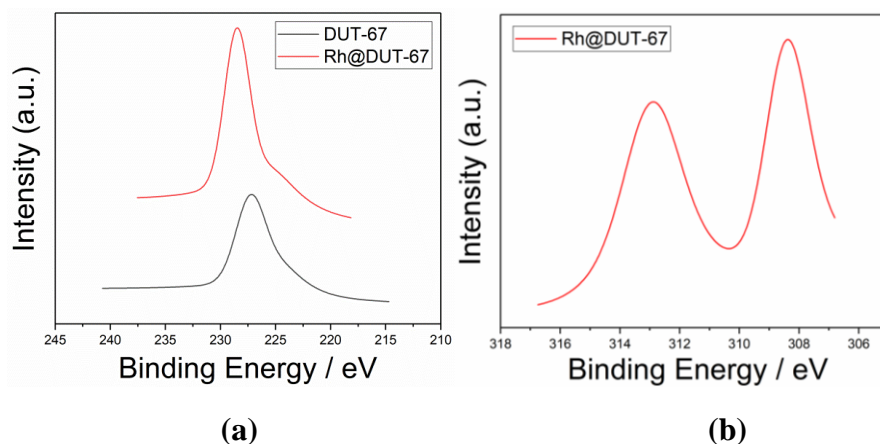


Figure 37. XP spectra of (a) S_{2s} signal of as-synthesized and Rh-supported DUT-67, and (b) Rh_{3d} signal of Rh-supported Zr-MOF DUT-67.

Table 4. Binding energies of carbon, oxygen, sulfur, zirconium and rhodium in the XP spectra of the as-synthesized and Rh-supported DUT-67.

Signal	Binding energy(eV)					
	C_{1s}	O_{1s}	S_{2s}	Zr_{3d}	Zr_{3p}	Rh_{3d}
DUT-67	284.9	533.1	227.2	181.4	333.3	
	288.7			183.6	347.1	
Rh@DUT-67	284.9	534.0	228.5	181.6	333.3	308.4
	288.8			183.9	347.1	312.9

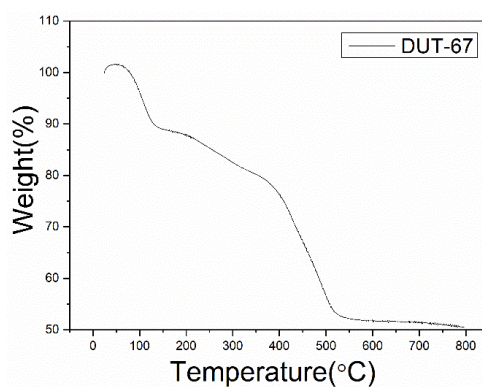


Figure 38. Thermogravimetric weight loss curves (TGA) of DUT-67 in the argon atmosphere.

3.2.2 Catalysis

3.2.2.1 Hydroformylation of linear *n*-alkenes

The catalytic performance of Rh@DUT-67 in the hydroformylation of olefins was tested with *n*-alk-1-enes with different chain lengths (C6 to C16). Both *n*- and *i*-aldehydes are found as reaction products. In addition, internal alkenes are formed by double bond shift isomerization. In certain cases aldol condensation was observed. Hydrogenation of alkenes was not found. The blank tests with *n*-hexene and *n*-octene show that the de-solvated as-synthesized DUT-67 alone is not catalytic active. It does not catalyze the double bond shift in *n*-alk-1-enes to internal positions (*i*-alkenes), or the hydroformylation of alkenes to aldehydes even after 21h of reaction.

The total conversions of different *n*-alk-1-enes such as *n*-hexene, *n*-octene, *n*-decene, *n*-dodecene and *n*-hexadecene in dependence on the reaction time over Rh@DUT-67 are shown in Figure 39. The reaction proceeds rapidly. After 1 hour 17% to 33% of conversion is achieved. Nearly full conversion is achieved after 3h to 4h depending on the type of the reactant molecule. In tendency the conversion decreases with the chain length with exception of *n*-hexadecene. The conversion follows the order: *n*-hexadecene \geq *n*-hexene $>$ *n*-octene \approx *n*-decene $>$ *n*-dodecene after 2h reaction. The fast conversion demonstrates the high activity of the catalyst as well as high accessibility of Rh active sites. The large pores facilitate the mass transfer. The large void space around the rhodium at the organic linker favors the formation of the space demanding transition state, i.e. the catalytic reaction. Surprisingly, the ultra-long chain *n*-hexadecene show fastest conversion in the first 2h. The long chain *n*-hexadecene has a size of *ca.* 1.8 nm are, which is close to the channel size. Therefore, these molecules are arranged preferentially along the channel direction and move in a quasi-one-dimensional manner. i.e. similar to file diffusion. This allows a faster moving through the channels can hardly overcome each other. The mass transfer is enhanced markedly.

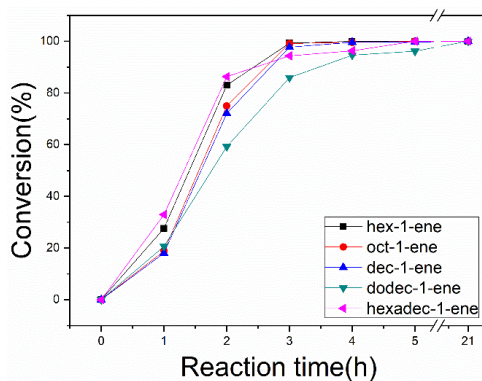


Figure 39. Conversion of the *n*-hexene, *n*-octene, *n*-decene, *n*-dodecene, and *n*-hexadecene in the hydroformylation over Rh@DUT-67 in dependence on the reaction time.

Figure 40 shows the selectivity to aldehydes in the hydroformylation of *n*-alkenes over Rh@DUT-67 in dependence on the reaction time. After 1h reaction the selectivity to aldehydes is *ca.* 12-38% and *ca.* 20 to 50%.after 2 hours. As seen in the figure, generally the selectivity to aldehydes increases continuously during the course of reaction. At the same time, formation of *i*-alkenes is also observed. The selectivity to aldehydes reaches finally 50-85% due to the conversion of *i*-alkenes. The aldehyde selectivity decreases in the order: *n*-hexene > *n*-hexadecene > *n*-octene > *n*-dodecene > *n*-decene. The high aldehyde selectivity of *n*-hexadecene is in line with the file motion in the straight channel of DUT-67, thereby passing directly the active sites. The latter are located at the linker directed to the channel.

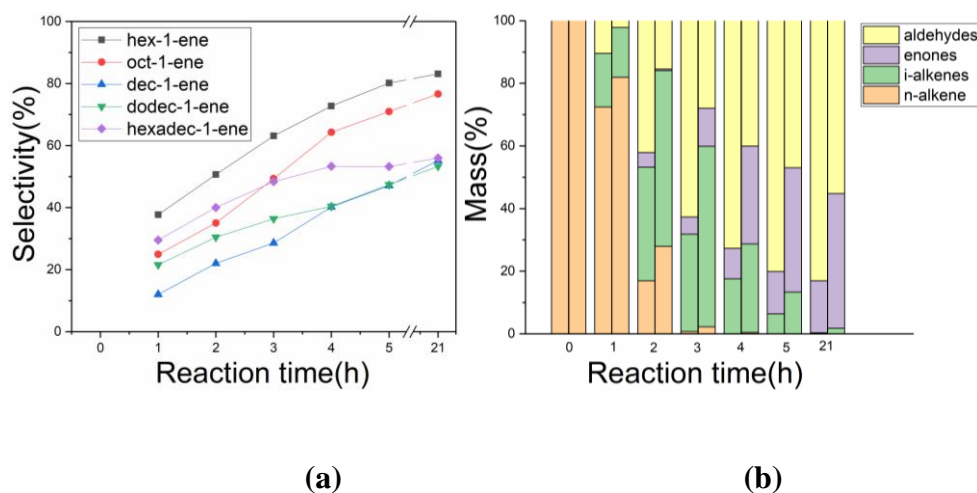


Figure 40. (a) Selectivity to aldehydes in the hydroformylation of *n*-hexene, *n*-octene, *n*-decene, *n*-dodecene, and *n*-hexadecene over Rh@DUT-67 in dependence on the

reaction time. (b) Composition of the reaction mixtures obtained in the hydroformylation of *n*-hexene (left) and *n*-decene (right) over Rh@DUT-67 catalyst.

In Figure 41 are shown the yields of aldehydes for different *n*-alkenes in dependence of the reaction time obtained over the Rh-supported DUT-67. The yield of aldehyde is low after 1h due to the low conversion and in part of the low aldehyde selectivity, e.g. with *n*-decene and *n*-dodecene. Whereas with *n*-hexene and *n*-hexadecene, *ca.* 10% aldehyde yield are observed due the high conversion and selectivity. The yield increases continuously during the reaction. Highest yields of aldehydes (75-85%) are observed with *n*-hexene and *n*-octene after 5h. Whereas the yields are much lower (*ca.* 50%) with *n*-decene, *n*-dodecene and *n*-hexadecene due to the competing aldol condensation. The aldol condensation requires a face to face arrangement of aldehydes groups. It is best achieved for long chain molecules by the confinement in the channels. This confinement effect, i.e. the arrangement of the molecule in the channel direction is largest in case of the long chain *n*-hexadecane. Therefore, the aldol condensation of the formed heptadecanal starts early after 3h of reaction.

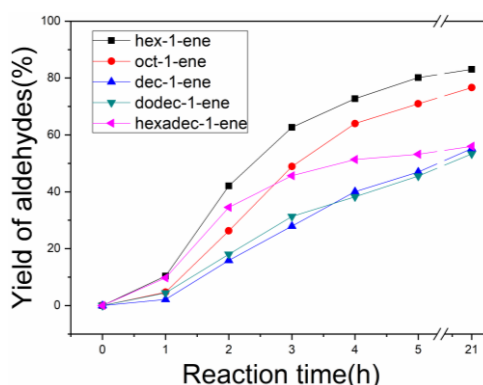


Figure 41. Yield of aldehydes in the hydroformylation of *n*-hexene, *n*-octene, *n*-decene, *n*-dodecene, and *n*-hexadecene over Rh@DUT-67 in dependence on the reaction time.

The *n/i*-aldehyde ratios of the products are shown in Figure 42. It is worth noting that the initial *n/i*-aldehyde ratio for all catalytic runs is similar and *ca.* 2.5-3. Then the ratio decreases until the end of the reaction. At the beginning of the reaction, all reaction mixtures contain only the *n*-alkenes. Therefore *n*-aldehydes are preferentially formed. During the course of reaction, increasing amounts of *i*-alkenes are formed by the double bond shift reaction and are converted to the corresponding *i*-aldehydes. Hence, the *n/i*-aldehyde decreases markedly with

reaction time. The decrease is less pronounced with *n*-hexadecene because of the consumption of aldehydes by the aldol reaction.

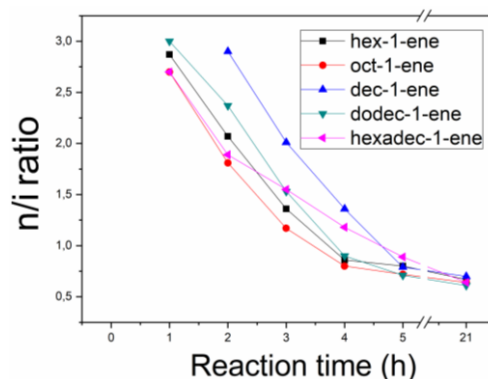


Figure 42. *n/i*-aldehydes ratio of *n*-hexene, *n*-octene, *n*-decene, *n*-dodecene and *n*-hexadecene in the hydroformylation over Rh@DUT-67 in dependence on the reaction time.

The lifetime is an important aspect concerning the use of catalysts. Therefore the re-usability of the Rh@DUT-67 was examined using *n*-hexene as model substance. For this, the catalyst was separated from the reaction solution after the catalytic run by simple filtration. The separated catalyst was all washed by toluene and used in the next reaction run. The recovered Rh@DUT-67 exhibited high catalytic efficiency of *ca.* 95% after the first run. After 5 runs, only a loss of 20% of the starting activity was observed. The *n/i*-ratio of *ca.* 3, i.e. the regioselectivity of *ca.* 75% at the beginning of reaction, is maintained. (Figure 43).

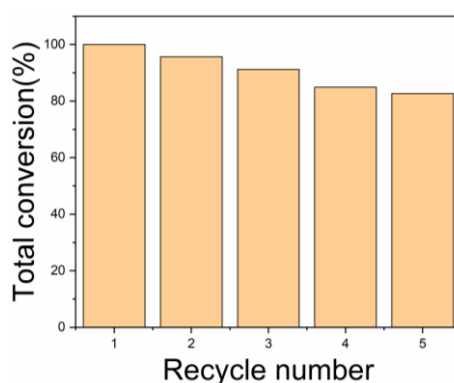


Figure 43. Re-usability of Rh@DUT-67 catalyst in the hydroformylation of *n*-hexene.

3.2.2.2 Hydroformylation of bulky olefins

Figure 44 shows the yield of aldehydes in dependence of the reaction time observed with different sized bulky olefins in the hydroformylation with Rh@DUT-67. The yield of the aldehydes equals to the conversion because double bond shift cannot occur. With 3,3-dimethyl-1-butene (DMB) the formation of aldehyde starts rapidly and achieves *ca.* 65% after 3h of reaction. Conversion of other bulky olefins proceeds much slower. The conversion and yield of aldehyde decrease in the order: 3,3-dimethyl-1-butene >>> 4-methylstyrene >> cyclooctene > cyclohexene > 2,4,4-trimethylpentene. The final yields of 45% to 80% are achieved. The decrease in the yield with different olefins is due to the limited accessibility of active sites by the bulky molecules. The 4-methylstyrene is a stiff molecule and less flexible due to phenyl group. Lowest activity is observed with the large 2,4,4-trimethylpentene (TMP) because the mobility is low and double bond is additional shielded by the methyl group. Even though the size of cyclohexene is smaller than that of the cyclooctene, cyclohexene is less converted. It is additional stabilized in a half-chair conformation, which requires higher activation energy for the reaction¹⁴⁶.

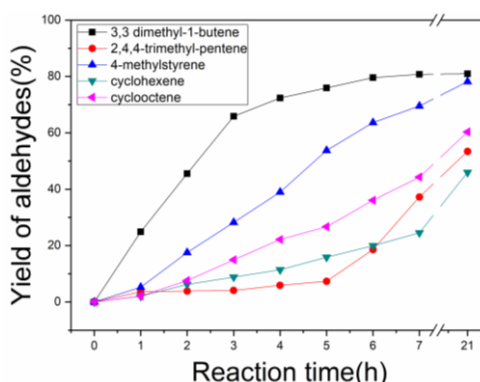


Figure 44. Yield of aldehyde in the hydroformylation of 3,3-dimethyl-1-butene, 4-methylstyrene, cyclooctene, cyclohexene, and 2,4,4-trimethylpentene over Rh@DUT-67 in dependence on the reaction time.

3.2.3 Summary

Synthesis of DUT-67 and corresponding Rh-supported DUT-67 (Rh@DUT-67) are of highly crystalline with defined pore size.

The regular cube-like shaped crystals are composed of small sized nanoparticle (30nm). The estimated pore sizes by TEM are *ca.* 0.7 to 1.80nm, which are in line with the theoretical pore size of DUT-67 (16.6Å). The open pore structure facilitates the mass transfer to and from the catalyst and access to the active site.

High porosity and surface area are proved by N₂ adsorption /desorption measurement. Specifically, the tested BET surface area of DUT-67 and Rh@DUT-67 are 1013.7 and 972.2 m² g⁻¹, respectively.

The Rh species are highly dispersed in an atomic scale and not visible in high resolution TEM. XPS indirectly suggests that the Rh species are located nearby the sulfur atoms in the MOF framework in the organic linker by the markedly shift of sulfur signal after Rh loading.

TG measurement confirmed the catalystRh@DUT-67 are thermal stable up to 350 °C, which proved that the catalyst remains stable during the catalytic reaction.

The Rh-supported catalyst Rh@DUT-67 shows very high catalytic activity pointing to high dispersion of the rhodium i.e. the presence of catalytic “single site”. Even in a low amount of Rh (0.04wt%), fast conversions and high yield of aldehydes are observed in the hydroformylation with *n*-alkenes.

The large pore size and high accessibility also facilitate the conversion of large sized bulky olefins and aldol condensation of primary formed aldehydes.

The Rh-supported DUT-67 could be easily separated from the products by simple decantation and reused. The total conversion remains 80% after 5 times recycling.

The Rh-supported DUT-67 represents a promising catalytic system for the catalytic applications in the hydroformylation. Due its stability, porosity and accessibility the MOF DUT-67 MOFs is it is in general a promising material for the immobilization of catalytic active components.

3.3 Hydroformylation of olefins over Rh-supported Zr-MOF NU-1000

In this work we intend to investigate the catalytic performance with mesopore Zr-MOF catalysts. For this purpose, rhodium-supported zirconium-based mesoporous MOF NU-1000 were prepared and characterized by PXRD, FTIR, SEM/TEM, XPS, and nitrogen adsorption. The catalytic performance was studied in the hydroformylation of olefins to the corresponding aldehydes using linear olefins with different chain lengths (C6, C8, C10, C12, and C16) as model substances.

3.3.1 Characterization

The powder X-ray diffraction patterns of as-synthesized NU-1000 and the corresponding Rh-supported catalyst Rh@NU-1000 are shown in Figure 45. The materials are highly crystalline and show a low background and narrow reflections especially in the diffraction angle range of $2\theta = 2$ to 10° . The PXRD patterns correspond to the expected structure type and the positions of XRD reflections are similar to the simulated pattern. The positions of observed XRD reflections are similar to the simulated patterns and other report^{138,140}. The signals indicated that the structure of NU-1000 maintained after Rh loading. However, the intensity of the reflections is decreased by further mechanical and thermal treatment during the Rh loading procedure. Rhodium metal reflections were not observed in PXRD patterns of Rh@NU-1000, which indirectly proved that the supported rhodium was very low concentrated ($<0.05\text{wt}\%$) and highly dispersed in the pores.

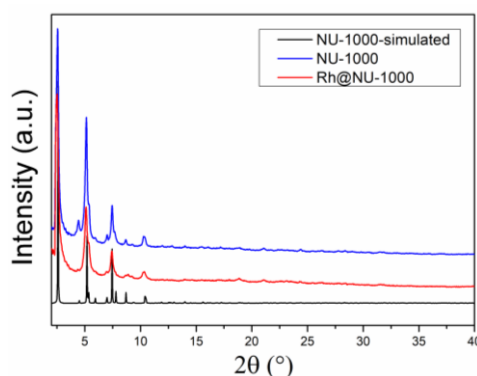


Figure 45. Simulated XRD pattern (bottom) and PXRD patterns of synthesized (top) and Rh-supported (middle) NU-1000.

The FTIR spectra of NU-1000 and rhodium supported Rh@NU-1000 are shown in Figure 46. All the prepared materials show the typical vibrational spectra of the linker molecules. The vibrational bands are narrow and well-resolved. The absorption bands of NU-1000 appearing between 640-800 cm^{-1} are assigned to the Zr–O longitudinal and transverse mode vibrations, respectively. The narrow and intense signals at 1400-1650 cm^{-1} are stretching of the carboxylate groups of the ligand. Slight shift to higher wavenumber and (within 10 cm^{-1}) an increase in the intensities of the vibrational bands were observed in the rhodium loading samples, indirectly confirming the Rh loading.

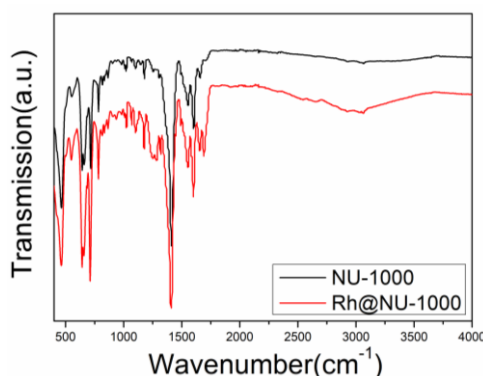


Figure 46. FTIR spectra of as-synthesized and Rh-supported NU-1000.

Nitrogen adsorption and desorption isotherms of as-synthesized and Rh-supported NU-1000 are of type I (Figure 47). A markedly increase of nitrogen up take at low relative pressure below $p/p_0 < 0.02$ indicates the presence of micropores. The increase of the isotherms at relative pressure (of up to $p/p_0 = 0.2$) exhibits a larger mesoporous step. Brunauer–Emmett–Teller (BET) theory calculations reveal that the calculated surface areas of the porous NU-1000 and the corresponding Rh-supported catalysts NU-1000/Rh@NU-1000 are $1139.5 \text{ m}^2\text{g}^{-1}$ / $404.7 \text{ m}^2\text{g}^{-1}$, respectively. The significant decrease in the specific surface area and pore volume detected after Rh loading is caused by the additional mechanical stress and shrinkage due to the stirring followed by the additional heating of the samples to remove the adsorbed solvent. It cannot be excluded that some pores are blocked by the rhodium but the loading is too low to cause a significant effect.

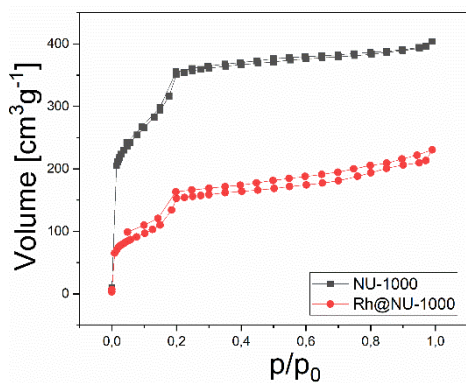


Figure 47. N₂ adsorption and desorption isotherms of starting (black) and Rh-supported NU-1000 (red).

Thermal stability is shown by TGA measurement (Figure 48). TGA performed on the activated MOF samples suggests structural changes or different amounts of chemisorbed material. The slight increase in weight at the beginning was caused by the decrease in the density of argon at higher temperature. The curve shows two steps of weight loss prior to the formation of final ZrO₂ product. The two step decrease of the weight was attributed to the removal of guest solvent (DMF, water) and organic linker, respectively.

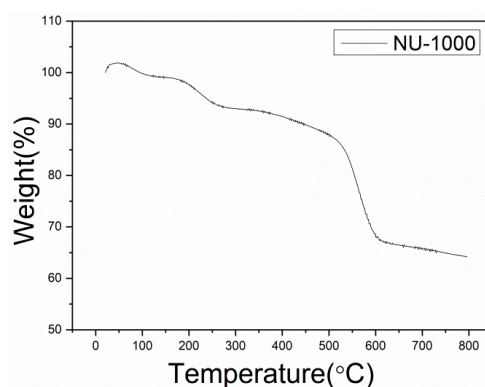


Figure 48. Thermogravimetric weight loss curves (TGA) of NU-1000 in the argon atmosphere.

The X-ray photoelectron spectroscopy was used to characterize the electronic state of the elements C, O, Zr and Rh in the MOF structure. The results are shown in Figure 49. Although it is very low, the Rh loading causes significant shifts of the O_{1s} and Z_{3p} XPS signal maxima to higher energy. The oxygen signal is shifted by *ca.* 1.3 eV and the zirconium signal by up to 1.7eV (Table. 54). These shifts show a strong interaction of the rhodium with the oxygen and zirconium indicating that the rhodium is likely located at the metal nodes in the framework.

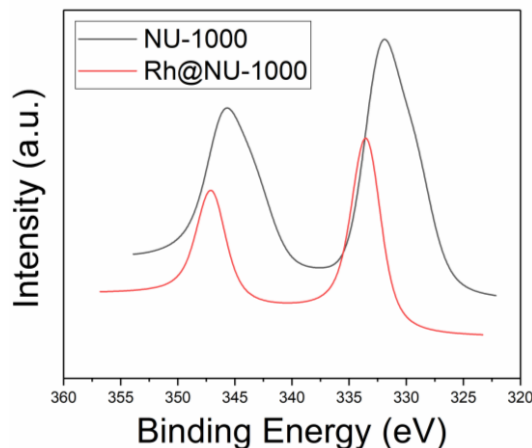


Figure 49. XPS spectra of Zr_{3p} signal of as-synthesized and Rh-supported NU-1000.

Table 5. Binding energies of carbon, oxygen, zirconium and rhodium in the XP spectra of the as-synthesized and Rh-supported NU-1000.

Signal	Binding energy (eV)				
	C1s	O1s	Zr3d	Zr3p	Rh3d
NU-1000	284.9	528.9	181.2	331.8	
	288.8	531.0	183.5	345.6	
Rh@NU-1000	284.9	530.2	182.6	333.5	308.1
	288.8	532.1	184.8	347.1	312.7

3.3.2 Catalysis

3.3.2.1 Hydroformylation of linear *n*-alk-1-enes

The catalytic performance of Rh@NU-1000 in the hydroformylation of linear *n*-alkenes of different chain lengths was investigated using *n*-hexene, *n*-octene, *n*-dodecene, *n*-dodecene, and *n*-hexadecene as model substances. Both *n*- and *i*-aldehydes are obtained. Simultaneously, double bond shifted internal alkenes obtained from *n*-alkene isomerization are formed as side-products. No notable alkanes are generated from alkenes by hydrogenation of alkenes during the course of reaction. The blank experiments with *n*-hexene and *n*-octene indicated that NU-1000 alone does not catalyze the isomerization of *n*-alkenes to *i*-alkenes, or the hydroformylation of alkenes to aldehydes even after 21h of treatment..

The course of conversion of different *n*-alkenes (*n*-hexene, *n*-octene, *n*-decene, *n*-dodecene and *n*-hexadecene) over Rh@NU-1000 is shown in Figure 50. Generally the reaction proceeds rapidly. After 2 hour 32% to 65% of conversion is achieved. The conversion follows the order: *n*-hexadecene \approx *n*-hexene \approx *n*-dodecene > *n*-octene > *n*-decene. Nearly 90% conversion is achieved after 5h depending on the type of the reactant molecule. The fast conversion demonstrates the high activity of the catalyst as well as the accessibility of Rh active sites. The large pores facilitate the mass transfer. Interestingly, also the long chain *n*-hexadecene shows fast conversion close to that of the short chain *n*-hexene in the first 2h. This is probably due to the large pores which facilitate the mass transfer as well as the high mobility and enhanced arrangement possibilities of the long-chain *n*-hexadecene with respect to the active sites in the confined space of the extra-large pores (*ca.* 30Å).

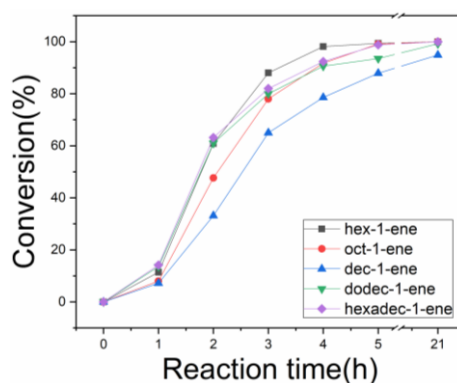


Figure 50. Conversion of *n*-hexene, *n*-octene, *n*-decene, *n*-dodecenem, and *n*-hexadecene in the hydroformylation over Rh@NU-1000 in dependence on the reaction time.

Figure 51 shows the selectivity to aldehydes observed for the hydroformylation of *n*-alkenes over Rh@NU-1000 in dependence of the reaction time. As can be seen from the graph generally the selectivity to aldehydes increases during the course of reaction. At the beginning, the *n*-aldehyde is formed only. With increasing formation of double bond shifted *i*-alkenes also formation of *i*-aldehydes starts. Thus the selectivity of aldehydes increases continuously. This is also well reflected in the decrease of the *n*/*i*-ratio during the course of reaction as shown below.

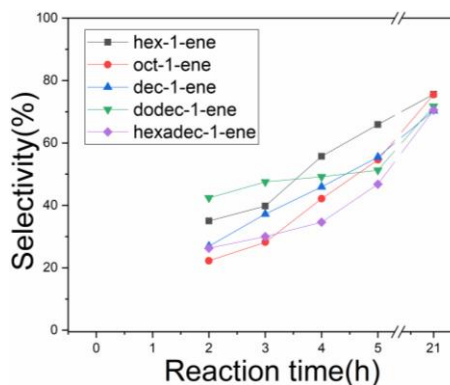


Figure 51. Selectivity to aldehydes in the hydroformylation of *n*-hexene, *n*-octene, *n*-decene, *n*-dodecene, and *n*-hexadecene over Rh@NU-1000 in dependence on the reaction time.

In Figure 52a shows the yields of aldehydes for different *n*-alkenes in dependence of the reaction time obtained over the Rh-supported NU-1000. After starting of the reaction aldehydes are formed continuously. Hydroformylation with *n*-dodecene shows highest the yield of *ca.* 37% close to that of *n*-hexene. The yield of aldehydes follows the order: *n*-dodecene \geq *n*-hexene > *n*-hexadecene > *n*-decene \approx *n*-octene. Final yields of 65 to 75% are obtained after 21 h. Variation in the aldehyde yield, i.e. the slower increase in the yield with *n*-dodecene are caused by the competing aldol condensation consuming the aldehyde. It is more pronounced in the selectivity behavior (Figure 51).

The compositions of the reaction mixtures of during the hydroformylation of *n*-hexene and *n*-decene are shown in Figure 52b. During the reaction, the *n*-alkenes are continuously converted to aldehydes and a large portion of *i*-alkenes (*ca.* 50% *i*-hexenes and *ca.* 35% *i*-decenes after 3h). The aldehyde content increases continuously, In contrast, the *i*-alkene content decreases only slowly. Even after 21 h some *i*-alkenes remain. Obviously the access of internal *i*-alkenes to the active Rh sites of NU-1000 is hindered. It shows that the Rh-sites are not located in the extra-large pores but in the smaller, triangular pores. Further special restrictions arise from the stiff and large tetrapodal pyrene benzoic linkers connecting the Zr nodes. Otherwise it would be not understandable that even the small *i*-hexenes (*ca.* 17%) are not fully converted as observed e.g. with MOF DUT-67.

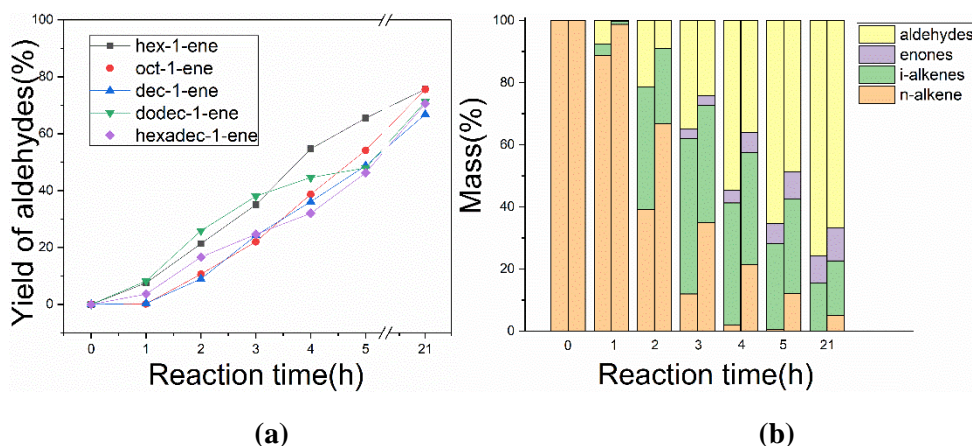


Figure 52. (a) Yield of aldehydes with *n*-hexene, *n*-octene, *n*-decene, *n*-dodecene and *n*-hexadecene in dependence on the reaction time over Rh@NU-1000. (b) Composition of the reaction mixtures obtained in the hydroformylation with *n*-hexene (left) and *n*-decene (right) over Rh@NU-1000 catalyst.

The *n/i*-aldehyde ratios are shown in Figure 53. The *n/i*-aldehyde ratios are *ca.* 2.7-3 (2.4 with *n*-dodecene) up to 2h of reaction, where already *ca.* 30 to 65% of conversion is achieved). Thereafter, *n/i*-ratio decreases to less than 1.0 after 21h due to the conversion of *i*-alkenes. Besides, the specifically the formed *n*-aldehyde are consumed by the competing aldol condensation. This is also a reason for the observed decrease of the *n/i*-ratio after longer reaction time.

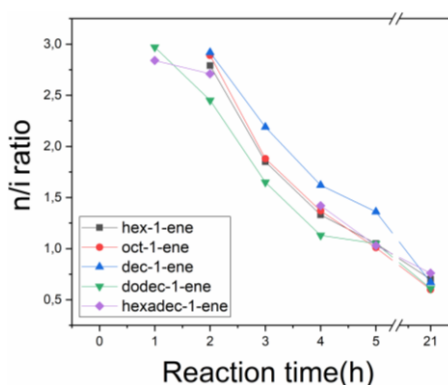


Figure 53. *n/i*-aldehydes ratio of *n*-hexene, *n*-octene, *n*-decene, *n*-dodecene and *n*-hexadecene in the hydroformylation over Rh@NU-1000 in dependence on the reaction time.

3.3.2.2 Hydroformylation of bulky olefins

Figure 54 has shown the yield of aldehydes in dependence of the reaction time observed with different sizes of bulky olefins (3,3-dimethyl-1-butene, 2,4,4-trimethyl-pentene, 4-methylstyrene, cyclohexene, cyclooctene) in the hydroformylation with Rh@NU-1000. The yield of the aldehydes equals to the conversion because double bond shift cannot occur, thus the selectivity of the reaction is close to 100% due to no possibility of double bond isomerization. Specifically, the yields of hydroformylation with 3,3-dimethyl-1-butene was significantly higher (82% yield) than that of other bulky olefins due to its relative small molecular size and high reactivity. In the hydroformylation with 4-methylstyrene and 2,4,4-trimethyl-pentene, the reaction proceeds slowly because the molecular size of the substrate is large. When the reaction proceeded after long time, the yield reached to a relative high amount (*ca.* 80% and *ca.* 63% respectively) at 21h. In contrast, in the hydroformylation with large and lower reactive molecules as cyclohexene and cyclooctene, the conversion proceeds markedly slower. Cyclohexene is less reactive because it is additional stabilized in a half-chair conformation, which requires higher activation energy for the reaction. Thus the aldehyde yield was higher (48%) with cyclooctene than that of cyclohexene (36%) even though the molecular size is larger.

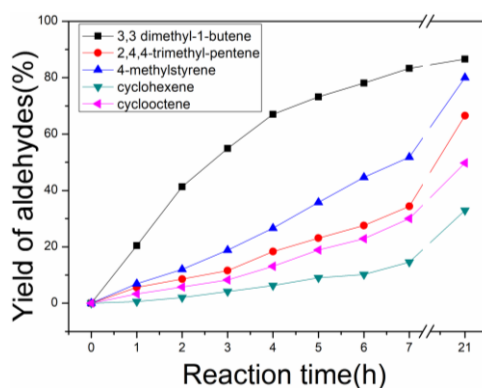


Figure 54. Yield of aldehyde in the hydroformylation of 3,3-dimethyl-1-butene, 4-methylstyrene, cyclooctene, cyclohexene, and 2,4,4-trimethylpentene over Rh@NU-1000 in dependence on the reaction time.

3.3.3 Summary

Synthesis of NU-1000 and Rh-supported NU-1000 (Rh@NU-1000) are of high crystallinity with defined pore size.

High porosity and surface area are proved by N₂ adsorption /desorption measurement. Specifically, the tested BET surface area of NU-1000 and Rh@NU-1000 are 1139.5m²g⁻¹ and 404.7m²g⁻¹, respectively. The observed decrease in the specific surface area and pore volume detected after Rh loading is caused by the additional mechanical stress and shrinkage due to the stirring followed by the additional heating of the samples to remove the adsorbed solvent.

The Rh species are highly dispersed in an atomic scale and the XPS indirectly suggests that the Rh species are located nearby the Zr and O atoms in the metal nodes of the framework.

TG measurement confirmed NU-1000 is thermal stable under 400 °C, which proved that the catalyst remains stable during the catalytic reaction.

The Rh species in the framework of NU-1000 are highly dispersed in an atomic scale and the XPS indirectly suggests that the Rh species are located nearby the sulfur atoms in the MOF framework in the organic linker.

The Rh-supported catalysts Rh@NU-1000 shows very high catalytic activity pointing to high dispersion of the rhodium i.e. the presence of catalytic “single site”.

Even in a low amount of Rh, fast conversions of *n*-alkenes and high yield of aldehydes are observed. Moreover, the large mesopore also facilitates the conversion of large sized bulky olefins and aldol condensation.

3.4 Structure - catalytic property - relationships in the hydroformylation over Zr-MOFs

Hydroformylation is studied over five different Zr-MOFs with different sized linear and bulky olefins. The maximum pore size of the catalysts follows the order: Rh@UiO-66 < Rh@UiO-67 < Rh@DUT-67 < Rh@MOF-808 < Rh@NU-1000. The influence of the structure on the catalytic performance is discussed. Location of the catalytic site and the accessibility to the catalytic site are different. Among them, the position of active Rh site is different from other catalysts, which is near to the organic linker. In the other four catalysts, rhodium is located in the cage of the framework, close to the Zirconium site.

In the framework of Rh@DUT-67, a large void space around the organic linker can be used for the catalytic reaction. Thus the fastest conversion of olefins is observed. Although Rh@MOF-808 has large pores, the small cage size limits the accessibility of the olefin to the rhodium active site. Thus the conversion is slower than that with Rh@UiO-67 and Rh@NU-1000. Overall, the catalytic performance is best with Rh@DUT-67 and decreased in the order Rh@DUT-67 > Rh@NU-1000 > Rh@UiO-67 > Rh@MOF-808 > Rh@UiO-66.

Both the pore size and the accessibility contribute to the catalytic performance. The composition in the reaction mixture over *n*-hexene and *n*-decene after 21h are shown in Figure 55 and table 6. In the reaction with Rh@DUT-67, only a small amount of *i*-decenes are unreacted and left in the final reaction product, and a large amount of enones are formed. This is due to its large pore size and accessible Rh sites around the linker. Thus the high space demanding reaction of *i*-olefins to aldehydes and the aldol condensation of aldehydes proceeds easier.

With Rh@UiO-66 and Rh@UiO-67, more olefins are not reacted in the solution when increasing the length of the substrate from 6 carbon to 10. However, reaction with Rh@UiO-67 has higher conversion than Rh@UiO-66, proving the importance of pore size in the catalytic reaction. With Rh@MOF-808 and Rh@NU-1000, although the pore sizes are large enough for the diffusion of the molecules, the accessibility is limited and the space is blocked by the linker. The catalytic behavior is similar in the hydroformylation with bulky olefins over the Rh-supported catalysts. For the large sized bulky olefins, the large pore Rh-supported Zr-MOFs always have higher yield of corresponding aldehyde.

Overall, five different Rh-supported Zr-MOF catalysts have shown a total different behavior in the hydroformylation of different olefins. For large sized substrates, the pore size is a more important factor, which determines the entrance of the molecule. If the pore size is large enough relative to the substrate, accessibility the active sites become more important.

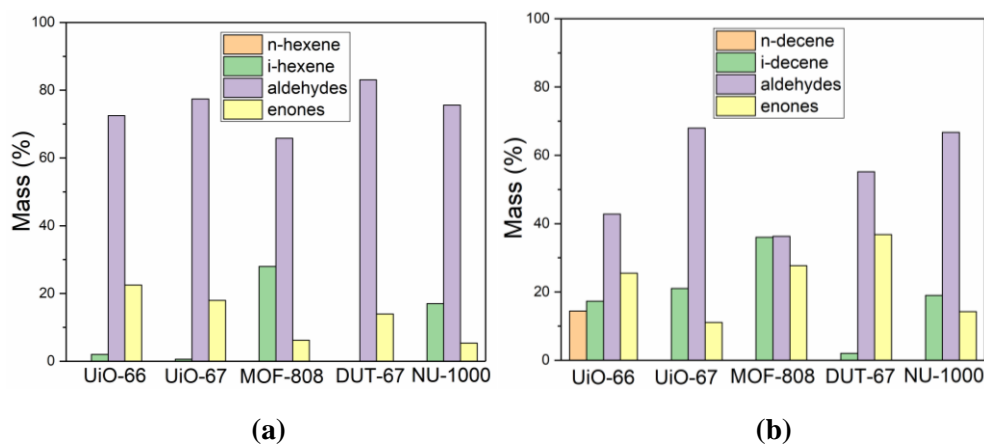


Figure 55. The composition in the reaction mixture over *n*-hexene and *n*-decene after 21h.

Table 6. The amount of *i*-alkenes in in the reaction mixture over *n*-hexene and *n*-decene after 21h.

<i>i</i> -alkenes	UiO-66	UiO-67	MOF-808	DUT-67	NU-1000
<i>i</i> -hexenes	2%	0.6%	28%	0%	17%
<i>i</i> -decenes	17.3%	21%	36%	2%	19%

4. Conclusion

Different Zr-MOFs with an increasing pore sized order: Rh@UiO-66 < Rh@UiO-67 < Rh@DUT-67 < Rh@MOF-808 < Rh@NU-1000 are prepared to study the relationship between the structure and catalytic properties in the hydroformylation of different sized alkenes and bulky olefins.

As synthesized MOFs and corresponding Rh-supported catalysts are characterized by PXRD, FTIR, SEM/TEM, XPS, TGA and nitrogen adsorption/desorption. The results show that all the samples are of high crystallinity, purity and stability.

Rh@UiO-66, Rh@UiO-67 and Rh@MOF-808 contain a hierarchical pore system of interconnected inter-particles featuring macro and mesopores as well as intra (nano) particle medium and large sized micropores. Rh@DUT-67 crystallized as regular cube-like shaped crystals which composed of aggregated small sized nanoparticle. The high porosity and pore volume facilitate the mass transfer.

Even with detailed inspection by high-resolution TEM it was impossible to detect any Rh particles due to the low loading (1Rh per *ca.* 50 unit cells). Obviously after loading, Rh species are highly dispersed in a single site manner. Rh is located at different positions, as indicate the XPS shifts of the framework atoms carbon oxygen sulfur, and zirconium. In the framework of DUT-67, the active sites are nearby the sulfur atom on the organic linker. In the other catalysts, Rh is supported in the secondary building units close to the Zr nodes.

All the Rh-supported catalysts shown high activity in the hydroformylation of olefins even in quite low Rh amount. TONs of 27000–65000 are achieved in the hydroformylation with *n*-alkenes. Even large molecules like *n*-hexadecene are converted due to the large pore sizes. Besides, the orientation of the phenylene linker have an important impact on the catalytic properties, total conversion equals in the hydroformylation over mixed *n*-alkenes (*n*-hexene, *n*-decene and *n*-hexadecene) with Rh@UiO-66 and Rh@UiO-67. Thus a single file diffusion phenomenon is observed.

As regioselectivity to linear aldehyde, i.e the *n/i*-aldehyde ratio, up to *ca.* 3 is achieved in the reaction of *n*-alkenes over all the catalysts. After a long time

reaction, this ratio is decreased due to the conversion of formed internal alkenes, therefore the yield of aldehydes increase continuously.

The hydroformylation with bulky olefins has lower yield than that with *n*-alkenes. The selectivity of the reaction is close to 100% due to no possibility of double bond isomerization. Even though the molecular size of cyclohexene is smaller than cyclooctene, cyclohexene is less active because it is stabilized in a half-chair conformation, which requires higher addition energy for the reaction.

In the framework of Rh@DUT-67, a large void space around the organic linker can be used for the catalytic reaction. Thus fastest conversion of olefins is observed of all the catalysts. Moreover, the large space also facilitate the aldol condensation Aldol condensation requires a linear head to head orientation of the reacting molecules.

With Rh@UiO-66 and Rh@UiO-67, more olefins are not reacted in the solution when increasing the length of the substrate form 6 carbon to 10. However, reaction with Rh@UiO-67 has higher conversion than Rh@UiO-66, proving the importance of pore size in the catalytic reaction. With Rh@MOF-808 and Rh@NU-1000, although the pore sizes are large enough for the diffusion of the molecules, the accessibility is limited. The entrance of MOF-808 is blocked by planar tripodal linker. With NU-1000, the large linker molecules restrict formation of active complex (olefin insertion).

Leaching test with Rh@UiO-66 was done to detect the Rh active species released into the solution during the reaction. The catalyst is stable against leaching. The filtered solution was not active. The supported MOF catalyst can be re-used. The re-usability of the Rh@DUT-67 was examined using *n*-hexene as model substance and the total conversion remain 80% after 5 times recycle.

Both the pore size and the accessibility contribute to the catalytic performance. For large sized substrates, the pore size is a more important factor, which determines the entrance of the molecule. The pore size of Zr-MOFs is large enough to allow conversion of large molecule like the *n*-hexadecene.

Over all, the catalytic results indicate that porous Zr-MOFs are interesting and potential materials for the preparation of metal supported heterogeneous catalysts.

The hybrid framework with its strictly alternating arrangement of inorganic and organic groups, allows the preparation of highly active isolated single site catalysts. Additionally, high density of separated sites can be achieved. The mass transfer is improved by the large voids and the hydrophilic-hydrophobic nature of the pore walls. Large molecules and sterically demanding molecules like internal alkenes can be converted. Moreover, Zr-MOF catalyst are stable and can be re-used.

Reference

- (1) Adkins, H.; Krsek, G. *Journal of the American Chemical Society* **1949**, *71*, 3051.
- (2) Franke, R.; Selent, D.; Börner, A. *Chemical Reviews* **2012**, *112*, 5675.
- (3) Beller, M.; Cornils, B.; Frohning, C. D.; Kohlpaintner, C. W. *Journal of Molecular Catalysis A: Chemical* **1995**, *104*, 17.
- (4) Ungváry, F. *Coordination Chemistry Reviews* **2007**, *251*, 2087.
- (5) Sharma, S. K.; Jasra, R. V. *Catalysis Today* **2015**, *247*, 70.
- (6) Chughtai, A. H.; Ahmad, N.; Younus, H. A.; Laypkov, A.; Verpoort, F. *Chemical Society Reviews* **2015**, *44*, 6804.
- (7) Abdel-Mageed, A. M.; Rungtaweivoranit, B.; Parlinska-Wojtan, M.; Pei, X.; Yaghi, O. M.; Behm, R. J. *Journal of the American Chemical Society* **2019**.
- (8) Wang, X.; Chen, W.; Zhang, L.; Yao, T.; Liu, W.; Lin, Y.; Ju, H.; Dong, J.; Zheng, L.; Yan, W.; Zheng, X.; Li, Z.; Wang, X.; Yang, J.; He, D.; Wang, Y.; Deng, Z.; Wu, Y.; Li, Y. *Journal of the American Chemical Society* **2017**, *139*, 9419.
- (9) Zhu, L.; Liu, X.-Q.; Jiang, H.-L.; Sun, L.-B. *Chemical Reviews* **2017**, *117*, 8129.
- (10) Senthil Kumar, R.; Senthil Kumar, S.; Anbu Kulandainathan, M. *Microporous and Mesoporous Materials* **2013**, *168*, 57.
- (11) Opelt, S.; Krug, V.; Sonntag, J.; Hunger, M.; Klemm, E. *Microporous and Mesoporous Materials* **2012**, *147*, 327.
- (12) Fang, X.; Shang, Q.; Wang, Y.; Jiao, L.; Yao, T.; Li, Y.; Zhang, Q.; Luo, Y.; Jiang, H. L. *Advanced Materials* **2018**, *30*.
- (13) Van Vu, T.; Kosslick, H.; Schulz, A.; Harloff, J.; Paetzold, E.; Schneider, M.; Radnik, J.; Steinfeldt, N.; Fulda, G.; Kragl, U. *Applied Catalysis A: General* **2013**, *468*, 410.
- (14) Van Vu, T.; Kosslick, H.; Schulz, A.; Harloff, J.; Paetzold, E.; Radnik, J.; Kragl, U.; Fulda, G.; Janiak, C.; Tuyen, N. D. *Microporous and Mesoporous Materials* **2013**, *177*, 135.
- (15) Hou, C.; Zhao, G.; Ji, Y.; Niu, Z.; Wang, D.; Li, Y. *Nano Research* **2014**, *7*, 1364.
- (16) Ahn, S.; Thornburg, N. E.; Li, Z.; Wang, T. C.; Gallington, L. C.; Chapman, K. W.; Notestein, J. M.; Hupp, J. T.; Farha, O. K. *Inorganic Chemistry* **2016**, *55*, 11954.
- (17) Rasero-Almansa, A. M.; Corma, A.; Iglesias, M.; Sánchez, F. *ChemCatChem* **2013**, *5*, 3092.
- (18) Smith, D. F.; Hawk, C. O.; Golden, P. L. *Journal of the American Chemical Society* **1930**, *52*, 3221.
- (19) Roelen, O.; CHEMISCHE VERWERTUNGSGESELLSCHAFT OBERHAUSEN MBH: German, 1938.
- (20) Falbe, J. *New syntheses with carbon Monoxide* Springer-Verlag Berlin Heidelberg, New York., 1980; Vol. 274.

- (21) Chikkali, S. H.; van der Vlugt, J. I.; Reek, J. N. H. *Coordination Chemistry Reviews* **2014**, *262*, 1.
- (22) Trzeciak, A. M.; Ziólkowski, J. J. *Coordination Chemistry Reviews* **1999**, *190-192*, 883.
- (23) Pruchnik, F. P. *Organometallic Chemistry of the Transition Elements* Plenum Press: New York, 1990.
- (24) Damoense, L.; Datt, M.; Green, M.; Steenkamp, C. *Coordination Chemistry Reviews* **2004**, *248*, 2393.
- (25) Lazzaroni, R.; Settambolo, R.; Caiazzo, A. In *Rhodium Catalyzed Hydroformylation*; Van Leeuwen, P. W. N. M., Claver, C., Eds.; Springer Netherlands: Dordrecht, 2002, p 15.
- (26) van Rooy, A.; Orij, E. N.; Kamer, P. C. J.; van Leeuwen, P. W. N. M. *Organometallics* **1995**, *14*, 34.
- (27) Mobin, R.; Rangrez, T. A.; Chisti, H. T. N.; Inamuddin; Rezakazemi, M. In *Functional Polymers*; Jafar Mazumder, M. A., Sheardown, H., Al-Ahmed, A., Eds.; Springer International Publishing: Cham, 2019, p 1135.
- (28) Cerveau, G.; Corriu, R. J. P.; Framery, E. *Chemistry of Materials* **2001**, *13*, 3373.
- (29) Unterlass, M. M. *European Journal of Inorganic Chemistry* **2016**, *2016*, 1135.
- (30) Schubert, U. *Chemical Society Reviews* **2011**, *40*, 575.
- (31) Dusselier, M.; Davis, M. E. *Chemical Reviews* **2018**, *118*, 5265.
- (32) Das, S.; Heasman, P.; Ben, T.; Qiu, S. *Chemical Reviews* **2017**, *117*, 1515.
- (33) De Vos, D. E.; Dams, M.; Sels, B. F.; Jacobs, P. A. *Chemical Reviews* **2002**, *102*, 3615.
- (34) Kresge, C. T.; Roth, W. J. *Chemical Society Reviews* **2013**, *42*, 3663.
- (35) Klinowski, J. *Chemical Reviews* **1991**, *91*, 1459.
- (36) Meng, X.; Xiao, F.-S. *Chemical Reviews* **2014**, *114*, 1521.
- (37) Weckhuysen, B. M.; Yu, J. *Chemical Society Reviews* **2015**, *44*, 7022.
- (38) Li, Y.; Li, L.; Yu, J. *Chem* **2017**, *3*, 928.
- (39) Li, G.; Pidko, E. A. *ChemCatChem* **2019**, *11*, 134.
- (40) Zhang, J.; Chen, J.; Peng, S.; Peng, S.; Zhang, Z.; Tong, Y.; Miller, P. W.; Yan, X.-P. *Chemical Society Reviews* **2019**, *48*, 2566.
- (41) Sun, M.-H.; Huang, S.-Z.; Chen, L.-H.; Li, Y.; Yang, X.-Y.; Yuan, Z.-Y.; Su, B.-L. *Chemical Society Reviews* **2016**, *45*, 3479.
- (42) Zhang, J.-P.; Liao, P.-Q.; Zhou, H.-L.; Lin, R.-B.; Chen, X.-M. *Chemical Society Reviews* **2014**, *43*, 5789.
- (43) Baumann, A. E.; Burns, D. A.; Liu, B.; Thoi, V. S. *Communications Chemistry* **2019**, *2*, 86.

- (44) Eddaoudi, M.; Sava, D. F.; Eubank, J. F.; Adil, K.; Guillerm, V. *Chemical Society Reviews* **2015**, *44*, 228.
- (45) Wang, C.; Zhang, T.; Lin, W. *Chemical Reviews* **2012**, *112*, 1084.
- (46) Rowsell, J. L. C.; Yaghi, O. M. *Microporous and Mesoporous Materials* **2004**, *73*, 3.
- (47) Furukawa, H.; Cordova, K. E.; O’Keeffe, M.; Yaghi, O. M. *Science* **2013**, *341*, 1230444.
- (48) Wang, P.-L.; Xie, L.-H.; Joseph, E. A.; Li, J.-R.; Su, X.-O.; Zhou, H.-C. *Chemical Reviews* **2019**, *119*, 10638.
- (49) Zhou, H.-C. J.; Kitagawa, S. *Chemical Society Reviews* **2014**, *43*, 5415.
- (50) Guillerm, V.; Kim, D.; Eubank, J. F.; Luebke, R.; Liu, X.; Adil, K.; Lah, M. S.; Eddaoudi, M. *Chemical Society Reviews* **2014**, *43*, 6141.
- (51) Schneemann, A.; Bon, V.; Schwedler, I.; Senkovska, I.; Kaskel, S.; Fischer, R. A. *Chemical Society Reviews* **2014**, *43*, 6062.
- (52) Furukawa, S.; Reboul, J.; Diring, S.; Sumida, K.; Kitagawa, S. *Chemical Society Reviews* **2014**, *43*, 5700.
- (53) Buser, H. J.; Schwarzenbach, D.; Petter, W.; Ludi, A. *Inorganic Chemistry* **1977**, *16*, 2704.
- (54) Hofmann, K. A.; Köpfer, F. *Zeitschrift für anorganische Chemie* **1897**, *15*, 204.
- (55) Rayner, J. H.; Powell, H. M. *Journal of the Chemical Society (Resumed)* **1952**, 319.
- (56) Hoskins, B. F.; Robson, R. *Journal of the American Chemical Society* **1990**, *112*, 1546.
- (57) Chae, H. K.; Eddaoudi, M.; Kim, J.; Hauck, S. I.; Hartwig, J. F.; O’Keeffe, M.; Yaghi, O. M. *Journal of the American Chemical Society* **2001**, *123*, 11482.
- (58) Li, H.; Eddaoudi, M.; Groy, T. L.; Yaghi, O. M. *Journal of the American Chemical Society* **1998**, *120*, 8571.
- (59) Rowsell, J. L. C.; Millward, A. R.; Park, K. S.; Yaghi, O. M. *Journal of the American Chemical Society* **2004**, *126*, 5666.
- (60) Chae, H. K.; Siberio-Pérez, D. Y.; Kim, J.; Go, Y.; Eddaoudi, M.; Matzger, A. J.; O’Keeffe, M.; Yaghi, O. M.; Materials, D.; Discovery, G. *Nature* **2004**, *427*, 523.
- (61) Eddaoudi, M.; Kim, J.; Rosi, N.; Vodak, D.; Wachter, J.; Keffe, M.; Yaghi, O. M. *Science* **2002**, *295*, 469.
- (62) Furukawa, H.; Ko, N.; Go, Y. B.; Aratani, N.; Choi, S. B.; Choi, E.; Yazaydin, A. Ö.; Snurr, R. Q.; O’Keeffe, M.; Kim, J.; Yaghi, O. M. *Science* **2010**, *329*, 424.
- (63) Mahmoudi, G.; Morsali, A.; Zhu, L.-G. *Polyhedron* **2007**, *26*, 2885.
- (64) Dan-Hardi, M.; Serre, C.; Frot, T.; Rozes, L.; Maurin, G.; Sanchez, C.; Férey, G. *Journal of the American Chemical Society* **2009**, *131*, 10857.

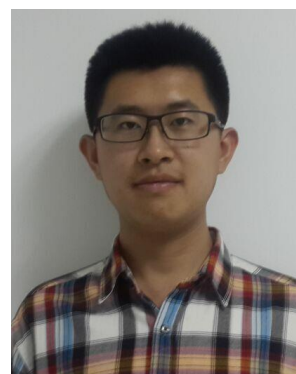
- (65) Fu, Y.; Sun, D.; Chen, Y.; Huang, R.; Ding, Z.; Fu, X.; Li, Z. *Angewandte Chemie International Edition* **2012**, *51*, 3364.
- (66) Dickie, D. A.; Schatte, G.; Jennings, M. C.; Jenkins, H. A.; Khoo, S. Y. L.; Clyburne, J. A. C. *Inorganic Chemistry* **2006**, *45*, 1646.
- (67) Chung, H.; Barron, P. M.; Novotny, R. W.; Son, H.-T.; Hu, C.; Choe, W. *Crystal Growth & Design* **2009**, *9*, 3327.
- (68) Liu, W.-T.; Ou, Y.-C.; Xie, Y.-L.; Lin, Z.; Tong, M.-L. *European Journal of Inorganic Chemistry* **2009**, *2009*, 4213.
- (69) Zhao, J. a.; Mi, L.; Hu, J.; Hou, H.; Fan, Y. *Journal of the American Chemical Society* **2008**, *130*, 15222.
- (70) Evans, J. D.; Sumbly, C. J.; Doonan, C. J. *Chemical Society Reviews* **2014**, *43*, 5933.
- (71) Deria, P.; Mondloch, J. E.; Karagiari, O.; Bury, W.; Hupp, J. T.; Farha, O. K. *Chemical Society Reviews* **2014**, *43*, 5896.
- (72) Lin, Z.-J.; Lü, J.; Hong, M.; Cao, R. *Chemical Society Reviews* **2014**, *43*, 5867.
- (73) Lu, W.; Wei, Z.; Gu, Z.-Y.; Liu, T.-F.; Park, J.; Park, J.; Tian, J.; Zhang, M.; Zhang, Q.; Gentle, T.; Bosch, M.; Zhou, H.-C. *Chemical Society Reviews* **2014**, *43*, 5561.
- (74) Zhang, Z.; Zaworotko, M. J. *Chemical Society Reviews* **2014**, *43*, 5444.
- (75) Bradshaw, D.; El-Hankari, S.; Lupica-Spagnolo, L. *Chemical Society Reviews* **2014**, *43*, 5431.
- (76) Van Vleet, M. J.; Weng, T.; Li, X.; Schmidt, J. R. *Chemical Reviews* **2018**, *118*, 3681.
- (77) Cohen, S. M. *Chemical Reviews* **2012**, *112*, 970.
- (78) Stock, N.; Biswas, S. *Chemical Reviews* **2012**, *112*, 933.
- (79) Gebert, W. *Acta Crystallographica Section B* **1978**, *34*, 2958.
- (80) Ockwig, N. W.; Delgado-Friedrichs, O.; O'Keeffe, M.; Yaghi, O. M. *Accounts of Chemical Research* **2005**, *38*, 176.
- (81) Li, H. E., M.; O'Keeffe, M.; Yaghi, O. M. *Nature* **1999**, *402*, 276.
- (82) Chui, S. S. Y.; Lo, S. M. F.; Charmant, J. P. H.; Orpen, A. G.; Williams, I. D. *Science* **1999**, *283*, 1148.
- (83) Feng, D.; Gu, Z.-Y.; Li, J.-R.; Jiang, H.-L.; Wei, Z.; Zhou, H.-C. *Angewandte Chemie International Edition* **2012**, *51*, 10307.
- (84) Thorarinsdottir, A. E.; Harris, T. D. *Chemical Reviews* **2020**.
- (85) Wang, Y.; Cui, H.; Wei, Z.-W.; Wang, H.-P.; Zhang, L.; Su, C.-Y. *Chemical Science* **2017**, *8*, 775.
- (86) Zhu, Q.-L.; Xu, Q. *Chemical Society Reviews* **2014**, *43*, 5468.
- (87) Zhang, T.; Lin, W. *Chemical Society Reviews* **2014**, *43*, 5982.
- (88) Wu, C.-D.; Zhao, M. *Advanced Materials* **2017**, *29*, 1605446.

- (89) Stavila, V.; Talin, A. A.; Allendorf, M. D. *Chemical Society Reviews* **2014**, *43*, 5994.
- (90) Ramaswamy, P.; Wong, N. E.; Shimizu, G. K. H. *Chemical Society Reviews* **2014**, *43*, 5913.
- (91) Kreno, L. E.; Leong, K.; Farha, O. K.; Allendorf, M.; Van Duyne, R. P.; Hupp, J. T. *Chemical Reviews* **2012**, *112*, 1105.
- (92) He, Y.; Zhou, W.; Qian, G.; Chen, B. *Chemical Society Reviews* **2014**, *43*, 5657.
- (93) Falcaro, P.; Ricco, R.; Doherty, C. M.; Liang, K.; Hill, A. J.; Styles, M. J. *Chemical Society Reviews* **2014**, *43*, 5513.
- (94) Canivet, J.; Fateeva, A.; Guo, Y.; Coasne, B.; Farrusseng, D. *Chemical Society Reviews* **2014**, *43*, 5594.
- (95) Sumida, K.; Rogow, D. L.; Mason, J. A.; McDonald, T. M.; Bloch, E. D.; Herm, Z. R.; Bae, T.-H.; Long, J. R. *Chemical Reviews* **2012**, *112*, 724.
- (96) Cui, Y.; Yue, Y.; Qian, G.; Chen, B. *Chemical Reviews* **2012**, *112*, 1126.
- (97) Witherspoon, V. J.; Xu, J.; Reimer, J. A. *Chemical Reviews* **2018**, *118*, 10033.
- (98) Li, J.-R.; Sculley, J.; Zhou, H.-C. *Chemical Reviews* **2012**, *112*, 869.
- (99) Suh, M. P.; Park, H. J.; Prasad, T. K.; Lim, D.-W. *Chemical Reviews* **2012**, *112*, 782.
- (100) de Lange, M. F.; Verouden, K. J. F. M.; Vlugt, T. J. H.; Gascon, J.; Kapteijn, F. *Chemical Reviews* **2015**, *115*, 12205.
- (101) Wang, Q.; Astruc, D. *Chemical Reviews* **2020**, *120*, 1438.
- (102) Fujita, M.; Kwon, Y. J.; Washizu, S.; Ogura, K. *Journal of the American Chemical Society* **1994**, *116*, 1151.
- (103) Schlichte, K.; Kratzke, T.; Kaskel, S. *Microporous and Mesoporous Materials* **2004**, *73*, 81.
- (104) de Oliveira, A.; Mavrandonakis, A.; de Lima, G. F.; De Abreu, H. A. *ChemistrySelect* **2017**, *2*, 7813.
- (105) Férey, G.; Mellot-Draznieks, C.; Serre, C.; Millange, F.; Dutour, J.; Surblé S.; Margiolaki, I. *Science* **2005**, *309*, 2040.
- (106) Horcajada, P.; Surblé S.; Serre, C.; Hong, D.-Y.; Seo, Y.-K.; Chang, J.-S.; Grenèche, J.-M.; Margiolaki, I.; Férey, G. *Chemical Communications* **2007**, 2820.
- (107) Farha, O. K.; Shultz, A. M.; Sarjeant, A. A.; Nguyen, S. T.; Hupp, J. T. *Journal of the American Chemical Society* **2011**, *133*, 5652.
- (108) Genna, D. T.; Pfund, L. Y.; Samblanet, D. C.; Wong-Foy, A. G.; Matzger, A. J.; Sanford, M. S. *ACS Catalysis* **2016**, *6*, 3569.
- (109) Feng, D.; Chung, W.-C.; Wei, Z.; Gu, Z.-Y.; Jiang, H.-L.; Chen, Y.-P.; Darensbourg, D. J.; Zhou, H.-C. *Journal of the American Chemical Society* **2013**, *135*, 17105.

- (110) Schröder, F.; Esken, D.; Cokoja, M.; van den Berg, M. W. E.; Lebedev, O. I.; Van Tendeloo, G.; Walaszek, B.; Buntkowsky, G.; Limbach, H.-H.; Chaudret, B.; Fischer, R. A. *Journal of the American Chemical Society* **2008**, *130*, 6119.
- (111) Jiang, H.-L.; Liu, B.; Akita, T.; Haruta, M.; Sakurai, H.; Xu, Q. *Journal of the American Chemical Society* **2009**, *131*, 11302.
- (112) Yuan, B.; Pan, Y.; Li, Y.; Yin, B.; Jiang, H. *Angewandte Chemie International Edition* **2010**, *49*, 4054.
- (113) Liu, X.-H.; Ma, J.-G.; Niu, Z.; Yang, G.-M.; Cheng, P. *Angewandte Chemie International Edition* **2015**, *54*, 988.
- (114) Zhou, W.; He, D. *Green Chemistry* **2009**, *11*, 1146.
- (115) Zeelie, T. A.; Root, A.; Krause, A. O. I. *Applied Catalysis A: General* **2005**, *285*, 96.
- (116) Sun, Z.; Wang, Y.; Niu, M.; Yi, H.; Jiang, J.; Jin, Z. *Catalysis Communications* **2012**, *27*, 78.
- (117) Riisager, A.; Wasserscheid, P.; van Hal, R.; Fehrmann, R. *Journal of Catalysis* **2003**, *219*, 452.
- (118) Selent, D.; Franke, R.; Kubis, C.; Spannenberg, A.; Baumann, W.; Kreidler, B.; Börner, A. *Organometallics* **2011**, *30*, 4509.
- (119) Behr, A.; Levikov, D.; Vogelsang, D. *Journal of Molecular Catalysis A: Chemical* **2015**, *406*, 114.
- (120) Chen, C.; Qiao, Y.; Geng, H.; Zhang, X. *Organic Letters* **2013**, *15*, 1048.
- (121) Liu, Y.-l.; Zhao, J.-g.; Zhao, Y.-j.; Liu, H.-M.; Fu, H.-y.; Zheng, X.-l.; Yuan, M.-l.; Li, R.-x.; Chen, H. *RSC Advances* **2019**, *9*, 7382.
- (122) Yu, S.; Chie, Y.-m.; Guan, Z.-h.; Zhang, X. *Organic Letters* **2008**, *10*, 3469.
- (123) Gadzikwa, T.; Bellini, R.; Dekker, H. L.; Reek, J. N. H. *Journal of the American Chemical Society* **2012**, *134*, 2860.
- (124) Güven, S.; Hamers, B.; Franke, R.; Priske, M.; Becker, M.; Vogt, D. *Catalysis Science & Technology* **2014**, *4*, 524.
- (125) Fujita, S.-I.; Akihara, S.; Fujisawa, S.; Arai, M. *Journal of Molecular Catalysis A: Chemical* **2007**, *268*, 244.
- (126) Lang, R.; Li, T.; Matsumura, D.; Miao, S.; Ren, Y.; Cui, Y.-T.; Tan, Y.; Qiao, B.; Li, L.; Wang, A.; Wang, X.; Zhang, T. *Angewandte Chemie International Edition* **2016**, *55*, 16054.
- (127) Gorbunov, D.; Safronova, D.; Kardasheva, Y.; Maximov, A.; Rosenberg, E.; Karakhanov, E. *ACS Applied Materials & Interfaces* **2018**, *10*, 26566.
- (128) Chuai, H.; Su, P.; Liu, H.; Zhu, B.; Zhang, S.; Huang, W. *Catalysts* **2019**, *9*.
- (129) Wang, Y.; Yan, L.; Li, C.; Jiang, M.; Zhao, Z.; Hou, G.; Ding, Y. *Journal of Catalysis* **2018**, *368*, 197.

- (130) Jia, X.; Liang, Z.; Chen, J.; Lv, J.; Zhang, K.; Gao, M.; Zong, L.; Xie, C. *Organic Letters* **2019**, *21*, 2147.
- (131) Liang, Z.; Chen, J.; Chen, X.; Zhang, K.; Lv, J.; Zhao, H.; Zhang, G.; Xie, C.; Zong, L.; Jia, X. *Chemical Communications* **2019**, *55*, 13721.
- (132) Shi, Y.; Ji, G.; Hu, Q.; Lu, Y.; Hu, X.; Zhu, B.; Huang, W. *New Journal of Chemistry* **2020**, *44*, 20.
- (133) Tao, L.; Zhong, M.; Chen, J.; Jayakumar, S.; Liu, L.; Li, H.; Yang, Q. *Green Chemistry* **2018**, *20*, 188.
- (134) Tan, M.; Yang, G.; Wang, T.; Vitidsant, T.; Li, J.; Wei, Q.; Ai, P.; Wu, M.; Zheng, J.; Tsubaki, N. *Catalysis Science & Technology* **2016**, *6*, 1162.
- (135) Cavka, J. H.; Jakobsen, S.; Olsbye, U.; Guillou, N.; Lamberti, C.; Bordiga, S.; Lillerud, K. P. *Journal of the American Chemical Society* **2008**, *130*, 13850.
- (136) Furukawa, H.; Gándara, F.; Zhang, Y.-B.; Jiang, J.; Queen, W. L.; Hudson, M. R.; Yaghi, O. M. *Journal of the American Chemical Society* **2014**, *136*, 4369.
- (137) Bon, V.; Senkovska, I.; Baburin, I. A.; Kaskel, S. *Crystal Growth & Design* **2013**, *13*, 1231.
- (138) Mondloch, J. E.; Bury, W.; Fairen-Jimenez, D.; Kwon, S.; DeMarco, E. J.; Weston, M. H.; Sarjeant, A. A.; Nguyen, S. T.; Stair, P. C.; Snurr, R. Q.; Farha, O. K.; Hupp, J. T. *Journal of the American Chemical Society* **2013**, *135*, 10294.
- (139) Jiang, J.; Gándara, F.; Zhang, Y.-B.; Na, K.; Yaghi, O. M.; Klemperer, W. G. *Journal of the American Chemical Society* **2014**, *136*, 12844.
- (140) Wang, T. C.; Vermeulen, N. A.; Kim, I. S.; Martinson, A. B. F.; Stoddart, J. F.; Hupp, J. T.; Farha, O. K. *Nature Protocols* **2016**, *11*, 149.
- (141) Katz, M. J.; Brown, Z. J.; Colón, Y. J.; Siu, P. W.; Scheidt, K. A.; Snurr, R. Q.; Hupp, J. T.; Farha, O. K. *Chemical Communications* **2013**, *49*, 9449.
- (142) Patterson, A. L. *Physical Review* **1939**, *56*, 978.
- (143) Sing, K. S. W. *Pure and Applied Chemistry* **1985**, *57*, 603.
- (144) Brunauer, S.; Emmett, P. H.; Teller, E. *Journal of the American Chemical Society* **1938**, *60*, 309.
- (145) Scherrer, P. In *Kolloidchemie Ein Lehrbuch*; Zsigmondy, R., Ed.; Springer Berlin Heidelberg: Berlin, Heidelberg, 1912, p 387.
- (146) Jensen, F. R.; Bushweller, C. H. *Journal of the American Chemical Society* **1969**, *91*, 5774.

Yanjun Sun



Place and Date of Birth: Jilin, P.R. China, 25/09/1990
Nationality: Chinese
Address: Erich-Schlesinger-Str. 20,
Rostock, Germany
E-mail: yanjun.sun@uni-rostock.de
Language: English: IELTS 6.0 German: B1.1

EDUCATION

- 10/2016 –Present **Research Doctorate**
Institute of Chemistry/Leibniz Institute for Catalysis, University of Rostock
Topic: Rh-catalyzed hydroformylation with Zr metal-organic frameworks
Supervisor: Prof. Dr. Axel Schulz
- 08/2013-06/2016 **Master in Inorganic Chemistry**
State Key Laboratory of Inorganic Synthesis and Preparative Chemistry
Jilin University, Changchun, Jilin, P.R. China
Topic: Synthesis and properties of molecular sieves and Aluminum Phosphate
(absorption and conductivity), Molecular engineering
Supervisor: Prof. Dr. Jihong Yu, Prof. Dr. Jiyang Li
- 09/2009-06/2013 **Bachelor of Chemistry**
Jilin University, Changchun, Jilin, P.R. China
Core Course: Inorganic Chemistry, Organic Chemistry, Physical Chemistry,
Analysis Chemistry

Research Experience

- 09/2016-Present **Doctoral research experience**
- Hydroformylation of olefins over Rh-supported Zr-MOF UiO-66, UiO-67, and MOF-808
 - Hydroformylation of olefins over Rh-supported heteroatom substituted Zr-MOF DUT-67
 - Hydroformylation of olefins over Rh-supported extra large sized mesopore Zr-MOF NU-1000

08/2013-06/2016 **Master research experience**

- Research in synthesis and high proton conduction of a new open-framework aluminophosphate (JU103)
- Assisted in synthesis of a new aluminophosphate molecular sieve (JU93) with adsorption selectivity of CO₂ over CH₄
- Assisted in synthesis of two new four-connected zeolite-like magnesium aluminophosphates (JU94 and JU95)
- Synthesis of crystals and property research of iron phosphates with open-framework

Awards

- | | |
|----------------------------------|-------------|
| ➤ National Scholarship | 2015 |
| ➤ Evonik Scholarship | 2015 |
| ➤ Excellent Master Scholarship | 2014 |
| ➤ Excellent Bachelor Scholarship | 2013 |

Publications

- Influence of the pore structure on the catalytic performance of large pore Rh-supported Zr-MOFs in the hydroformylation of n-alkenes, in preparation
- Hydroformylation of olefins over rhodium supported on the metal–organic framework DUT-67, in preparation
- Hydroformylation of olefins over rhodium supported on the mesoporous metal–organic framework NU-1000, in preparation
- High proton conduction in a new alkali metaltemplated open-framework aluminophosphate., Y. Sun, Y. Yan., Y. Wang, Y. Li, J. Li and J. Yu, *Chem. Commun.*, 2015, **51**, 9317.
- Organotemplate-free hydrothermal synthesis of an aluminophosphate molecular sieve with AEN zeolite topology and properties of its derivatives., Y. Wang, Y. Sun, Y. Mu, C. Zhang, J. Li and J. Yu, *Chem. Commun.*, 2014, **50**, 15400.
- ChemInform Abstract: Two New Four-Connected Zeolite-Like Magnesium Aluminophosphates with Intersecting 8-Ring Channels., Y. Wang, Y. Mu, Y. Sun and J. Li, *RSC Adv.*, 2014, 4, 56288

Conference Participation

Poster “**Influence of the structure of Rh supported Zr-MOF Catalysts on the performance in the hydroformylation of olefins**”

YanJun Sun, Hendrik Kosslick and Axel Schulz.

“3rd International Conference on Metal Organic Frameworks and Porous Polymers”, Paris, 27-30 October, 2019